ANALYSIS OF ADDITIVELY MANUFACTURED INJECTORS FOR ROTATING DETONATION ENGINES

THESIS

Michael C. Waters, 2d Lt, USAF

AFIT-ENY-MS-18-M-301

DEPARTMENT OF THE AIR FORCE
AIR UNIVERSITY

AIR FORCE INSTITUTE OF TECHNOLOGY

Wright-Patterson Air Force Base, Ohio

AFIT-ENY-MS-18-M-301

ANALYSIS OF ADDITIVELY MANUFACTURED INJECTORS FOR

ROTATING DETONATION ENGINES

THESIS

Presented to the Faculty

Department of Aeronautical Engineering

Graduate School of Engineering and Management

Air Force Institute of Technology

Air University

Air Education and Training Command

in Partial Fulfillment of the Requirements for the

Degree of Master of Science in Aeronautical Engineering

Michael C. Waters, B.S.A.E.

2d Lt, USAF

March 8, 2018

ANALYSIS OF ADDITIVELY MANUFACTURED INJECTORS FOR

ROTATING DETONATION ENGINES

THESIS

Michael C. Waters, B.S.A.E.
2d Lt, USAF

Committee Membership:

Dr. Carl Hartsfield
Chair

Dr. William Hargus
Member

Maj David Liu, PhD
Member

Contents

List of Figures

List of Tables

AFIT-ENY-MS-18-M-301

Abstract

This research represents an experimental and computational analysis of additively manufactured injectors for Rotating Detonation Engines (RDEs) for use in rocket propulsion. This research was based on the manufacture and testing of existing injector element designs using additive techniques. The designs were modeled from geometries gathered from Sutton and Biblarz *Elements of Rocket Propulsion* and shown in Table (1) [23]. The designs chosen are representative of common orifice geometries. The goal of this research was to characterize the viscous losses of each design based on the discharge coefficient. The designs were computationally simulated to gain insight to the flow characteristics using multiple sets of conditions for surface roughness and inlet pressure. The results were then compared to experimental results of similar conditions. Each design was then tested using pressurized water as a simulated propellant. The results show the viscous losses to be highly dependent on design and the relative roughness of the surface. For designs with areas of high relative roughness and L/D such that flow interaction is facilitated, the surface roughness was shown to effect the discharge coefficient. It was found when L/D was small enough to be neglected, as was the case with Designs 1 and 2, the relative roughness of the surface had no precipitable effect on the flow.

Acknowledgements

I would like to thank my research advisor, Dr. Carl Hartsfield, for his continuous guidance and endless patience throughout this research. I would also like to thank my research committee for their advice and recommendations throughout this research process.

Finally I would like to thank my wife for her never ending support in all of my endeavors and for always reminding me of the truly important things in life especially during the most trying of times.

Nomenclature

$d_{orifice}$	Injector Orifice Diameter
C_d	Discharge Coefficient
A	Cross sectional area of injector opening
ρ	Density
ΔP	Pressure change across injector head
$\dot{m}_t$	Total Mass flow rate of engine
N	Number of injector elements
f	Roughness Height
g	Acceleration due to Gravity
l	Length
D_h	Hydraulic Diameter
v	Flow Velocity
μ	Dynamic Viscosity
ρ	Density
Re	Reynolds Number
$T_{intensity}$	Turbulence Intensity
P_{CJ}	Chapman-Jouguet detonation pressure
Γ	Ratio of specific heats
ρ_{TMD}	Thoretical Maximum Density

ANALYSIS OF ADDITIVELY MANUFACTURED INJECTORS FOR

ROTATING DETONATION ENGINES

I Introduction

1.1 Motivation

Detonation engines have been found to offer higher efficiencies than traditional deflagration engines. [21] These efficiencies are due to detonations following the Humphrey cycle instead of the Brayton cycle. The efficiency of the deflagration process for an ideal Brayton cycle is dependent on the temperature before and after isentropic expansion. The efficiency of pressure gain combustion, as with detonation, is calculated using the ideal Humphrey cycle. It not only depends on the temperature before and after isentropic expansion, but also combustion. So far these efficiencies have lead research into Rotating Detonation engines (RDEs) for application to air-breathing propulsion systems. There has been very little research into developing a RDE for rocket propulsion. With today's technology level, the RDE could not be used for launch applications; however, a first stage propulsion system is where the higher efficiencies would have the highest effect. Until advancements allowing the increased size to be feasible, the RDE may provide an alternative to the traditional liquid fuel rocket engines used for orbit maintenance. The higher efficiency of the engines leads to lower operational costs associated with performance. These lower costs may allow for further advancements in other areas of the spacecraft.

The advances in additive manufacturing technology have allowed the production of parts, both prototype and final, to be less costly to a program in terms of time and

monetary costs. Additive manufacturing processes are capable of producing parts in a multitude of materials from plastic polymers to metals. To produce a metallic part, a machine will typically use a high powered laser or electron beam to sinter or weld particles of fine powder together layer by layer. The machine is controlled by a computer thereby reducing the human involvement. Because the laser is sintering particles of a fine powder and not removing excess material, the waste involved in production is drastically reduced as discussed later in Chapter II. The reductions in cost and time required have allowed for the rapid prototyping of parts and a more iterative design process to evolve. This iterative design process allows a design team to build parts that are impossible to make through traditional subtractive methods and may satisfy the mission requirements more efficiently.

Additive manufacturing is still a novel concept in the production of combustion and load bearing parts. An additively manufactured product may not have the same thermal or structural properties as a similar subtractively manufactured part. For these reasons, there has been little research done to investigate the capabilities of AM for combustion components, specifically injectors. The injector of a rocket engine not only inserts fuel to the combustion chamber at the correct flow rate, position, and atomization level, but also has to do the same with the oxidizer while also making sure the two mix adequately for combustion. So far, research for rocket engine injectors has been focused on subtractive manufacturing methods, drastically limiting the design capabilities.

1.2 Problem Statement

While additive manufacturing reduces cost, time, and waste throughout the manufacturing process, there are drawbacks. One of the drawbacks is a higher surface roughness when compared to a traditionally manufactured part. Injectors with a hy-

draulic diameter on the same scale or even an order of magnitude higher than the size of the irregularities may have higher viscous losses.[10] These losses could reduce the efficiency of the injector reducing the performance of the engine as a whole. The goal of this research is to evaluate and quantify the effects of additive manufacturing (AM) on injector element performance for Rotating Detonation Engines (RDEs). This will be investigated through the use of computational as well as experimental methods.

1.3 Research Methodology

For this research, the injector elements were modeled using computational fluid dynamics (CFD) to determine preliminary results on flow behavior. After these results, several injector elements were manufactured from Inconel 718 using an additive method known as direct laser sintering (DLS). These injectors were modeled from those presented in Table (1) located in Chapter II Section 2.2.

The injector elements were manufactured using Inconel 718 because it is representative of the materials that would be used in a live fire injector. The pressure in the water tanks was controlled to yield a desired pressure drop across the injector face. The volumetric flow rate was measured, allowing calculation of the mass flow rate, discharge coefficient, and Reynolds' number. High speed imagery was used to visualize the jets and their respective flow characteristics. After all testing was concluded, several AM injector elements were sectioned to be examined using a laser scanning microscope to quantify the surface roughness and confirm assumptions made in this regard.

1.4 Research Objectives

This research is aimed at understanding the effects of surface roughness on flow characteristics and interactions of injection streams. The following research objectives

3

were identified to help further this understanding:

1. Measure mass flow rate of additively and subtractively manufactured injector elements with a controlled pressure drop.

2. Calculate discharge coefficient of injector designs using computational and experimental techniques

3. Compare discharge coefficient of both techniques to each other as well as historical data.

4. Visualize flow of AM injector elements.

1.5 Preview

This section provides a preview of the remaining chapters. Chapter II is the Literature Review and as such summarizes the relevant theory, discoveries, and research in this area. The processes and procedures of experimentation are laid out in Chapter III, Methodology. Chapter IV details the results of the computational and experimental investigations as well as an analysis of the data collected. Chapter V details the conclusions of this research and includes recommendations for future research efforts.

II Background

2.1 Introduction to Literature Review

This research is looking at the effects of additively manufacturing injectors for Rotating Detonation Engines (RDEs). This encompasses the integration of three base areas of interest: chemical rocket injectors, RDEs, and additive manufacturing. Each of these areas has been thoroughly investigated individually, but not much research has gone into all three areas together. The injector of a chemical rocket engine is one of the first critical failure points of a rocket engine. If the propellant is not reaching the combustion chamber, then the engine will not produce thrust or may have unsteady combustion, leading to catastrophic failure of the vehicle. A RDE is a combustion engine similar to a typical rocket engine; however, it is based on detonation combustion rather than deflagration combustion. Detonation combustion allows for a higher combustion efficiency than the traditional deflagration combustion cycle. The use of additive manufacturing techniques has revolutionized the design process by drastically reducing the time and cost to prototype parts. However, additive manufacturing is only starting to be used as a viable method to produce 'flight' or final mission parts. In 2012, NASA[14] successfully designed and built a full-sized rocket engine using additively manufactured parts.

2.2 Past Work in Chemical Rocket Engine Injectors

The injection plate of a chemical rocket engine is a key component to the assembly, without it the engine could not function. A comparison can be made between the injector for a rocket engine and a carburetor of an internal combustion engine in that each allows the proper mixture of fuel and oxidizer to enter the combustion chamber. However, the injectors on a rocket engine perform many more functions

than the carburetor does for the respective engines. The injection plate provides structural support by acting as a backstop or end cap to the combustion chamber. This end cap is what allows the pressure to increase and route the exhaust gases to a nozzle or other post-combustion subsystem. The injector plate also provides a thermal relief for the combustion chamber. The effects of fuel thermal changes were studied by Heidmann in the 1950s who found a general trend of increased efficiencies with increased temperature [12]. Heidmann also noted that should the temperature increase to the point of fuel vaporization before the injector, then large performance losses would be seen. Heidmann saw a 20% increase in efficiency with an increase of 6 inches (from 2 inches to 8 inches) of the combustion chamber length. This increased efficiency is not explicitly explained by Heidmann, however; it may be a result of the increased distance allowing further atomization and mixing of the propellants. This increased mixing would mean more of the propellants burn in the combustion chamber instead of the plume or exhaust outside of the engine. Heidmann did see increases in characteristic velocity for varying chamber lengths from 2 to 8 inches in 2 inch increments. These performance increases were not the focus of the research and are not explicitly explained.

The layout of the injection plate can allow for advanced cooling or mixing effects to take place within the combustion chamber, dependent on the needs of the engine. Rocket engine performance is measured through specific impulse and referred to as ISP. The performance of the injectors are highly influential on the total ISP of the rocket engine. A percentage point decrease of injection efficiency results in a decrease of the same magnitude in overall ISP [13]. The injector plate typically has a pressure drop of 15%-20% of the chamber pressure. This amount of drop allows for the dampening of combustion oscillation; therefore, lessening the harmonics produced in the combustion chamber that could be damaging to the rest of the rocket. For high

pressure engines, injector face erosion is an issue that can be mission ending. Face erosion can result in burn through of the injector manifold. This could cause issues ranging from pushing hot, high-pressure fuel or oxidizer back into the feed lines, causing catastrophic failure; or changing the mixture ratio of the fuel and oxidizer, causing off-mixture operations and decreased performance [25]. With low-pressure engines, this face erosion is mainly superficial and normally does not rise to the level of potential mission failure.

Injector Orifice and its Effects.

The injector orifice is the section of the injector where the propellant actually enters the combustion chamber. This section of the injector is arguably the most important in that it determines the mixing properties of the flow as well as the jet and droplet size. The mixing of the flow allows for the proper ratios to be reached and steady combustion or detonation to occur. The mixing is highly dependent on the injection jet size, speed, and direction. The size of the droplets in the jet directly affects combustion and the rates of mixing. The speed and direction of the jet help determine the momentum of the propellant, and affect the mixing rate. In order to achieve high combustion efficiency, there must be uniform mixing of propellant parts on a level as close to molecular as possible. Research by Priem and Heidmann of NASA Lewis Research Center in the 1950s concluded the droplet vaporization could be used as a combustion rate controlling mechanism.[25, 19]. This uniform mixing must also be in the correct mixture ratio to support the combustion event.

The orifice of an injector is characterized primarily by the pressure loss associated with its design, this value is known as the discharge coefficient. Equation (1) [23] shows the general form of the equation to calculate the discharge coefficient.
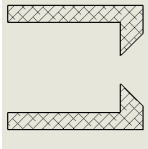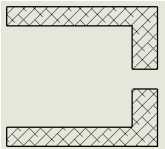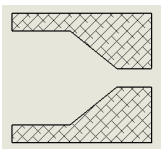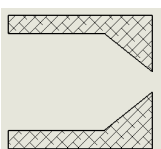
$$C_d = \frac{\dot{m}}{A\sqrt{2\rho\Delta p}} \tag{1}$$

Where A is the cross sectional area of the orifice, Δp is the pressure drop across the injector, $\dot{m}$ is the mass flow rate through the orifice, and ρ is the density of the propellant. Due to typical subtractive manufacturing, non-round openings are not prevalent due to the difficulty in manufacturing. However, with advances in additive manufacturing, non-traditional shapes may prove to be more advantageous designs and equivalent opening areas would be used to calculate a discharge coefficient. Equation (2) [13] shows a general form equation to calculate the diameter of the injector orifice needed for a given flow rate. Here N is the number of orifices used in the injector manifold.

$$d_{orifice} = \left(\frac{4\dot{m}}{\pi C_d\sqrt{2\rho\Delta p}}\right)^{0.5} \tag{2}$$

Table (1) shows a few general and common types of injector orifices as well as their typical diameters and discharge coefficients as found in *Rocket Propulsion Elements* [23]. Each orifice is designed similarly with only slight changes from one to another; however, each small change results in different flow characteristics for the injection jet and different pressure loss behaviors. These are the geometries to be used throughout this research given the access to their dimensions as well as discharge coefficients to compare to.

Table 1. Injector Orifices [23]

Orifice Type	Diameter (mm)	Discharge Coefficient	Diagram
Sharp-edged orifice	Above 2.5 Below 2.5	0.61 0.65 approx.	
Short-tube with rounded entrance	1.00 1.57	0.88 0.90	
Short-tube with conical entrance	0.50 1.00 1.57 2.54 3.18	0.7 0.82 0.76 0.84-0.80 0.84-0.78	
Sharp-edged cone	1.00 1.57	0.70-0.69 0.72	

Much research with injectors for chemical rocket engines exists and their development for particular circumstances. Three main types of injectors exist: coaxial, impinging, and non-impinging. Impinging injectors can be subdivided into two groups know as like and unlike. This refers to whether the injection streams are of the same propellant component or not, i.e. if two fuel or two oxidizer streams are interacting or if one fuel and one oxidizer stream are interacting.

A coaxial injector is comprised of two concentric flow jets. The inner jet is typically a liquid oxidizer where the outer jet is typically a gaseous fuel. This type of injector was first developed by NASA as a high performance injection element for

LOX/$H_2(g)$) propellant [13]. A typical velocity ratio of the two injection jets is 100 (LOX) / 1,000 ($H_2(g)$) [13]. The viscous interaction of the two shear layers is the primary mixing method of this type of injector. However, because this mixing relies on the shear interactions, it takes valuable axial or horizontal distance away from the injector face to achieve proper mixing. In 2009, the Air Force Research Laboratory and the University of California, Los Angeles collaborated on research with coaxial injectors. [20] This research found changes in the geometry of the coaxial radii to reduce acoustical perturbations at three pressure regimes: sub-critical, critical, and super-critical. [20]

Unlike-impinging injectors are designed in such a way so a fuel jet interacts or impinges on an oxidizer jet. This interaction is what initiates the mixing for the propellant. These injectors are designed based on the type of propellant being utilized. Each propellant mixture component will have a different momentum, given a particular pressure drop across the injector and, therefore, the injector orifice will have to be angled slightly differently to achieve the desired mixing characteristics as the jets interact. Like-impinging injectors follow the same concepts of the unlike-impinging; however, the jets interacting with each other are of the same propellant component(ie: fuel-fuel or oxidizer-oxidizer) [13]. Each of these types can be expanded into a nearly infinite number of designs and setups.

Non-impinging injectors are simply defined as injectors where the jets do not directly interact or impinge. There are endless ways to design these types of injectors and are only limited by the capabilities of manufacturing and imagination. A simple example of this type of injector is called a shower head injector. This injector acts just as a typical shower head where the streams exit the injector and are not designed to interact with each other [13].

2.3 Rotating Detonation Engines

Rotating Detonation Engines have gained much attention due to their increased efficiencies over conventional deflagration engines. These efficiencies are a result of RDEs using pressure-gain combustion [21]. This pressure-gain combustion follows the Humphrey cycle, where the normal deflagration cycle follows the Brayton cycle [21]. Figure(1) shows a comparison of the Brayton cycle and the Humphrey cycle. The differences in the areas under the respective cycle curves is where the higher efficiencies originate. These higher efficiencies have led to significant investment into research of RDEs for air-breathing propulsion. However, not much research has been conducted in the use of these engines for rocket propulsion.
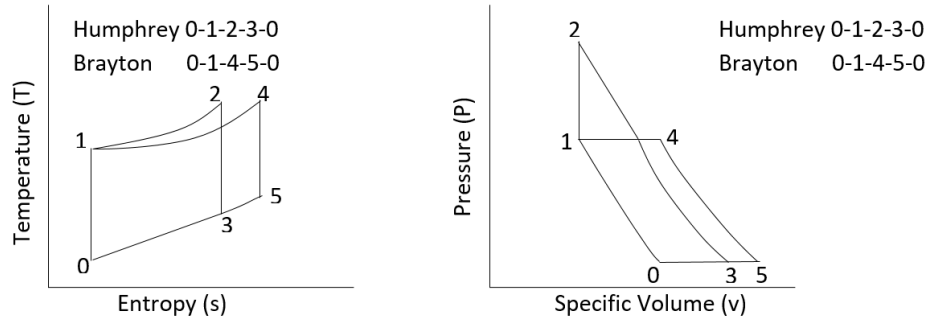
Figure 1. Comparison of Brayton and Humphrey Cycles [21]

All current chemical rocket engines today are a deflagration-based combustion cycle; therefore, limited by the Brayton cycle [3]. To achieve higher thermodynamic efficiency, a detonation based engine could be used. The rotating detonation engine (RDE) is an example of this type of engine. Figure (2) graphically shows the combustion process of an RDE. First, all the propellant fills the annulus as the fuel and oxidizer mix. Next, the ignition source ignites the mixture causing a deflagration to begin. This deflagration transitions to a detonation wave then travels around the

annulus. This detonation wave then continues to rotate around the annulus as long as a detonable mixture of propellant is ahead of the wave. The RDE hits steady operation when one or more detonation waves propagate around the annulus [6]. In 2015 Anand, George, Driscoll, and Gutmark found with a hydrogen/air rotating detonation combustor (RDC) the instabilities that exist in the RDC were reduced when multiple detonation waves were present in the combustor [4]. Anand et al. (2015) found the overall stability of the RDC increased with multiple waves; however, an optimization study was not performed nor were any visualization techniques used.

A detonation engine is no longer limited by the Brayton cycle but takes advantage of the Humphrey cycle. The Humphrey cycle allows for a higher efficiency; therefore, better performance. The RDE has many advantages over the current chemical engines other than the increased thermodynamic efficiencies. The RDE has no moving parts, and as with all liquid rocket engines, a RDE can be turned: on, off, and throttled as needed for thrusting.

Figure 2. RDE Detonation Process [21]

The basic combustion process a RDE follows is simple; Figure (3) shows a 3D simulation of the detonation wave traveling around the annulus. As shown in Figure

12

(3), the detonation wave is rather short in comparison to the overall axial length of the annulus. After the detonation wave, the products move along with the oblique shock trailing behind the detonation wave front toward the exhaust exit. The process is then repeated as the detonation revolves around the annulus. The flow rate of the propellant determines the presence of multiple waves. [22] As the flow rate increases, enough propellant becomes available to support the presence of multiple detonations. This is discussed further from a computational standpoint in Subsection (2.3) .
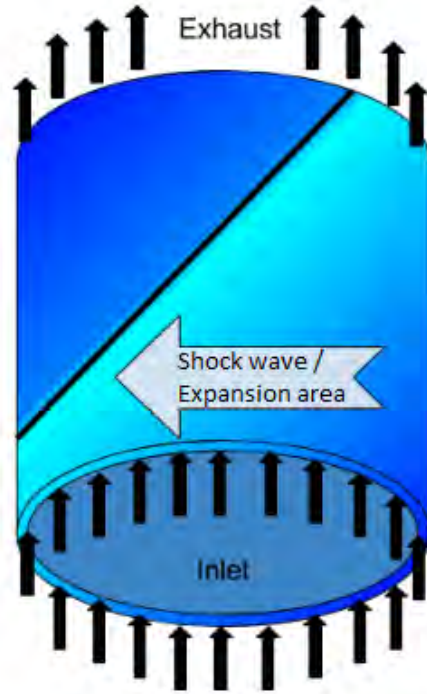
Figure 3. Compressible Fluid Characteristics in an RDE [21]

The propellant mixture is measured as a range of the equivalence ratio, or a ratio of the fuel to oxidizer. For full combustion, this ratio is ideally one; however, the mixture will not have to equal one in all locations evenly as long as the proper ratio exists in the detonation region such that the detonation wave can adequately propagate. Research through the Air Force Research Laboratory in 2012 [22] found a

range of air mixtures and their relation to thrust output of an their RDE. Table (2) shows the results of their experiment. For the last case of 24.8% Oxygen and 75.2% Nitrogen, an upper flow rate and thrust limit was not found and the values presented are the highest values testable.

Table 2. Values of air mixture percentages as they relate to Air flow rate and Thrust achieved [22]

% Oxygen	% Nitrogen	Air Flow Rate (lb/min)	Thrust/ Mass Flow Rate (lbf/lb/min)
21	78	40	1.25
23	77	50	1.30
24.8	75.2	130	1.54

Computational Analysis of RDEs.

For simulation purposes, research performed by the Naval Research Laboratory (NRL) found that a RDE may be treated as being 2D instead of 3D [21]. This is due to the radial distance of the annulus being much smaller than the azimuthal distance of the combustion annulus. In 2013, NRL, the Air Force Research Laboratory (AFRL), and the University of Connecticut conducted research into the computational modeling of mixing in RDEs and its impact on performance measured by ISP. Using amended ZND models for detonation, Nordeen was able to examine the effects of divergence and mixing within the annulus[16]. ZND is a 1D detonation model for explosives first developed during World War II [9]. The computation was carried out using an Euler method. The propellant mixing was modeled through the use of an arbitrary convective mixing term in a 2D simulation[16]. The convective mixing term allowed for simplicity of not modeling two injector element jets. By changing the mixing rates, Nordeen was able to effectively model a range of injector mixing

effectiveness. Computations were done with varying mixing rates and initial mixing fractions from a fully premixed propellant to a completely separate bi-propellant mixed post-injection[16]. Nordeen's research [16] showed little variation (approximately ± 1.5 sec) in ISP, this lead to only a 77 m/s difference between the highest and lowest wave speed [16].

In 2012, research done in conjunction with AFRL into the operation of RDEs visualized, with high speed imagery, the presence of a secondary detonation wave rotating approximately 180 degrees behind a main wave. This second wave was visually seen to be weaker than the main detonation wave [22] and was found computationally by Nordeen [16] in 2013 to be a secondary detonation wave traveling behind the main detonation combusting any detonable reactants left from the first wave. By treating the RDE as a control volume, any reactants that combusted outside of the detonation front, but still within the RDE were not counted as losses to the system [16].

In 2013 Chen et al. [8] performed research into impinging jets using high fidelity simulations. This research utilized Adaptive Mesh Refinement (AMR) to more accurately and efficiently simulate both low and high-speed impinging jet flows. Their simulations did not account for any turbulence, this was done as an error mitigation step. [8] This way the error induced by the turbulence model would not affect the simulation solution. Their results showed the impinging jets would interact and mix quickly with each other then break into ligaments and/or large droplets, and as the flow velocity of the jet was increased the break up of the jets became more unstable and lead to rapid atomization into droplets. [8] The simulation results showed to be dependent on the resolution of the mesh given droplets of a size below three times the size of the smallest cell in the mesh were discarded. [8] Chen et al. research reached a level of acceptable result as they were limited by resources on hand.

Pressure Drop in RDEs.

In a RDE it is important to understand the magnitude of the pressure changes throughout the detonation process. Detonations can produce pressures up to GPa, much higher than the yield stress of most conventional materials. Equation (3) shows the Chapman-Jouguet detonation pressure. Equations (3 - 6) were taken from Cooper. [9]

$$P_{CJ} = \frac{\rho D^2}{\gamma + 1} \tag{3}$$

$$D = 1.5 + \rho \left(\frac{D' - 1.5}{\rho_{TMD}} \right) \tag{4}$$

$$D' = \frac{F - 0.26}{0.55} \tag{5}$$

$$F = 100 \left(\frac{\Phi + \Psi}{MW} \right) - G \tag{6}$$

This pressure change is referred to as the pressure drop, because the upstream pressure must be higher than the chamber pressure to avoid hot, reactive, combustion products from being pushed into the fuel tanks and causing catastrophic failure. Looking back at Equation (1) from Section (2.2), it can be see $\dot{m}$ is a function of area, discharge coefficient, density, and pressure drop. Equation (7) shows this relationship per unit area.

$$\frac{\dot{m}}{A} = C_d \sqrt{2\rho \Delta p} \tag{7}$$

From Bergman et al. [7] and Anderson [5] Equations (8 - 21) can be formulated to yield an equation for discharge coefficient.

$$P_1 + \frac{1}{2}\rho V_1^2 = P_2 + \frac{1}{2}\rho V_2^2 \tag{8}$$

Equation (8) can then be rearranged to solve for V_2 yielding Equation (9) shown below.

$$V_2 = \sqrt{\frac{2(\Delta P - \Delta P_{viscous})}{\rho} + V_1^2} \tag{9}$$

The $\Delta P_{viscous}$ term here is the pressure drop due to viscous flow through a pipe.

$$\Delta P_{visc} = fl\frac{\rho U_m^2}{2D} = \frac{4\dot{m}}{\pi D^3}lf \tag{10}$$

Plugging in this formulation, the following equation can be formed.

$$\dot{m} = \rho A V_2 = \rho A \sqrt{\frac{2(\Delta P - \Delta P_{viscous})}{\rho} + V_1^2} \tag{11}$$

$$\dot{m} = \rho A V_2 = \rho A \sqrt{\frac{2\left(\Delta P - \frac{4\dot{m}}{\pi D^3}lf\right)}{\rho} + V_1^2} \tag{12}$$

$$A = \frac{\pi D^2}{4} \tag{13}$$

Therefore

$$\frac{\dot{m}}{A} = \rho\sqrt{\frac{2\left(\Delta P - \frac{\dot{m}}{AD}lf\right)}{\rho} + V_1^2} \tag{14}$$

Let

$$\zeta = \frac{\dot{m}}{A} \tag{15}$$

17

Therefore

$$\zeta = \rho\sqrt{\frac{2\left(\Delta P - \frac{\zeta}{D}lf\right)}{\rho} + V_1^2} \tag{16}$$

$$\zeta^2 = \rho^2\left[\frac{2}{\rho}\left(\Delta P - \frac{\zeta}{D}lf\right) + V_1^2\right] \tag{17}$$

$$\zeta^2 = 2\rho\left(\Delta P - f\zeta\frac{l}{D}\right) + \rho^2 V_1^2 \tag{18}$$

Complete the square

$$\zeta^2 + 2\rho f\frac{l}{D}\zeta + \left(\rho f\frac{l}{D}\right)^2 = 2\rho\Delta P + (\rho V_1)^2 \tag{19}$$

$$\zeta = \sqrt{2\rho\Delta P\left(\rho f\frac{l}{D}\right)^2 - (\rho V_1)^2} - \rho f\frac{l}{D} \tag{20}$$

Therefore, discharge coefficient as a function of pressure drop can be represented as follows in Equation (21).

$$C_D = \frac{\sqrt{2\rho\Delta P + \left(\rho f\frac{l}{D}\right)^2 - (\rho V_1)} - \rho f\frac{l}{D}}{\sqrt{2\rho\Delta P}} \tag{21}$$

Equation (21) shows as the pressure drop increases, the discharge coefficient should approach a constant value. This suggest the discharge coefficient, at a point, becomes independent of pressure drop. This is explored further in Chapter III. Commonly, V_1 is treated as being stagnant; therefore, eliminating a term in Equation (21). This assumption is not exactly correct; however, an analysis of this and the assertions leading to this assumption will be explored in Chapter III.

2.4 Additive Manufacturing

The use of additive manufacturing (AM) has gained popularity in the engineering world as a method for producing rapid prototypes or mock-ups. Sometimes referred to as 3D printing, AM is a method of manufacturing where an object is produced one layer at a time. This is unlike subtractive manufacturing, where material is removed from an originally larger block of material. With the advancements in printing capabilities, additive manufacturing has allowed for multiple revisions of a prototype to be built quickly and changes implemented before the final part production. Previously, parts requiring an intricate casting or manufacturing technique were not tested until the final implementation of all the components. This was due to the amount of time and money required to reproduce them, should something happen during multiple tests. AM has led to time and monetary savings throughout the design and build process.

There are two main categories of AM, plastic extrusion and powder bed fusion. Plastic extrusion consists of a spool of plasitc filament that is heated and extruded into the desired locations. Powder bed fusion is typically used for the manufacture of metallic components, and consists of using a high powered laser to weld metallic powder together forming the desired shapes. When manufacturing with metal, typically an inert gas (dependent on material) is used to fill the chamber to avoid any combustion events.[17] NASA, in an effort to build a full-scale AM rocket engine, found using a powder bed fusion technique reduced part count by 80% while reducing the requirements for configuration [14]. The use of AM allowed for an iterative design and build process by building prototypes and testing them before the critical design review stage of the project. AM allowed for the design and production of single element parts such as the injector element shown in Figure (4) all the way to parts as large as the fuel mixing pipe shown in Figure (5).

Figure 4. Additively manufactured single element injector [14]

Figure (4) shows a singular injector element for the rocket engine NASA was developing [14]. The injector elements are very small when compared to the fuel pipe shown in Figure (5). The fuel mixer pipe is shown with a ruler in the background giving context to its size. This particular pipe would be nearly impossible to produce through traditional subtractive manufacturing techniques.

Figure 5. Additively manufactured fuel mixer pipe [14]

With large, intricate parts, such as the fuel mixer pipe in Figure (5) or the C-5 end fitting in Figure (6), AM reduces the large amounts of waste generated from

traditional subtractive methods. The production of the C-5 fitting generated large amounts of material waste that had to be collected, processed, and typically sold to a third party organization to be transformed from waste into a usable material again [18]. The use of AM for this fitting could reduce the amount of waste by up to 90% [18]. Current research at the Georgia Institute of Technology is developing processes for the 3D printing of ceramics to be applied as molds for complex metal parts to be forged [18]. The ceramics are strong enough to withstand the intense heat of forging metals; however, are weak enough to be easily removed after the formation of the desired part(s).

Figure 6. Subtractively manufactured C-5 end fitting [18]

Additive manufacturing on the micro scale.

When manufacturing on the micro scale, AM has several drawbacks. Because the methods used for AM include wielding particles of a very fine powder together to create the shape desired, small imperfections are created unintentionally. Recent research done at the Air Force Institute of Technology by Tommila [24], studied

21

the implications of the surface roughness found with additively manufactured micro rocket nozzles. These effects are more prominent when manufacturing on the micro scale due to the effect the scale has on the Reynolds number. The Reynolds number is the relationship of viscous forces and inertial or momentum forces. The viscous forces have a much higher effect when the ratio of nozzle surface area to nozzle diameter is high. Simply put, a higher percentage of the flow is affected by the walls in a micro meter scale object when compared to a meter-scale object. This increased effect of viscous forces means the surface roughness plays a much larger part in determining the loss terms. Figure (7) shows the difference in a machined micro nozzle and an additively manufactured nozzle using a Direct Metal Laser Sintering (DMLS) method.

Figure 7. Machined micro nozzle (left) and DMLS Nozzle (right) [24]

In his research, Tommila examined several AM'ed nozzles, one of them is shown in Figure (8), showing the protrusions created through the DMLS process [24]. While these protrusions are only on the order of μm, their relative size to the diameter of the nozzle throat is what is important. These protrusions could lead to high viscous losses, turbulence, or the formation of shocks if the Mach number is high enough [24].

To improve the surface quality and reduce roughness there have been developments in machines combining AM and high-speed milling [17].
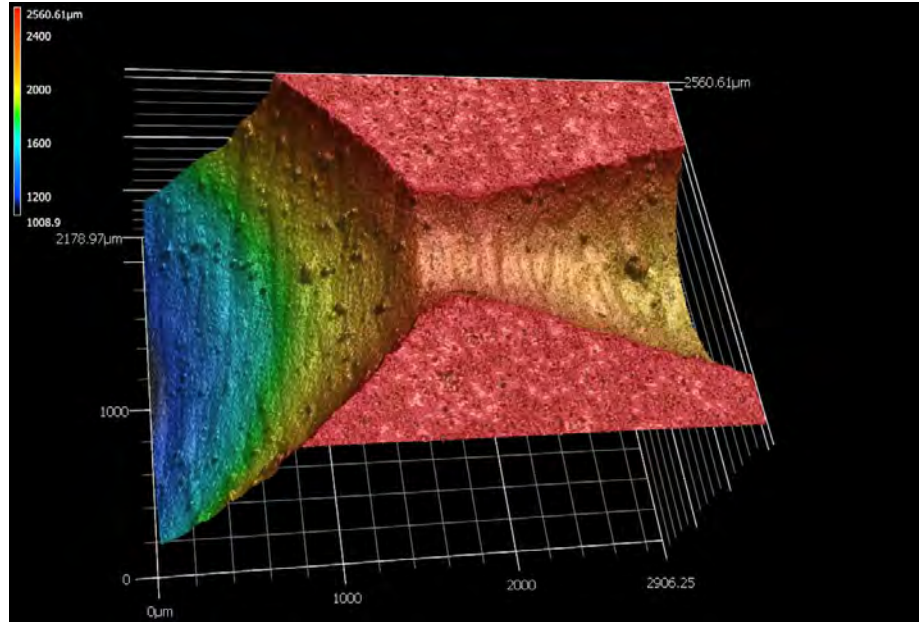
Figure 8. Laser Scanning Microscope image of AM rocket nozzle [24]

2.5   Literature Review Conclusion

Throughout development of technologies, higher efficiencies are typically a main goal along with reducing costs. The advent of additive manufacturing, as a means of development and prototyping, has led to the ability to reduce costs and save time. These savings lead to shorter development times as well as more intricate designs previously abandoned due to a lack of machining capability. The goal of this research is to discover the potential benefits of utilizing AM for injector elements in RDEs. Pressure-gain combustion allows for a higher efficiency [21] as has been demonstrated through comparison of constant pressure and constant volume combustion. RDEs operate through detonation combustion as a constant volume or pressure-gain combustion event. The injectors of the RDE have to be designed to allow for the mixing of the fuel and oxidizer in a minimal azimuthal distance. The detonation wave(s)

rotate around the annulus; therefore, the location of the 'top' (point closest to the injectors) of the detonation wave is controlled by the mixing of the fuel and oxidizer. This location also determines the overall length of the engine. Through the use of additive manufacturing, the design of the injection head and orifice can be redesigned to allow for a more compact, cheaper, and lighter system.

III Methodology

3.1 Introduction

Chapter II examined historical literature relating to this research and its need. This chapter examines the experimental theory and process, as well as examining the analytical theory and the experimental set up. This chapter discusses the validity of the models used in this research, their realms of relevance, and the assumptions made in order to use them.

3.2 Experimental Theory

This research used a two pronged analytical approach. First a computational analysis was carried out using fluent, as a part of Ansys Workbench 17.2. Using CFD it was possible to model geometries and gain insight to their respective flow characteristics without the cost of manufacturing. The CFD used, while useful in providing insight to the flow characteristics, is not exact. The exact surface roughness levels could not be modeled without already knowing the roughness levels of the printed parts. To alleviate this, the computational models were run using a variety of different roughness levels. The CFD also assumes uniform roughness, not accounting for the relatively large anomalies known to exist as was shown in Figure (8). These protrusions may be small on the scale of the entire element; however, relative to the surrounding roughness they can be quite large. After the computational analysis was performed the second prong of the analysis, experimentation, was conducted. The experiment involved flowing pressurized water though each element. The mass of water flowed was captured by measuring the mass of the collection container before and after the test. The mass flow rate as well as the discharge coefficient for each element was then calculated. This process was carried out for each design. This

combination of analytical techniques allowed for an efficient and cost-effective way of characterizing various geometries.

3.3 Model Theory

Figure (9) shows the stages of development for fluid flow along a wall or in a pipe. The first stage or set of arrows furthest to the left, shows the entry flow of the fluid before contact with any surface. The next set of arrows is marked by the velocity being a function of the x and r position and not being fully developed yet. The flow in this research is not fully developed and is in the region marked in Figure (9) as the hydrodynamic entry region. Typically for tube sections of $(x/D) < 10$ turbulent flow will not become fully developed. Turbulent flow is defined as having a Reynold's Number $> 10,000$ [7].
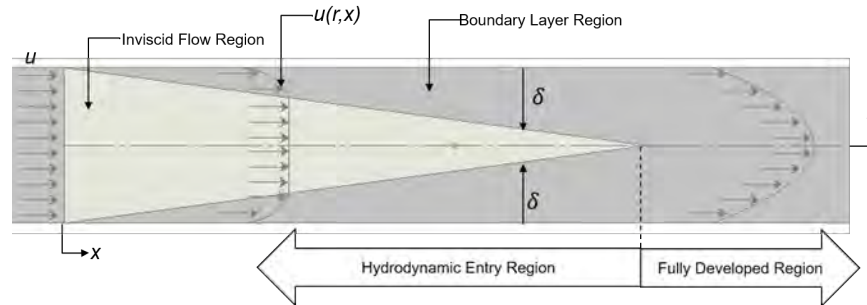
Figure 9. Velocity Profile Diagram[7]

The experimental analysis employed for this research used water as a propellant substitute. Water was used as a substitute because it is incompressible and non-reactive with any other materials used in this research. The use of water allowed for experimentation to be done multiple times for a drastically reduced cost compared to a live fire test as well as reducing safety concerns from flowing non combusting fuel. To gain insight to the magnitude of the pressure drop an open source software tool called CEARUN [11] was utilized to calculate the Chapman-Jouguet (CJ) detonation

pressure using the equations presented in Chapter II Section 2.3 Equations (3 - 6). This pressure is the ideal pressure rise generated from the detonation of a fuel.

CEARUN was used to analyze the detonation of Methane (CH_4) with pure (O_2), this is representative of a common rocket propellant fuel mixture [11]. The detonation pressure calculated by CEARUN was found to be 32.46 bar, the detonation velocity was found to be 2,532 m/sec. In a constant pressure combustion cycle, such as a typical liquid rocket engine, this pressure would act as the minimum back pressure to prevent hot combustion products from being forced back into the feed lines and potentially to supply tanks. With pressure gain combustion and a detonation wave the combustion products may be forced into the feed lines, but do not make it to the supply tanks causing system failure. This is because the detonation front is modeled as an instant pressure spike, and not a sustained pressure rise. As was mentioned in Chapter II Section 2.3, the discharge coefficient is expected to become independent of pressure drop. This behavior allows for a lower pressure drop to be examined while maintaining accuracy in the experiment.

Figure (10) shows the discharge coefficient as a function of pressure drop for fully developed flow in a tube with a 1mm opening. The figure compares the C_d for varying (15 micron and 100 micron) roughness heights. The figure shows the expected asymptotic behavior of the discharge coefficient, meaning for a high enough dP the discharge coefficient is constant. The figure also shows for a rough surface the C_d diverges from the smooth surface much sooner and is lower for all dP. This means the expected discharge coefficient of the AM elements is lower than the traditionally manufactured elements due to having a more rough surface.
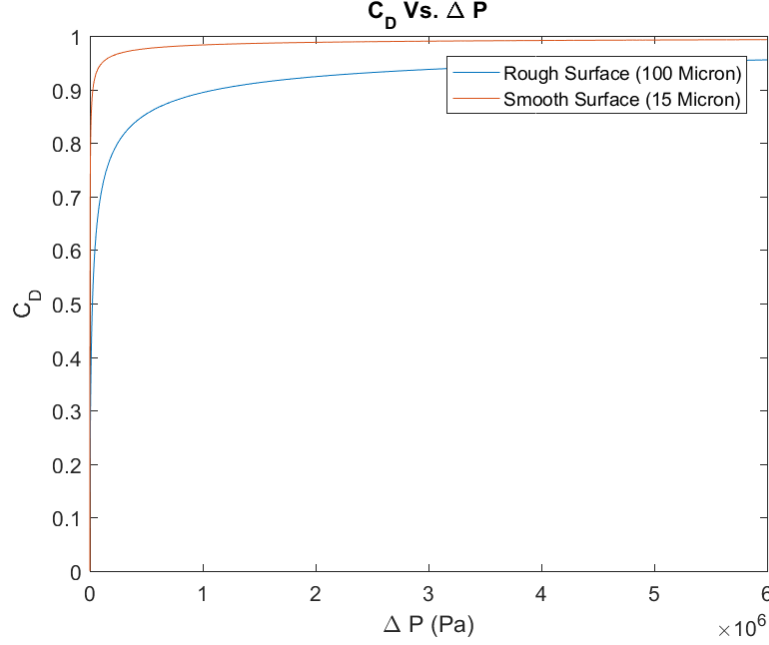
Figure 10. Comparison of C_d as a function of ΔP for a rough (100 micron) and a smooth (15 micron) surface

3.4 Experimental Materials and Equipment

Element Geometry.

The injector elements modeled in this research were modeled from designs presented by Sutton in Table (1). [23] Figure (11) shows a Computer Aided Design (CAD) of the sharp-edged cone element. CAD of the rest of the designs are located in Appendix 1. Appendix 1 also contains preliminary stress tests run using Solidworks ^TManalysis tools to determine if the pressures being exerted would be in danger of exceeding the yield stress of the elements.
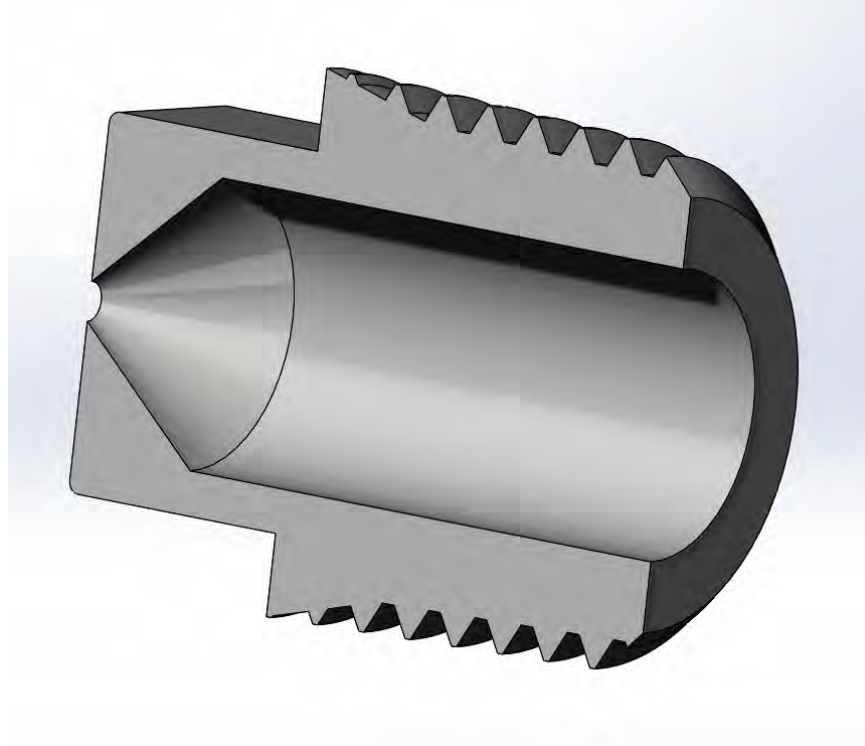
Figure 11. CAD of Sharp-edged Cone element [23]

Equipment.

The equipment needed for the experimentation portion of this research is not overly sophisticated; however, it is effective for gathering the data needed. First a source of pressure was needed, this was accomplished using a pressurized tank of inert Nitrogen. The pressure tank used to contain the water was a pressurized liquid tank rated to 205 PSI. The Nitrogen tank was regulated to 180 Psi for this research using a pressure regulator attached to the tank. Other materials included several feet of 1/4" stainless steel tubing, three swagelok ball valves, a 1L Polyethylene terephthalate (PET) container, and finally a scale to measure the mass of the water in the outflow container after each test. The accuracy of the scale used was $\pm 0.5g$, to mitigate this error a minimum of 100g of water was flowed through each of the elements. The time required to flow this amount of water was calculated using the CFD results for mass

flow rate. The pressure transducer was placed as close as possible to the outflow region to account for the maximum amount of pressure drop in the tubing. There was still pressure drop in the remaining tubing until the outflow area, this loss was quantified using the following equation. The pressure drop due to the tubing between the pressure transducer and the outflow was found to be 0.138 PSI including the 90 degree bend and the straight sections of tubing, Equation refe:Pdrop was used for this calculation [1]. The figures below (12 and 13) show the design for the lab set up as well as the actual lab setup used for this experiment. In Figure (13) the outflow of the setup can be seen on the left side of the image pointed down with a ball valve to control the start and stop of each run. The flow meter pictured in the lab setup as well as the lab image was not used for this experiment, yet was utilized in unrelated research using the same lab setup.

$$\Delta P = \frac{fLv^2}{2Dg} \tag{22}$$
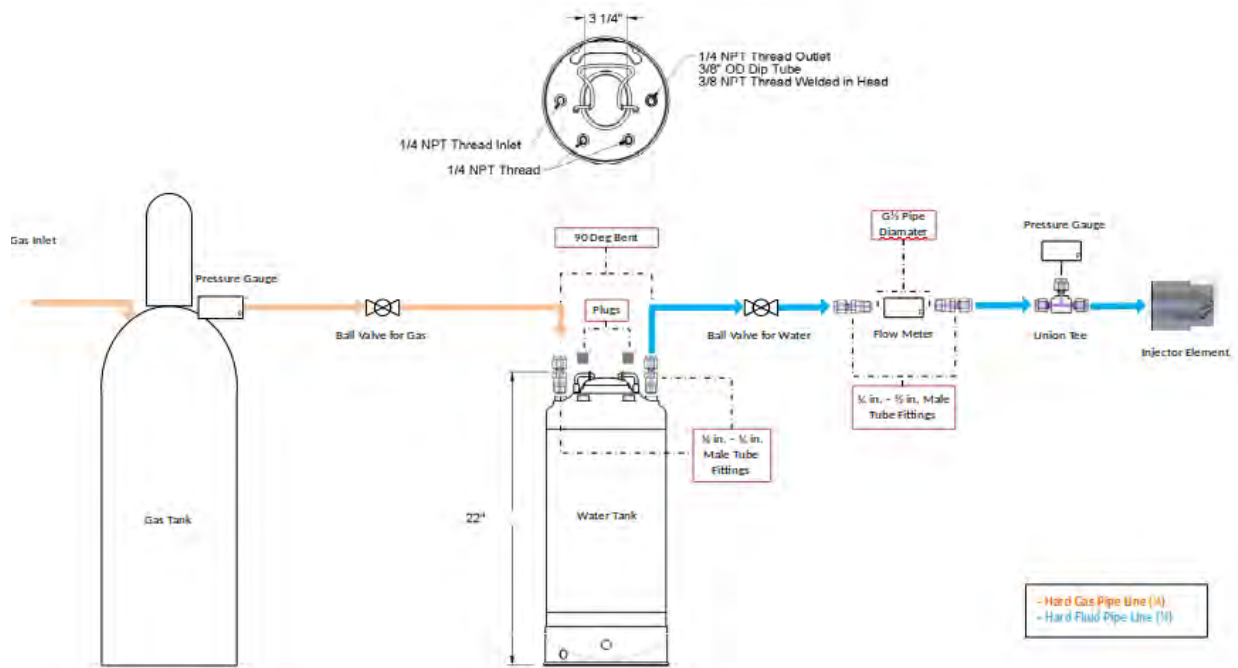
Figure 12. Piping Schematic

Figure 13. Lab Setup

3.5   Analysis Procedure and Process

The analysis performed in this research was broken into two types: computational and experimental. The computational analysis was used to model the flow and predict values to be seen in the experimental analysis.

Computational Analysis.

Ansys Fluent 17.2 was used for all computational analysis. The use of CFD allowed for the analysis of multiple geometries under different conditions in order to determine the need for experimental testing. The computational analysis followed a relatively simple process starting with the design of each element to be investigated. The designs chosen were previously shown and discussed in Table (1). It was determined,

due to the symmetry of the designs, a 2D simulation would be appropriate for these purposes. The next step was to generate a mesh for the designs using the built-in meshing software in Workbench 17.2. Figure (14) shows the mesh used for one of the designs. In the figure, the direction of flow is from left to right with the area to the right of the throat channel simulating outflow to ambient conditions.
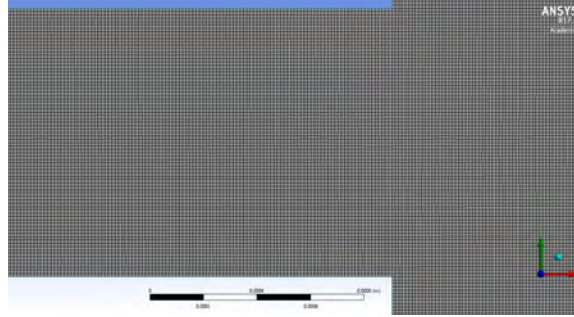
Figure 14. 1mm throat mesh

The next step was to set up and run the simulations. Using Fluent, simulations were carried out for each independent design. Simulations for each design were then run at varying surface roughness levels and pressures. The reason for running multiple pressures was to confirm discharge coefficient changing independent of the pressure change. Table (3) below shows some of the settings unchanged from run to run no matter the pressure or roughness height. The average mesh size indicated the number of cells in the 2D mesh used. The decision to use a turbulent intensity of 4 % was based on the Reynolds number in the flow, along with a projected hydraulic diameter. Equation (23)[2] shows the calculation of the turbulence intensity, where Re is the Reynolds number of the flow and D_h is the hydraulic diameter of the opening. The roughness constant listed as 0.5 was chosen to model uniform sand grain roughness, this was an assumption that the printed surfaces would have some level of uniformity in their respective roughness levels. Convergence criteria was the residual of the Navier-Stokes energy equation set to $1e^{-6}$.

33

$$T_{intensity} = 0.16Re^{(-1/8)}D_h \qquad (23)$$

Table 3. Mesh and Roughness settings

Mesh Size (average cells)	Turbulent Intensity	Roughness Constant	Y^+	Cell Size at Throat Y direction (microns)
269,728	4%	0.5	0.248	12.5

Experimental Analysis.

The experimental analysis performed for this research consisted of manufacturing multiple test articles representative of known geometries with historical data. The number of test articles produced was calculated using a T-Distribution and a 95% confidence level, this came to having five articles or elements produced of each design. Using the same code written to calculate the number of elements needed, the number of runs needed for a 99% confidence level was determined to be seven. This means each of the 20 total elements was tested seven times.

The procedure used to test each element is as follows:

1. Set pressure regulator on inert gas fill tank to desired pressure

2. Weigh outflow tank for empty weight

    Used for calculating mass flow rate

3. Attach the element to the water output from the pressure tank

4. Start data collection

5. Open ball valve to start flow of pressurized water

6. After the minimum amount of time close the valve halting the flow of pressurized water

7. Stop data collection

8. Weigh outflow container

    Refill pressure tank (if needed)

9. Repeat 7 times for each element

All elements were tested at a single pressure (180 psi). One element from each design was tested at an additional four pressures to experimentally show the independence of C_d to pressure and to make sure the mass flow rate varied as expected with the square root of the pressure drop.

3.6 Data Analysis

The data gathered from both the CFD as well as the experimental results had to be compared and evaluated equally. The results from the CFD had to be analyzed slightly differently than those of the experimental runs. The CFD was run to a steady state solution; therefore, had to be probed for velocity values of the fluid and at particular position in the domain. Therefore, the mass flow rate had to be calculated given the density, velocity, and the area of the opening using equations presented in Chapter 2. The Reynolds number was calculated using Equation (24). The hydraulic diameter shown in Equation (25) is a function of area as well a perimeter. These values were calculated for the CFD easily given the model is a perfect circle. The experimental elements; however, were not perfect and microscope imagery was used to measure the area and perimeter of each element.

$$Re = \frac{\rho v D_h}{\mu} \tag{24}$$

Where:

$$D_h = \frac{4A}{Perimeter} \tag{25}$$

After the discharge coefficient, mass flow rate, and Reynolds number were calculated for each design, roughness level, and pressure; they were compared and plotted according to their respective designs. The experimental results data consisted of a time accurate pressure sampling at a rate of 1000 Hz. This allowed for the pressure as well as the run time to be pulled from the data. With this information the mass flow rate could be calculated. Each element was imaged under a microscope to accurately calculate the area and hydraulic diameter of the orifice because each element was unique in their exact dimensions. This uniqueness meant each element needed their data to be analyzed using measurements respective to the element. Once all of the data were calculated for each element as well as the multiple pressures, the data were tested to see if it were normally distributed. This was done by testing to see what percentage of the data fell within 1, 2, and 3 sigma. For normally distributed data, 68 % of data falls within 1 sigma, 95 % of data falls within 2 sigma, and 99.7 % of data falls within 3 sigma [15]. Once the data were determined to be considered normally distributed, the standard deviation, mean, and variation of the data could be calculated and presented.

3.7   High Speed Imagery

One element from each design was imaged using a Phantom V12.1 high speed camera. The settings of the camera for each test are listed in Table (4).

Table 4. High speed camera settings

Resolution	1280x800
Sample Rate (fps)	4,000
Exposure Time (μs)	50

Figures (15 and 16) show the setup used for gathering the high speed imagery. The Plexiglas tube was used to eliminate any splashing of water back onto the camera. The window was used to provide a flat and clear surface to view through instead of the curved tube that would have distorted the view. Figure (16) shows a closer view of this setup.

Figure 15. High speed imagery setup

Figure 16. Close up view of high speed camera setup

The visualization of each of the injector elements consisted of 1,000 frames or 0.25 seconds. The frames were then processed using a software known as ImageJ. The maximum image, or the image representing the maximum intensity of each pixel in every frame was generated to show the flow field.

After the conclusion of all testing, two elements were chosen to be sliced in half

and examined using both an optical microscope and a laser scanning microscope. One element from Designs 2 and 4 were chosen to be sliced in half. These two designs were chosen due to their geometry. Each of these designs have unique features such as the diverging and converging sections of Designs 2 and 4 respectively. However, these designs also have features in the other two designs such a "tube" section on Design 3 and 4. The elements were sliced in half using an IsoMet 5000 linear precision saw.

IV Results

Within the computational results section of each design is a corresponding CAD image of the design. Each section will refer to the respective design as Design 1, 2, 3, or 4. In all images, the fluid flow is from the left to the right.

There were four main objectives for this research. First, to measure the mass flow rate of injector elements. Second, to calculate the discharge coefficient of injector designs using both computational and experimental techniques. Third, to compare the found discharge coefficients of both techniques to each other as well as historical data. Finally fourth, to visualize the flow through AM injector elements. As has been described, this research tested four designs, each with geometric properties different from the rest. Figure (17) shows the CAD drawings of all four designs side by side. All designs were manufactured with he opening first, this will be discussed later in this chapter. As shown there are similarities with some of the designs such as Designs 1 and 2 both demonstrating a thin (L/D $\approx$ 0) while Designs 3 and 4 demonstrate the effects of L/D ¿ 0.
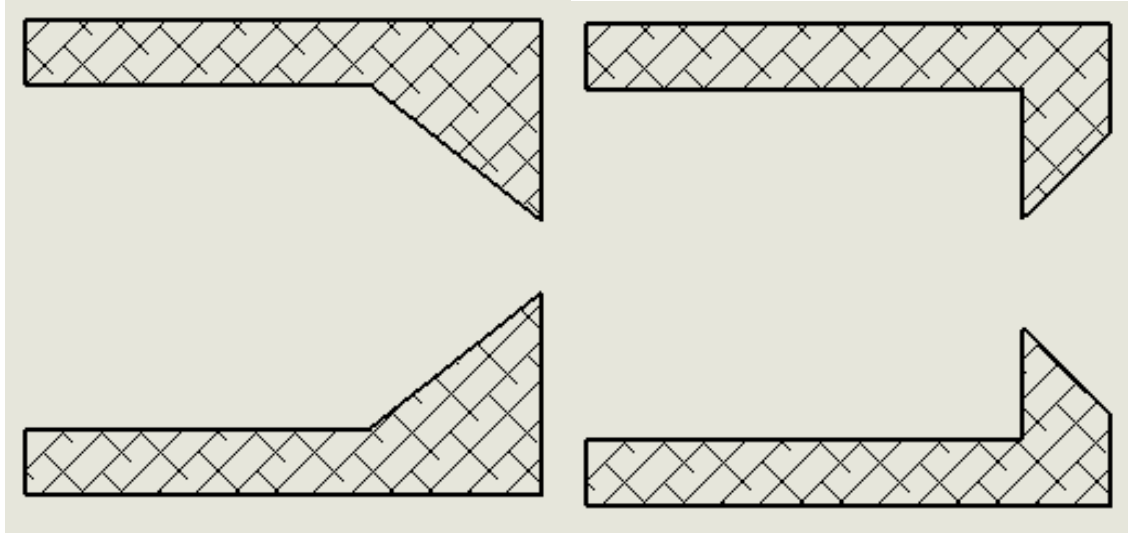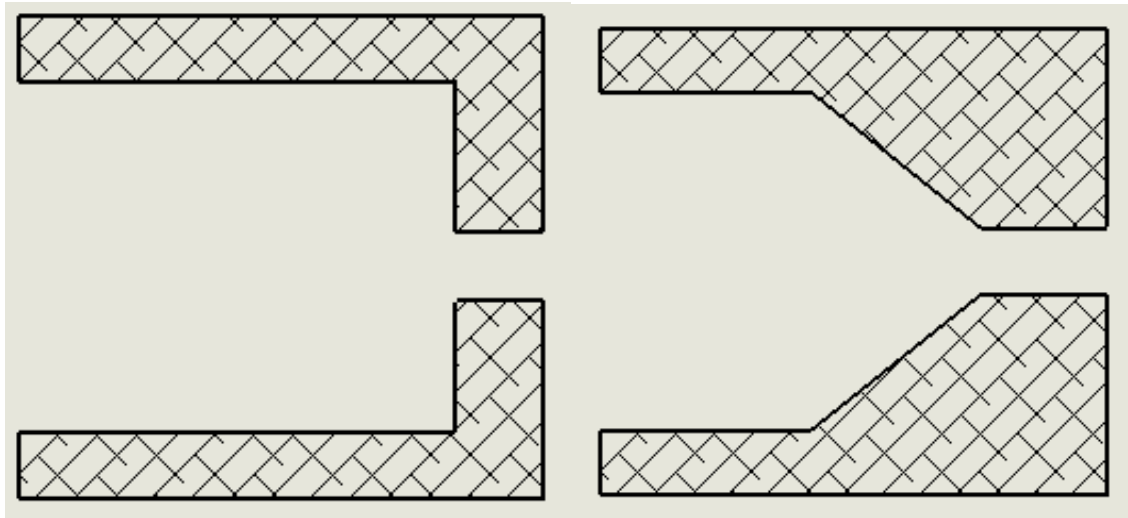
Figure 17. CAD drawings of all four designs, Design 1 (a), Design 2 (b), Design 3 (c), Design 4 (d)

4.1   Computational

All computational modeling was based on a perfect circular geometry with a 1mm throat diameter. This is the exact same as the CAD drawings shown above in Figure

(17).

Design 1.
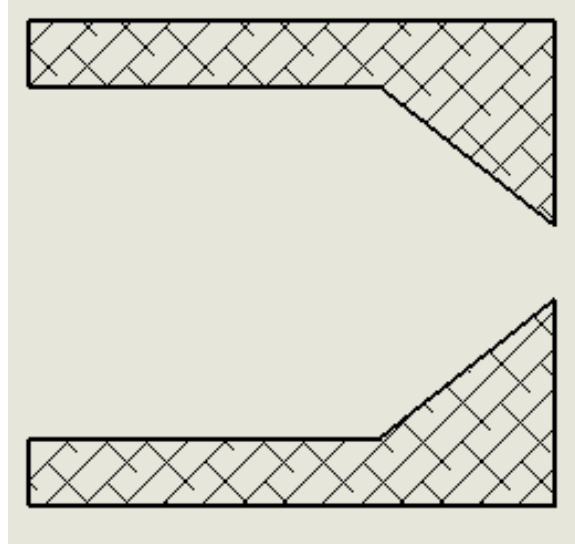
Figure 18. Side view of CAD for first set of injectors

Design 1, shown in Figure (18), is similar to a traditional converging nozzle. The sharp edges at the throat cause the flow to accelerate around them. Given the opening is a sharp edge, the effect of relative roughness for this design is low compared to some of the other designs. Figure (19) below, shows the velocity profiles across the throat of the injector at varying surface roughness heights of 0 microns to 300 microns. The figure shows the difference in flow velocity radially across the throat is very low as expected. Table (5) shows the differences numerically between the different roughness levels. The discharge coefficient was calculated from mass flow rates gathered from Fluent. As discussed, this design was not highly affected by the roughness level in velocity, mass flow, Re or Cd.
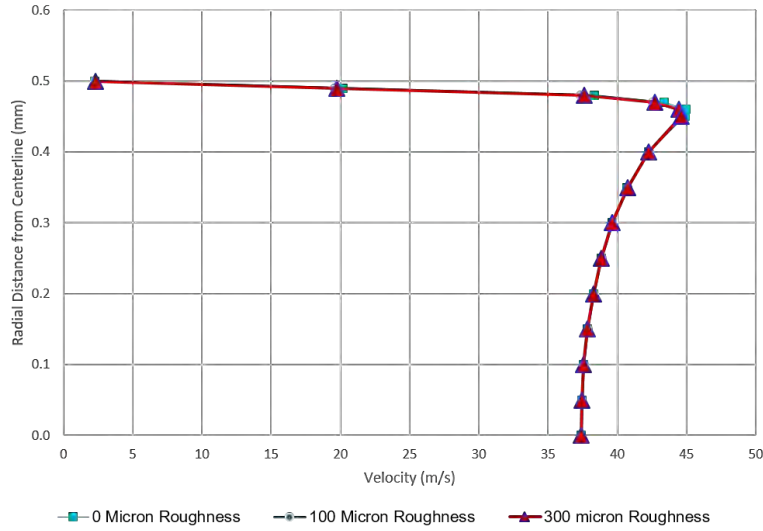
Figure 19. Comparison of velocity profiles at the throat for injector Design 1 at varying surface roughness

Figure (20) shows a contour plot of the velocity for injector Design 1. Given the design does not have a tube section, the flow has no time to become fully developed therefore is shown to have a faster core section after the opening. This core flow extends several opening diameters past the injector face and in a rocket engine would allow the combustion event to be offset from the injector face. This offset would aid in managing the thermal conditions of a rocket engine.
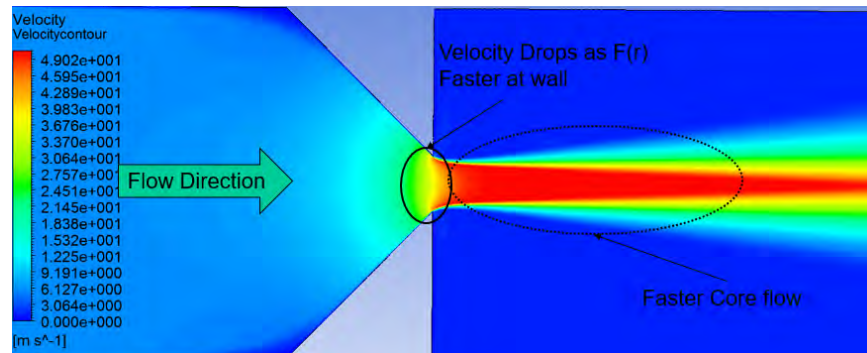
Figure 20. Velocity contour of Design 1

44

Table 5. Design 1 CFD Data

Roughness (micron)	Average Velocity (m/s)	Change from 0	Mass Flow (g/s)	Change from 0	Re (avg)	Change from 0	Cd	Change from 0
0	39.10	-	30.67	-	43,677	-	0.77	-
100	38.99	0.25%	30.59	0.25%	43,566	0.25%	0.74	0.25%
300	38.99	0.27%	30.59	0.27%	43,560	0.27%	0.74	0.27%

Table (6) shows a direct comparison of the Reynolds number, mass flow rate, and minimum test run time for the first design of injector elements. As has been discussed, the values do not vary much with the increase in surface roughness.

Table 6. Condensed Design 1 CFD data

Roughness	Re	Mass Flow (g/s)	Time (s) for 100g
0	43,677	39.10	3.26
100	43,566	38.99	3.27
300	43,560	38.99	3.27

Design 2.
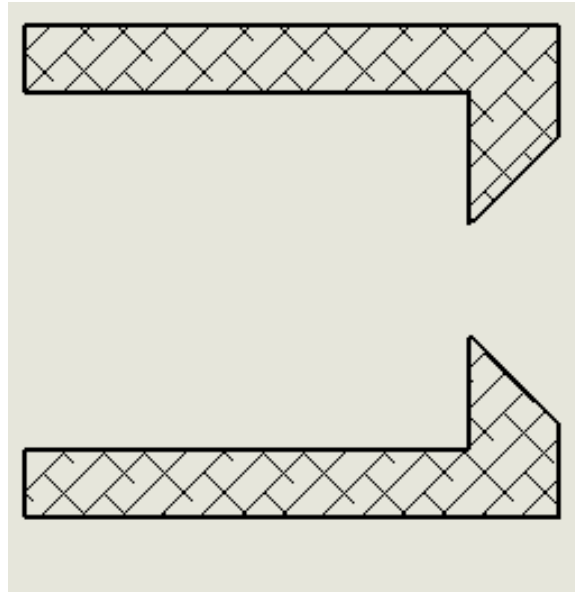
Figure 21. Side view of CAD for second set of injectors

Unlike Design 1 previously discussed, Design 2 has no converging section. This means the flow has to hit the wall inside the injector and then accelerate drastically as it flows through the opening. The flow not going through the opening enters a small recirculation region located in the interior corners of the element. However, instead of just an opening there is a diverging section as the flow exits the injector. This diverging section causes areas of increased velocity just past the throat. These same locations on Design 1 were shown to have a zero or near zero velocity. Having an above zero velocity means there is spraying off to the sides, this could lead to better mixing and possibly reducing the combustion's offset from the injector face. This design still has the strong core flow as was shown in the Design 1 results. The non-zero velocity in these locations is also an indication of higher vorticity occurring in these locations.
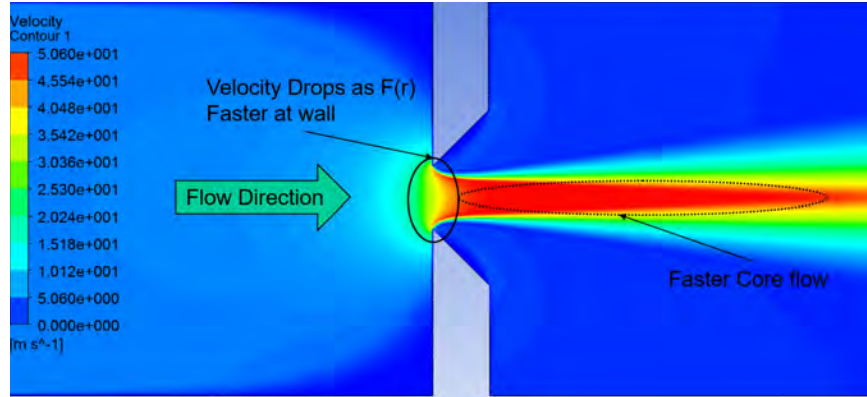
Figure 22. Velocity contour of Design 2
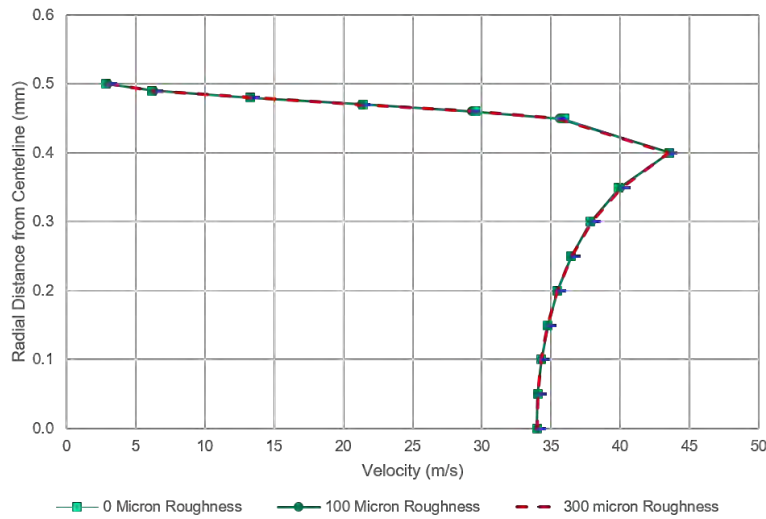
Figure 23. Comparison of velocity profiles for injector Design 2 at varying surface roughness

As was shown with Design 1, the velocity profiles shown in Figure (23) reveal little to no change due to roughness level. Table (7) actually shows the differences among roughness levels to be less than one-hundredth of a percentage. This little change was expected given the geometry of the design. It is important to note the change in geometry also changed the discharge coefficient seen by 0.1.

Table 7. Design 2 CFD data

Roughness (micron)	Average Velocity (m/s)	Change from 0	Mass Flow (g/s)	Change from 0	Re (avg)	Change from 0	Cd	Change from 0
0	34.29	-	26.90	-	38,306	-	0.65	-
100	34.27	<0.1%	26.88	<0.1%	38,280	<0.1%	0.65	<0.1%
300	34.28	<0.1%	26.88	<0.1%	38,286	<0.1%	0.65	<0.1%

Table 8. Condensed Design 2 CFD data

Roughness	Re	Mass Flow (g/s)	Time (s) for 100g
0	38,306	34.29	3.72
100	38,280	34.27	3.72
300	38,286	34.28	3.72

Design 3.
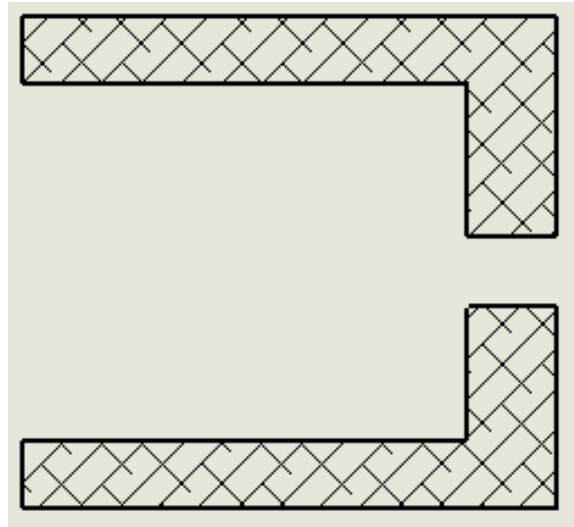
Figure 24. Side view of CAD for third set of injectors

The geometry of Design 3 replicates what would happen if a hole were to be drilled into the plate for the injector element. This design allows for the flow to be affected by the surface roughness more than the previous designs. Figure (25) shows the velocity contour plot for Design 3. The figure shows the flow just past the throat is faster in the middle than the walls where it is nearly stagnant. This is because the flow must turn the corner and enter the tube at the throat. The stagnant regions of fluid at the start of the throat, indicate the flow is not fully developed and comparing Figure (26) with Figure (9) shows this to be correct. The tube section of the throat would need to be several times longer to reach the needed L/D > 10 for the flow to become fully developed. This design does not have the same high speed core flow after the outflow found in Designs 1 and 2. This behavior is seen because the flow is starting to develop in the tube section of the design.
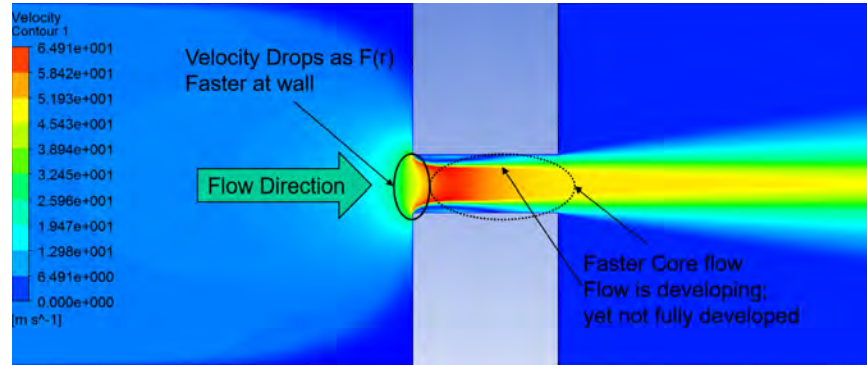
Figure 25. Velocity contour of Design 3
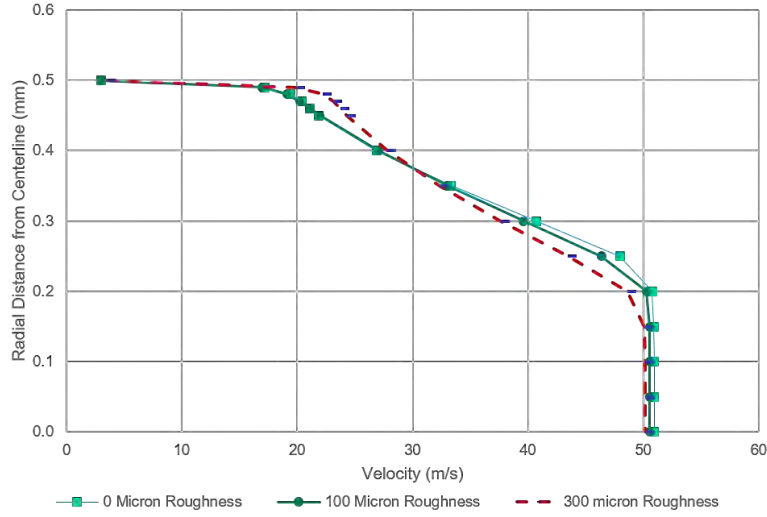
Figure 26. Comparison of velocity profiles for injector Design 3 at varying surface roughness

As shown in Figure (26) the velocity profiles indicate little change between the 0 micron roughness and the 300 micron roughness levels. This suggests the dependence on surface roughness is small; however, larger than the dependence shown by Designs 1 and 2. Table (9) shows the change between 0 and 300 micron roughness height is 1.2%. This difference is due to the presence of the tube section at the throat. This tube section, because the diameter is much smaller than the inlet area, has a much higher relative roughness. The relative roughness is the main cause of viscous losses in this situation.

Table 9. Design 3 CFD data

Roughness (micron)	Average Velocity (m/s)	Change from 0	Mass Flow (g/s)	Change from 0	Re (avg)	Change from 0	Cd	Change from 0
0	34.35	-	26.94	-	38,372	-	0.69	-
100	33.93	1.22%	26.61	1.22%	37,903	1.22%	0.68	1.22%
300	33.94	1.19%	26.62	1.19%	37,913	1.19%	0.68	1.19%

50

Table 10. Condensed Design 3 CFD data

Roughness	Re	Mass Flow (g/s)	Time (s) for 100g
0	38,372	26.94	2.86
100	37,903	26.61	2.86
300	37,913	26.62	2.86

Design 4.
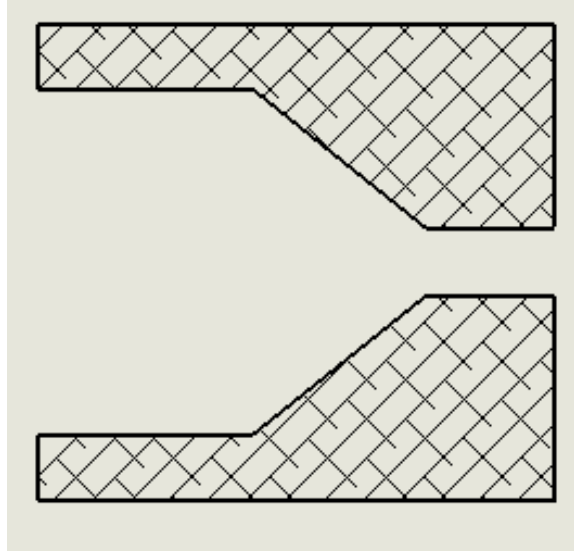
Figure 27. Side view of CAD for fourth set of injectors

Design 4 has a geometry similar to that of Design 3, now with a converging chamfer leading to the throat instead of the previous 90 degree wall. This converging section makes the design similar also to Design 1 now with a tube section. This converging section led to the flow being more developed and having to accelerate less around the corners of the throat leading to a higher overall discharge coefficient.
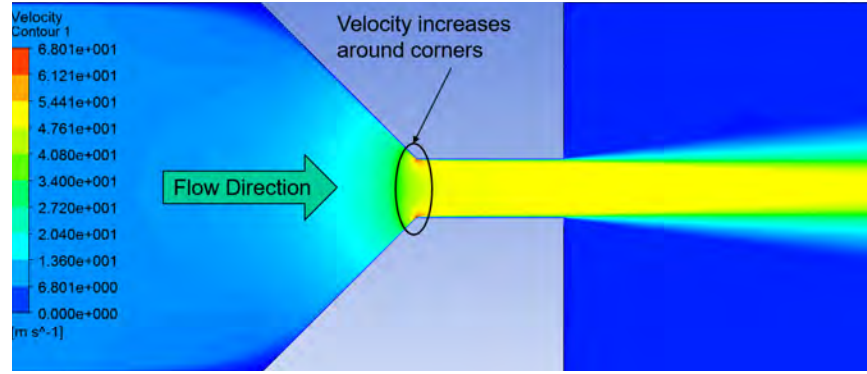
Figure 28. Velocity contour of Design 4

Figure (28) shows the velocity contours resulting from the CFD simulations for Design 4. This figure shows the acceleration of the flow around the corners at the throat, more fully developed flow, and a more uniform core flow post orifice opening. Each design previously shown has a distinct center core flow faster than the rest of the fluid flow; however, with this design the core flow is more uniform in velocity. Figure (29) shows the velocity profiles for Design 4 at multiple surface roughness levels. This design was run with more roughness levels because the difference between 0 and 300 micron roughness was so large in comparison to the other designs. The additional roughness levels show the effect of increased roughness as none of the other designs have so far. The variation shows how the increased roughness could be causing an increase in the size of the viscous boundary layer. This boundary layer formation would be what is depicted in the movement of the roughness lines. Table (11) shows the results of CFD simulations for the multiple roughness levels. The table shows there is a 7% change from the 0 micron level to the 300 micron level.
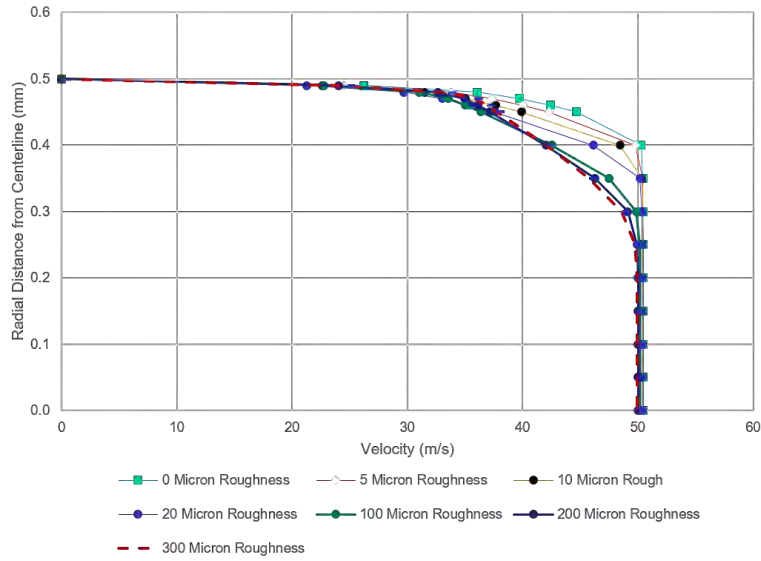
Figure 29. Comparison of velocity profiles for injector Design 4 at varying surface roughness

Figure (30) shows the same data as presented in Figure (29) simply with fewer roughness levels so as to better see the difference in the levels.
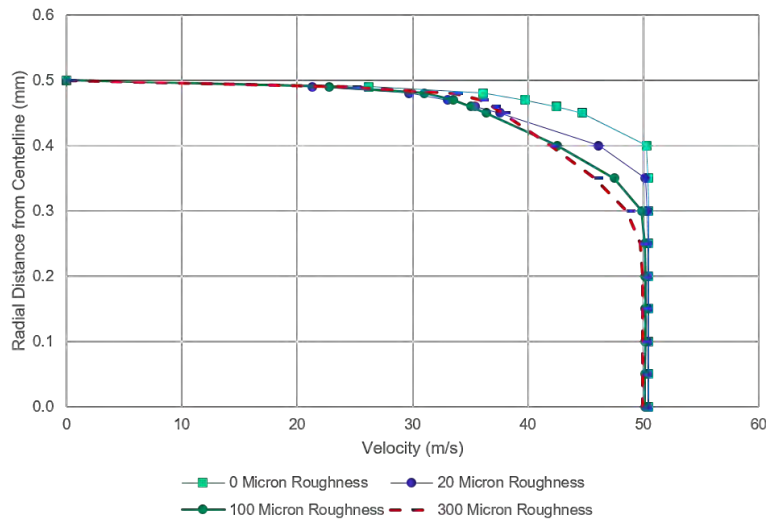
Figure 30. Comparison of velocity profiles of Design 4 at four surface roughness levels

Table 11. Design 4 CFD data

Roughness (microns)	Velocity (average) (m/s)	Change from 0	Mass Flow (g/s)	Change from 0	Re (average)	Change from 0	Cd	Change from 0
0	46.624	-	36.57	-	52,085	-	0.89	-
5	45.953	1.44%	36.04	1.44%	51,334	1.44%	0.87	1.44%
10	45.136	3.19%	35.40	3.19%	50,423	3.19%	0.86	3.19%
15	44.568	4.41%	34.96	4.41%	49,788	4.41%	0.85	4.41%
20	44.206	5.19%	34.67	5.19%	49,383	5.19%	0.84	5.19%
100	43.115	7.53%	33.82	7.53%	48,164	7.53%	0.82	7.53%
200	43.011	7.75%	33.74	7.72%	48,048	7.75%	0.82	7.75%
300	43.027	7.72%	33.75	7.72%	48,067	7.72%	0.82	7.72%

Table 12. Average Design 4 CFD data

Re	49,662
Mass Flow (g/s)	34.87
Time (s) for 100g	2.96
Volume (ml)	100.13

Figure (31) shows the relationship of discharge coefficient with surface roughness for Design 4. The figure shows the behavior for the discharge coefficient to remain constant after a certain (100 micron in this case) roughness level.
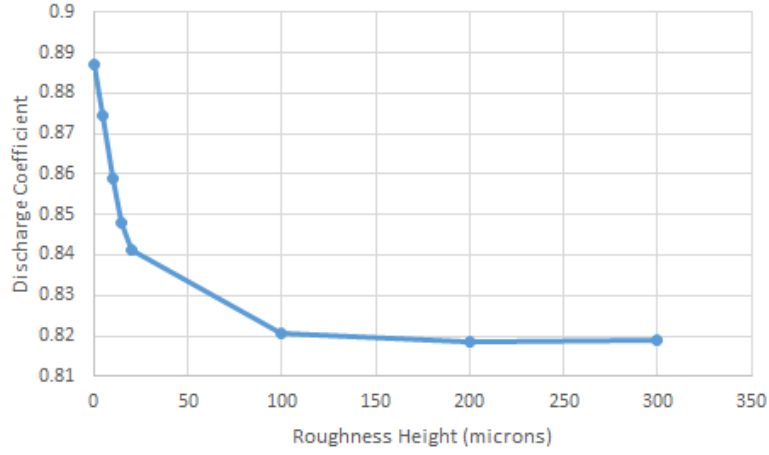
Figure 31. Cd as a function of the surface roughness height
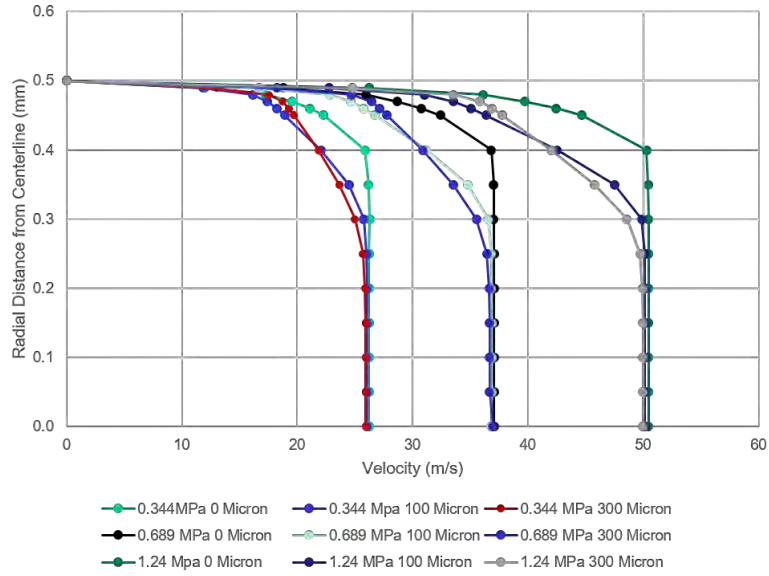
Figure 32. Comparison of velocity Profiles Design 4 at varying surface roughness levels (0-300 micron) and pressures

Figure (32) shows the velocity profiles of design four simulations run at three different pressures. This was done to confirm the results were independent of the pressure drop. The figure shows the results for 0.344 MPa, 0.689 MPa, and 1.24 MPa. The results show the same behavior as the previous test pressure with only a slight

variation in the 100 and 300 micron roughness at the 0.344 MPa level. This slight variation is non-worrisome given at this level of roughness the plots have indicated the velocity profile is nearly independent of roughness height.

4.2 Experimental

Each of the designs was printed with five copies to account for the variability in additively manufactured parts, improving the reliability of the results. All designs were printed oriented such that the throat opening was down. After printing, the injectors were still attached to the build plate and had to be removed from the build plate. The elements were printed with a slight amount of standoff material from the build plate to facilitate removal. Additional grinding or sanding was required to expose the orifice. This was acheived through the used of an electric belt sander. Figures 33 and 34 show a comparison of before and after additional post processing for one of the injector elements. Figure (35) shows a picture of a typical situation where the opening of the injector was completely covered with build material after being cut from the build plate. After the excess material was removed with sanding, each element was viewed under a microscope. Using an optical microscope, an image of the injector orifice was taken and used to calculate the true area of the orifice printed. The images for each design are shown in the design's respective section. The image was imported into Matlab where it was converted into a binary black and white image based of a threshold darkness level. This threshold was obtained by using a histogram of the brightness of each pixel in the original image. From this, now black and white image, the number of white pixels (the ones representing the orifice) could be counted and multiplied by a known conversion factor of square micrometer/pixel ($4.203\mu m^2$/pixel) . The following sections discuss each design independently as well as any variation between the CAD model and the final printed parts. The holes printed

in each injector element are not perfectly round nor are they the perfect dimensions depicted in the CAD. The design data referred to in the following tables are the data calculated using a perfect radius of 0.5 mm or equal to that in the CAD.

Figure 33. Design 2 before sanding process
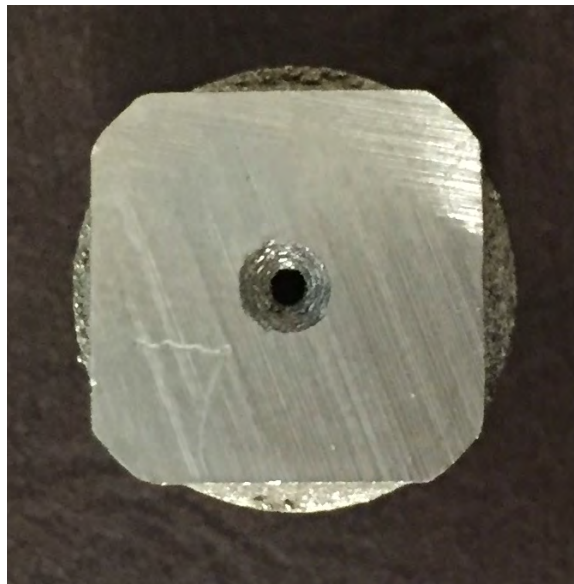
Figure 34. Design 2 after sanding

Figure 35. Blocked opening before sanding

Design 1.

Figure (36) shows the multiple images associated with the design elements. The original image shows the lighting of the microscope made it imperative to take the histogram and create a threshold for each image. The binary image shows this method worked to separate shadows from features in the image. By detecting the change in the binary image from black to white, the perimeter was found. Figure (37) shows the perimeter of Element 2. The figure shows the opening is not circular when viewed at this level of detail.

Figure 36. Original image in upper left shows the image captured by the microscope. Binary image in lower left shows the image after converting to pure black and white using threshold obtained from the histogram in upper right. Lower Right shows the detected surface of the opening
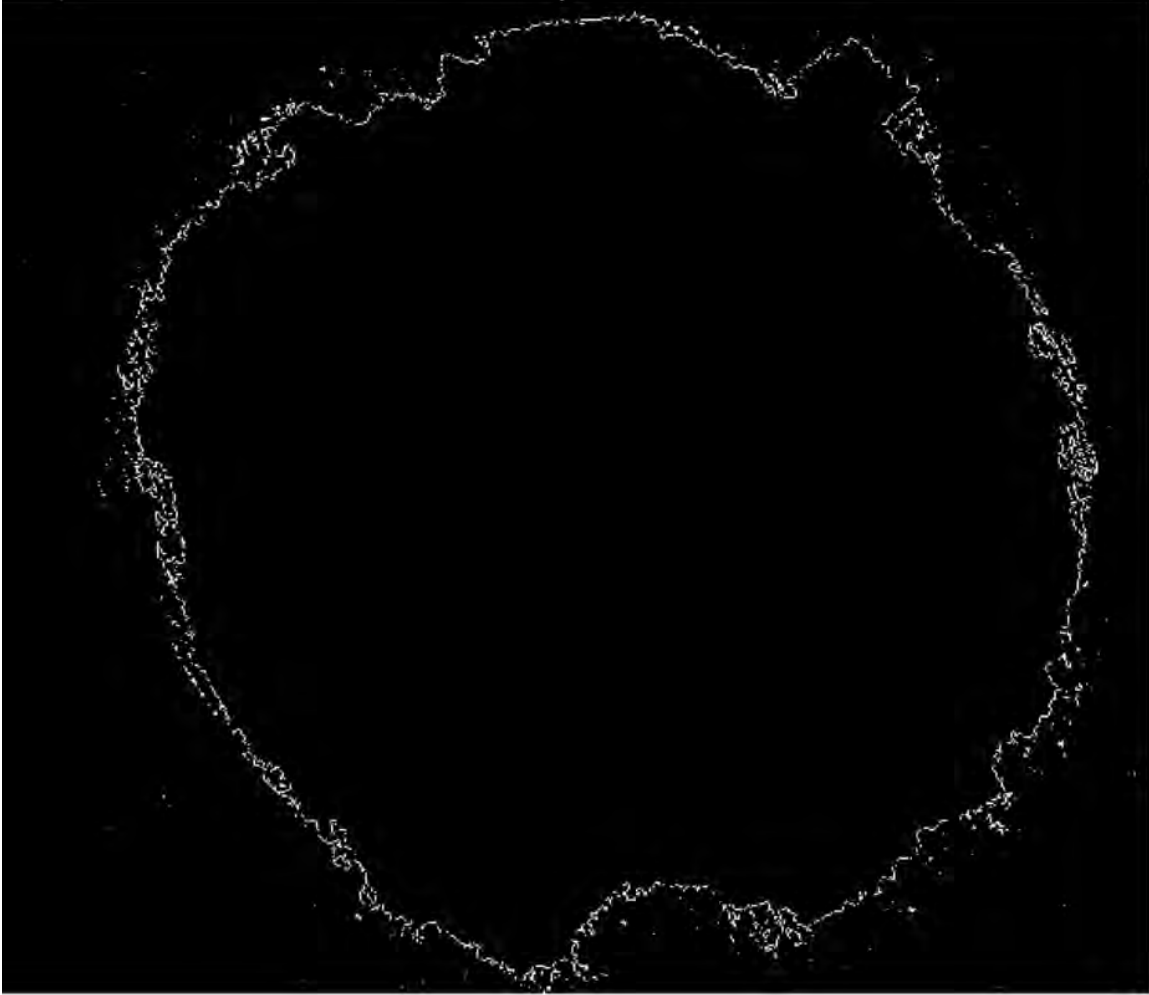
Figure 37. Detected perimeter of Element 2

Figure (37) shows the perimeter of Element 2. The image shows the variation of the opening from being circular. The variation in the opening causes a much higher perimeter to be calculated for the orifice. Each of the small cavities cause viscous losses in the flow because they are predominately comprised of boundary layer formation. These boundary layer areas do not contribute fully to the flow through the orifice; therefore, it reduces the effective area of the opening and skewing the calculations for discharge coefficient as well as hydraulic diameter.

Table (13) shows the results of calculating the area of the orifice for each of the

elements in the 1st design set. As shown in the table, the number 2 element is an outlier and had too much material removed during the sanding process.

The reason for the large change from design data is due to the geometry of the design. When looking at the 1st design (shown in Figure (18)), given the angle of the throat is 45 deg, over sanding by 0.2 mm accounts for the error seen with element number 2. This level of variation in orifice size was not seen in the other designs. This is because Design 1 was vulnerable to over sanding more so than the other designs. The geometry coupled with the build direction of the elements meant many of the elements of Design 1 had completely blocked openings until sanding revealed the exit plane face. The table also shows the perimeter measured for each of the elements. This perimeter was measured using the ratio of pixel size to physical distance, similar to the process for calculating the area of the openings. This perimeter was used to calculate the shown hydraulic diameter using Equation (25)

Table 13. Data from first design using microscope imagery

Number	Area (mm^2)	Change from Design (%)	Hydraulic Diameter (mm)	Perimeter (mm)
Design	0.785	-	1	3.14
1	1.077	37	0.634	6.79
2	1.563	99	0.515	12.14
3	1.021	30	0.628	6.49
4	1.073	37	0.862	4.98
5	1.170	40	0.757	5.81
Average	1.167	49	0.679	7.24
Avg without Elemnt 2	1.068	36	0.721	6.019

Figure (38) shows the discharge coefficient for each run of the elements of Design 1.

The data points represented in the figure are the averages for each set of tests where the error bars represent the variation in the results. The plot shows an expected drop in the Cd due to the increased surface roughness associated with the additive manufacturing process. From the plot, it can be understood the average discharge coefficient of the AM injector elements is ≈ 0.1 lower than that of the discharge coefficient in the *Rocket Propulsion Elements* text. The plot also shows the expected variation from element number 2 due to the increased variation from a true circular opening. It is important to note the variation in all of the elements from this design as a result of the geometry and its vulnerability to over sanding during processing after the printing process.
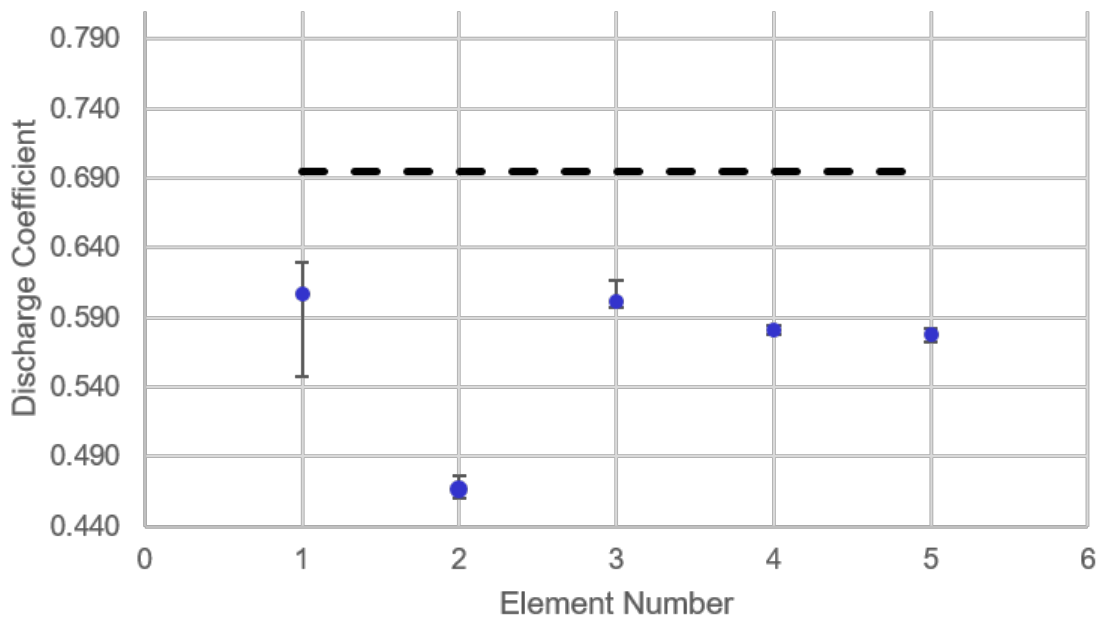
Figure 38. Comparison of Discharge Coefficient for each run of Design 1 testing

Figure (39) is another depiction of the flow characteristics for this design. This figure shows the relationship of Reynold's number to the mass flow rate. As expected, the number 2 element is an outlier and the rest of the elements are much closer together. Element 2 has a much higher perimeter for the area measured due to the

nature of the opening not circular. This higher perimeter led to a lower hydraulic diameter, in turn leading to a higher Re.
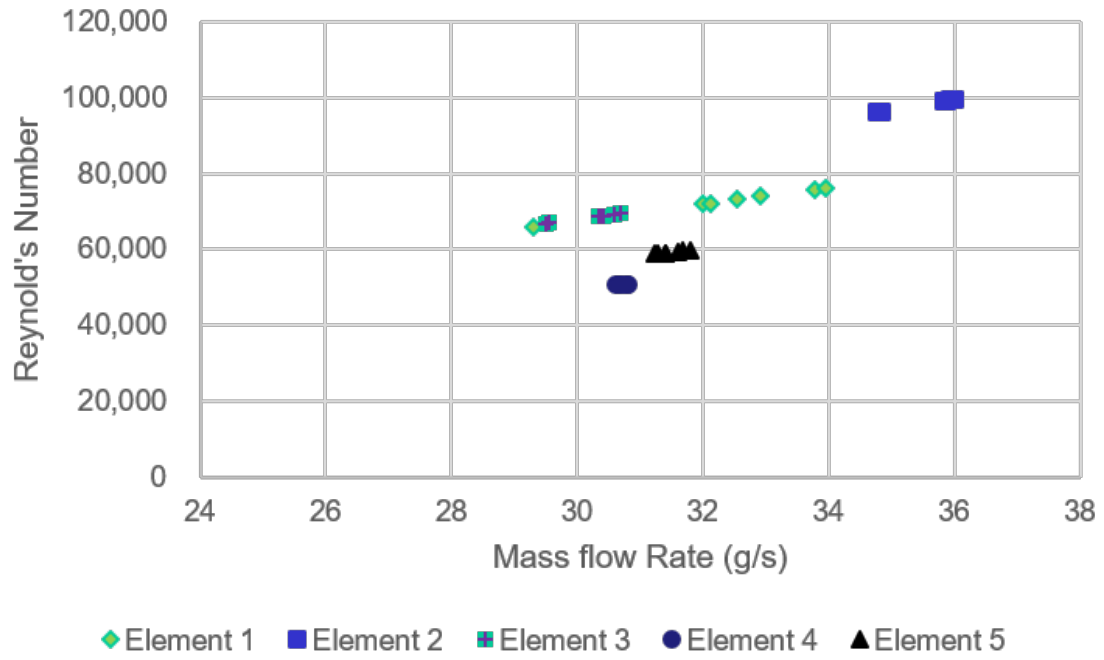
Figure 39. Comparison of Reynolds Number and Mass Flow Rate for Design 1
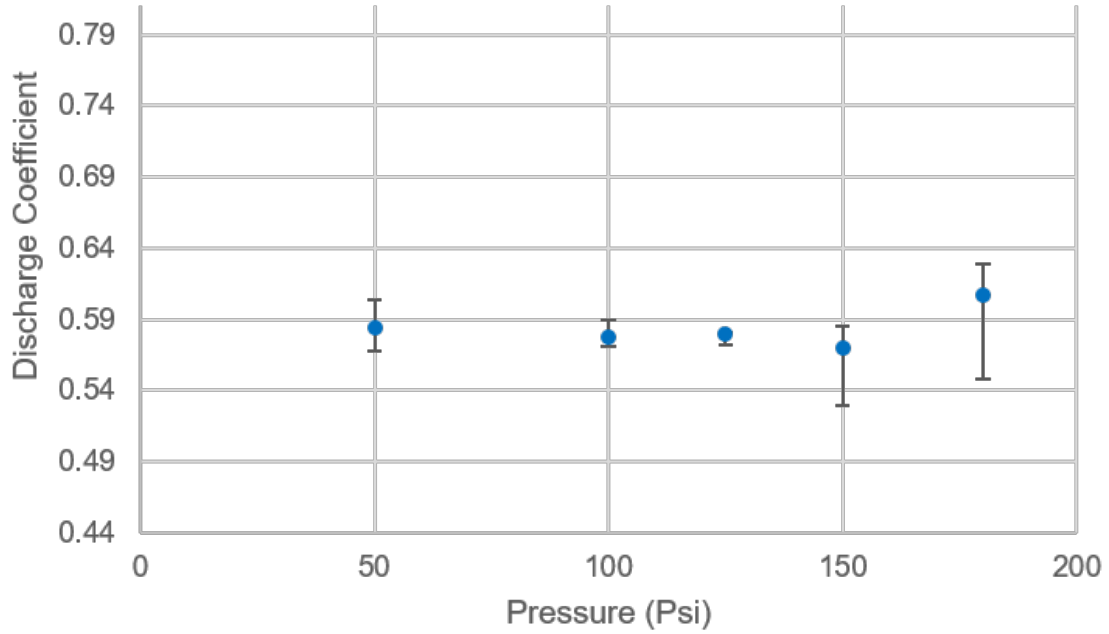
Figure 40. Discharge Coefficient calculated at additional pressure levels

Figures (40 and 41) show results for runs of element 1 at four additional pressures. Figure (40) confirms the Cd is independent of the pressure the system was initialized at. On Figure (40) the data points represent the average of each set of tests while the error bars represent the variation in each set of tests. Figure (41) shows the mass flow rate as a function of the square root of pressure and has a R^2 values of 0.993. The solid line on the plot represents the relationship of these two variables at a constant Cd value found earlier and depicted in Figure (42). The error bars on each marker represent the spread of values found over the set of runs performed at each pressure.
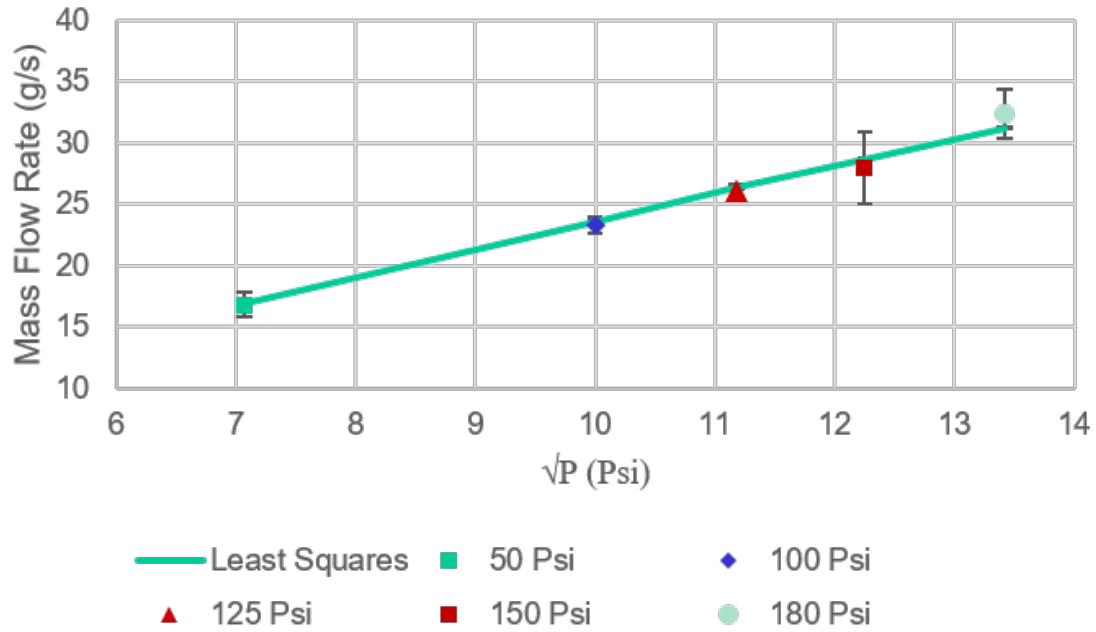
Figure 41. Mass flow rate as a function of the square root of pressure

Figure (42) represents the mass flow rates from all tests of Design 1 (elements 1-5 with 7 runs each) plotted along with the expected mass flow rate based on a singular Cd value. This single Cd value was used to calculate a mass flow rate, these values were then compared to the experimental values. The difference was then minimized by iteratively changing the initial "guess" Cd value. The comparison of the two sets of data shows how far from a normally distributed data set the gathered experimental data was. Figure (42) is a histogram of the distribution of mass flow rates for the data set. The two vertical lines represent one sigma from the mean.

As previously discussed, a normally distributed data set contains 68 % of data within 1 sigma, 95 % of data within 2 sigma, and 99.7 % of data within 3 sigma [15]. Table (14) numerically shows the mean, average, standard deviation, and percentages within 1 and 2 sigma of the average of the mass flow rate.
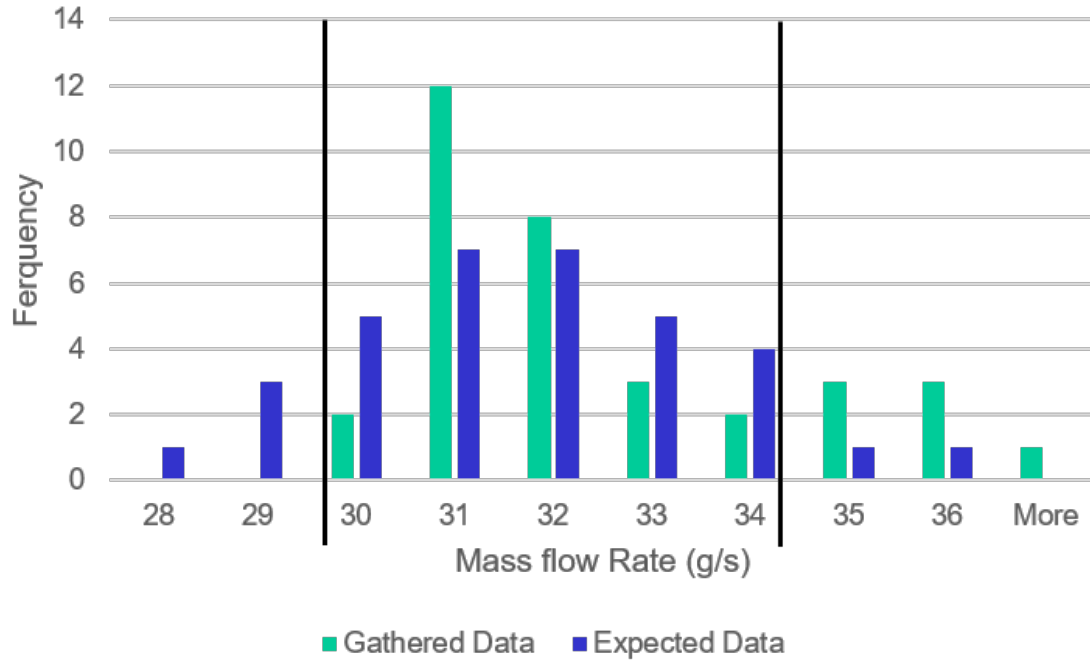
Figure 42. Mass flow rate data compared with expected mass flow values for constant Cd

Table 14. Design 1 statistical data for Mass Flow Rate at varying pressures

Mean	32.05
Standard Deviation	1.98
Count	35
% Within 1 Sigma	71%
% Within 2 Sigma	100%

Design 2.

The geometry of Design 2 presented a unique challenge for analyzing the microscope imagery. The diverging section on the outside of the injector face created many shadows around the opening as shown in the upper left of Figure (43). These shadows made the process of calculating the actual area of the opening more complicated. In

66

order to capture the throat of each element, the image was originally focused on the entire diverging section then slowly moved such that the inner area came into focus until a point was reached where the throat was in focus. The histogram, showing the frequency of dark pixels, had to be analyzed closer to eliminate the maximum amount of shadows without interfering with the actual opening of the element.
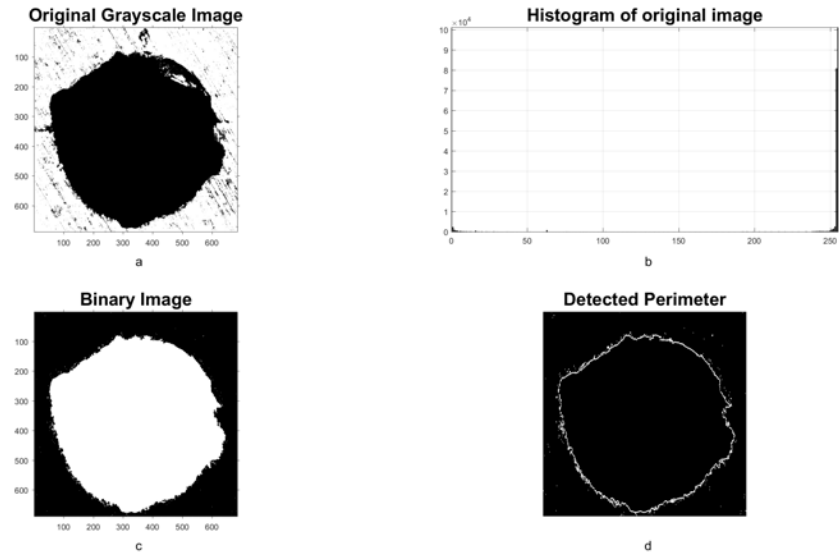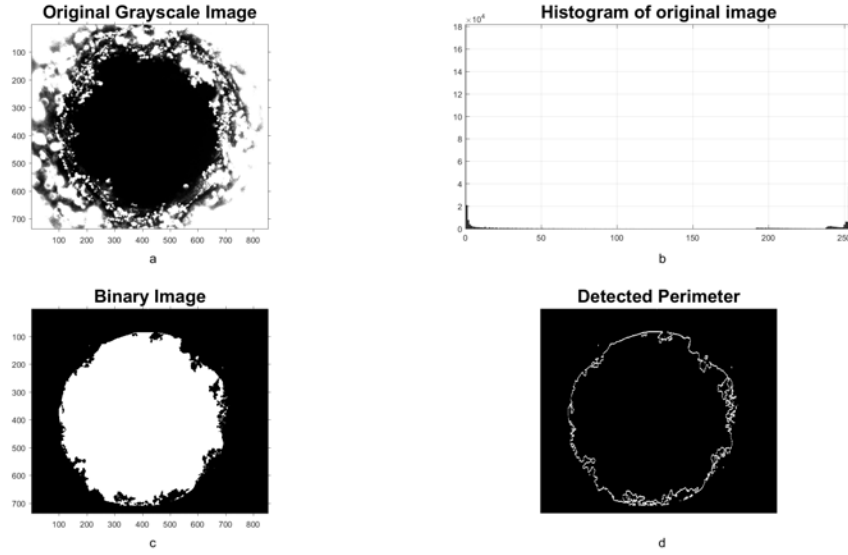

Figure 43. Original image in upper left shows the image captured by the microscope. Binary image in lower left shows the image after converting to pure black and white using threshold obtained from the histogram in upper right. Lower Right shows the detected surface of the opening

As shown in Table (15), the area change from design varies from 18 to 45 %. This is because of this variation in the amount of shadows cast on and around the opening of the elements of this design. The threshold to determining the binary image shown in the bottom left of Figure (43) could not be set lower without eliminating parts of the actual opening.

Table 15. Data from second design using microscope imagery

Number	Area (mm²)	Change from Design (%)	Hydraulic Diameter (mm)	Perimeter (mm)
Design	0.785	-	1	3.14
6	1.139	45	0.452	10.07
7	0.956	22	0.604	6.33
8	0.926	18	0.539	6.88
9	0.970	24	0.491	7.91
10	0.935	19	0.589	6.36
Average	0.988	25	0.535	7.51
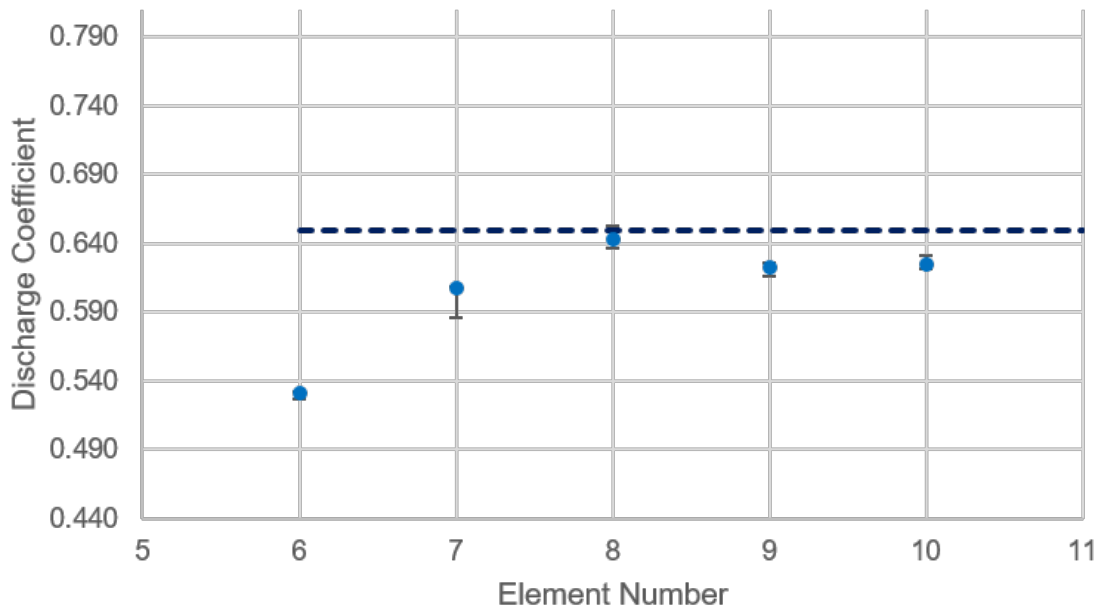
Figure 44. Comparison of Discharge Coefficient for each run of Design 2 testing

Figure (44) shows the calculated discharge coefficient for each test of the elements of Design 2. The dashed line represents the Cd from historical data, and as can be seen is higher than the rest of the calculated coefficients. The Cd of Element 6 is shown

to be lower than the rest of the elements. Looking back at Table (15), it is noted Elements 6 was 45 % above design in terms of area as well as the perimeter being much higher than the rest of the design. This combination of changes from design in the perimeter as well as the area reduce the hydraulic diameter and the effective area reducing the discharge coefficient. This difference, as well as its difference from the rest of the elements in Design 2, would account for the change visualized here in Figure (44). Overall, the results for Design 2 show a tighter grouping with each other as well as being closer to the historical Cd value than those results of Design 1 testing shown previously in Figure (38).

Below, Figure (45) shows how the Reynolds number varied between elements and with mass flow rate. The variation in Re corresponds strongly to the variation in the area calculated for the opening of each element. As shown in the figure, element 6 shows the largest results followed by Element 9 and 8 while Elements 10 and 7 are nearly on top of each other. This staggering of results resembles the results presented in Table (15) where the areas were shown to be widely different.
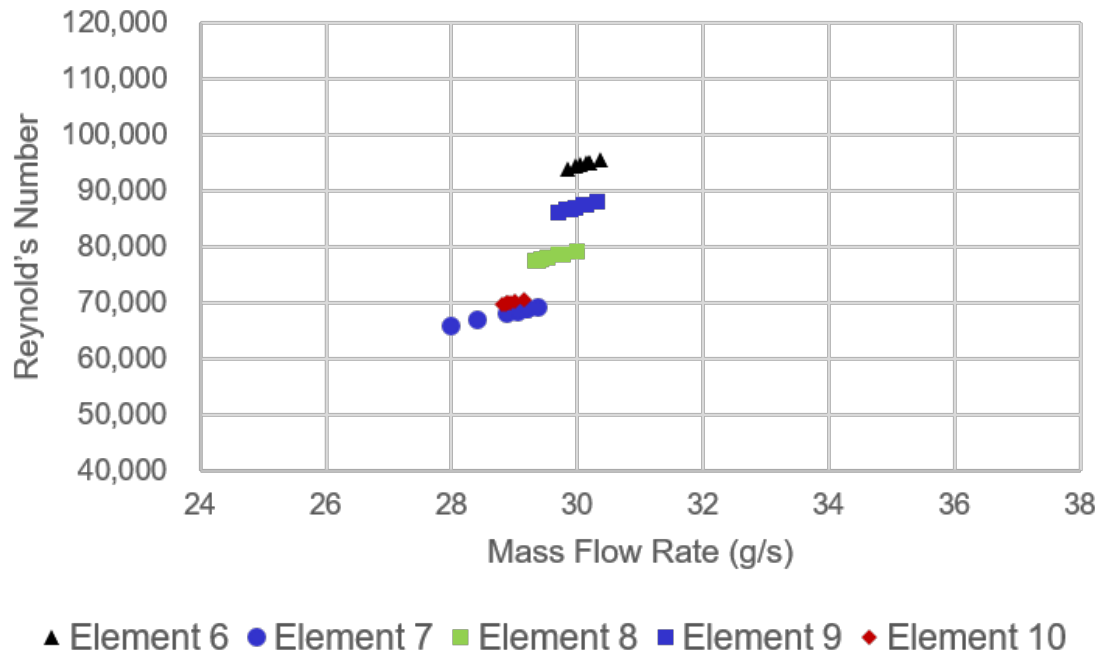
Figure 45. Comparison of Reynolds Number and Mass Flow Rate for Design 2
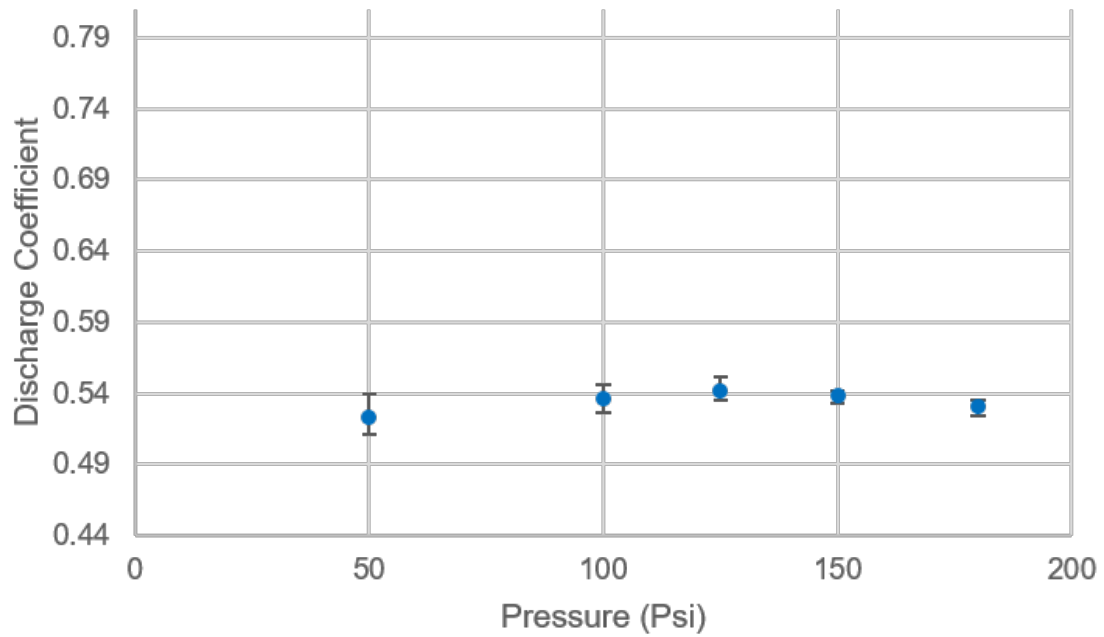
Figure 46. Discharge Coefficient calculated at additional pressure levels

Figure (46) shows the variation of Cd for Element 6 tested at different pressures.

The small amount of variation suggests the independence of Cd with pressure as expected. Figure (47) shows the comparison of the least squares fit to the mass flow rate as a function of the square root of pressure. The least squares fit shows a single Cd value fits the element for a variety of pressures, the error bars represent the variation in tests for each pressure.
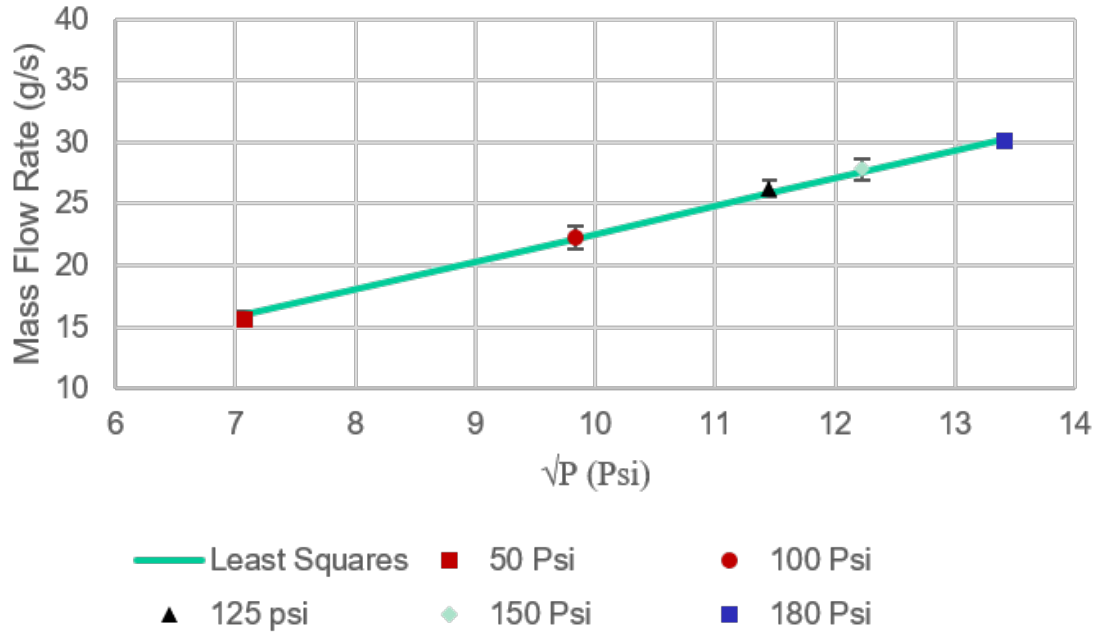
Figure 47. Mass flow rate as a function of the square root of pressure
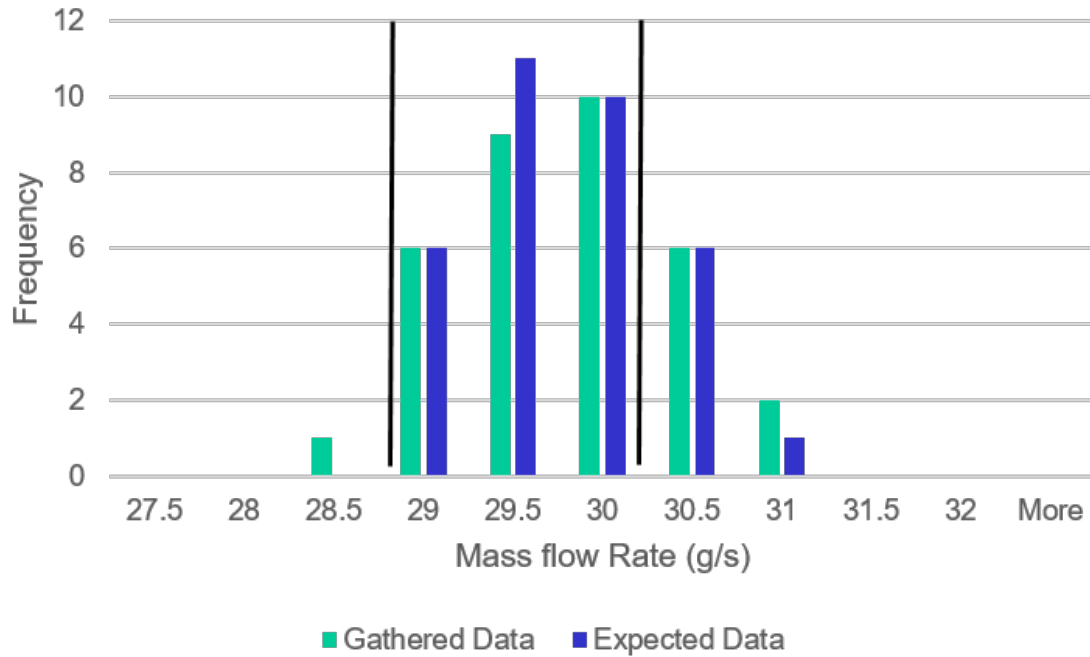
Figure 48. Mass flow rate data compared with expected mass flow values for constant Cd

The data distribution shown in Figure (48) shows the actual data are close to matching the expected mass flow values using a single discharge coefficient. Once again the solid vertical bars here represent 1 sigma from the mean. Table (16) shows 60 % of the data fell within 1 sigma and 97 % fell within 2 sigma. While this data are marginally outside the guidelines for normally distributed at the 1 sigma criteria, the data are will within the criteria at the 2 sigma level.

Table 16. Design 2 Statistical data for Mass Flow Rate at varying pressures

Mean	29.50
Standard Deviation	0.58
Count	35
% Within 1 Sigma	60%
% Within 2 Sigma	97%

Design 3.

The geometry of Designs 3 and 4 lent themselves to being less vulnerable to over sanding than the two previous designs. This robustness, while it would not change the areas of the openings much, would make it harder to keep consistency of mass flow due to the variation in the L/D value if any. This L/D, as previously discussed, is instrumental in the development of the fluid flow. The more time the flow has to develop, the more the velocity profile would change; altering the mass flow as well as the Reynolds number.
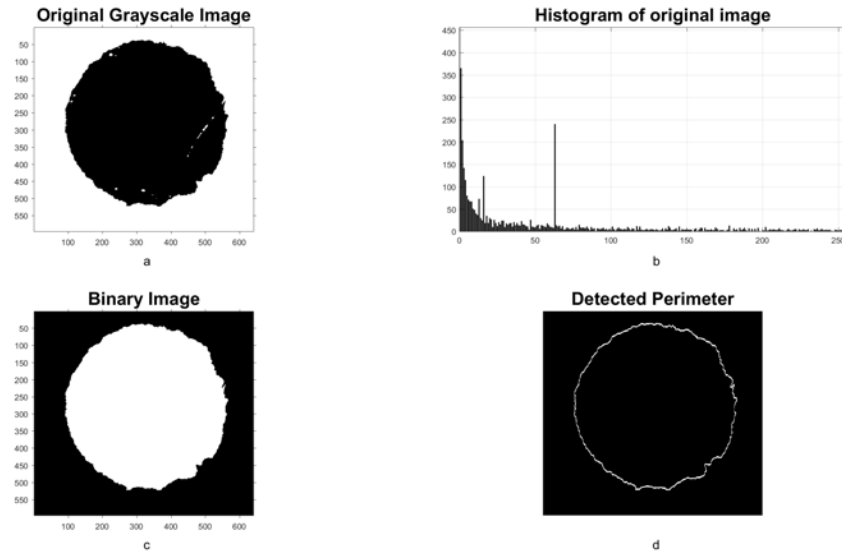
Figure 49. Original image in upper left shows the image captured by the microscope. Binary image in lower left shows the image after converting to pure black and white using threshold obtained from the histogram in upper right. Lower Right shows the detected surface of the opening

Figure (49) shows an image of the picture taken with a microscope at five times magnification as well as a histogram of the pixels, the binary image created, and the detected perimeter of the opening. The original image shows there was little shadowing outside of the opening, allowing for the calculated areas to be very close

to the design area by varying on average of only 7 %. Table (17) shows the results for the rest of the elements of Design 3 and shows the small amount of variation in the calculated area for each element.

Table 17. Data from third design using microscope imagery

Number	Area (mm^2)	Change from Design (%)	Hydraulic Diameter (mm)	Perimeter (mm)
Design	0.785	-	1	3.14
11	0.739	6	0.918	3.22
12	0.845	8	0.756	4.47
13	0.726	8	0.666	4.36
14	0.724	8	0.671	4.31
15	0.743	5	0.738	4.03
Average	0.756	7	0.750	4.08

The variation in the discharge coefficients for the elements of Design 3 is smaller than that of the previous two designs as shown in Figure (50). The variation in the discharge coefficients for this design is primarily due to the vulnerability of L/D to the sanding process causing the variation in mass flow rate. Figure (51) shows this variation in mass flow for each element. As shown in the figure, Element 12 appears to be an outliers with a much higher mass flow than the rest of the designs elements. The increase of mass flow for Element 12 is due to being the only element with an above design area. This lead Element 12 to have the highest discharge coefficient given the relative roughness having a smaller effect with a larger opening area.
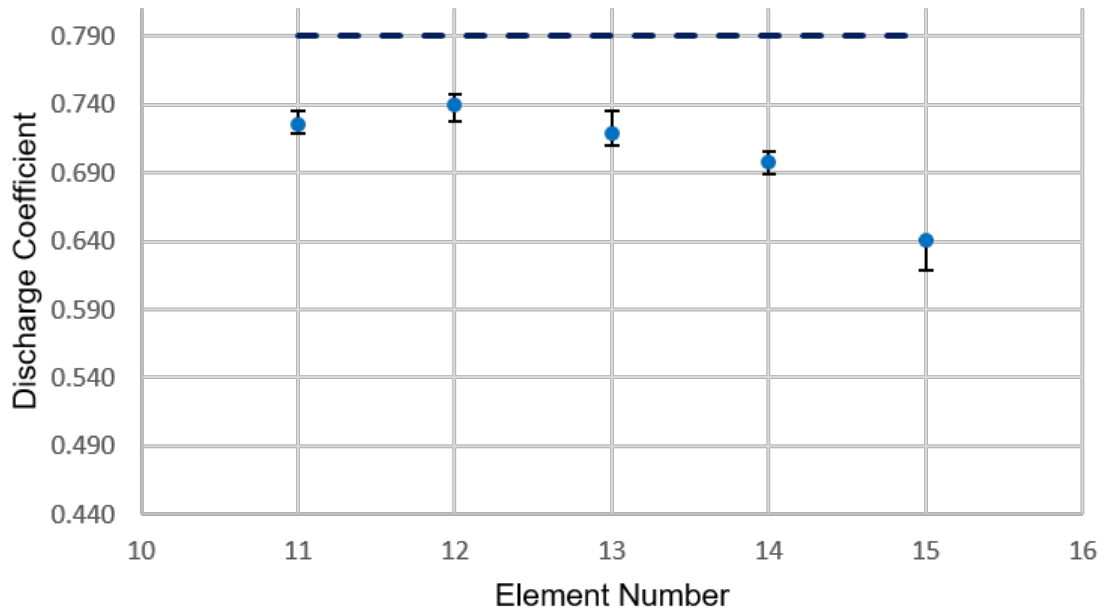
Figure 50. Comparison of Discharge Coefficient for each run of Design 3 testing
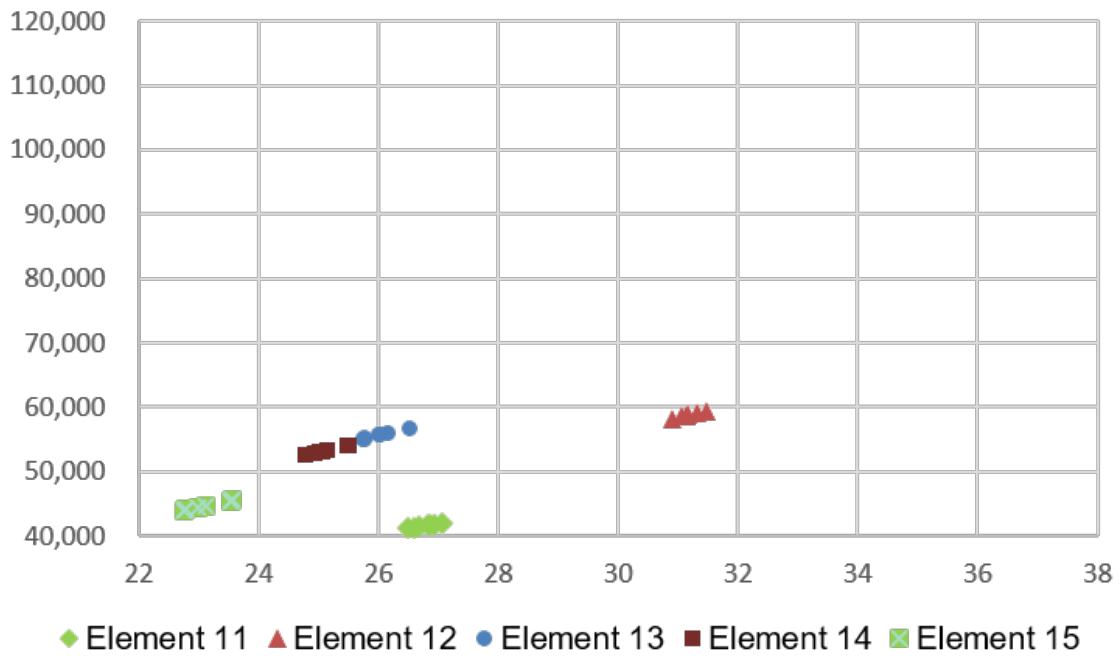
Figure 51. Comparison of Reynolds Number and Mass Flow Rate for Design 3
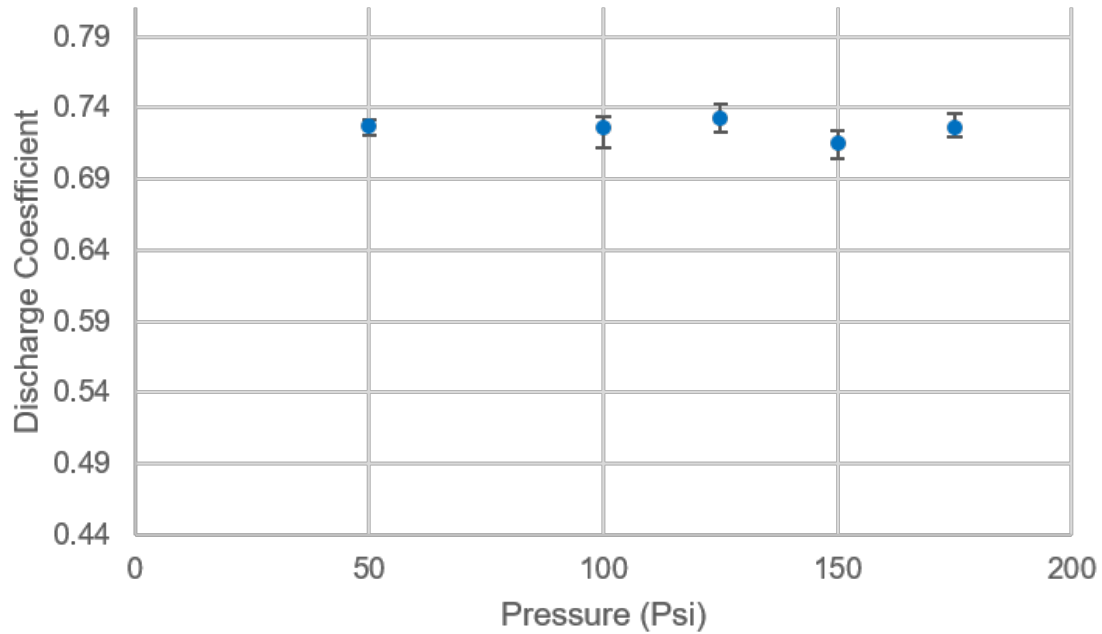
Figure 52. Discharge Coefficient calculated a additional pressure levels

Figure (52) shows the variation of Cd with different pressures for element 11 displaying, as expected, the Cd is independent of pressure for this design. The mass flow rate as a function of square root of pressure is displayed in Figure (53). This figure shows the variation of mass flow for each pressure represented by the error bars on each data point. As previously discussed, the solid line in this plot is representative of a least squares fit to the data gathered for each of the pressures.
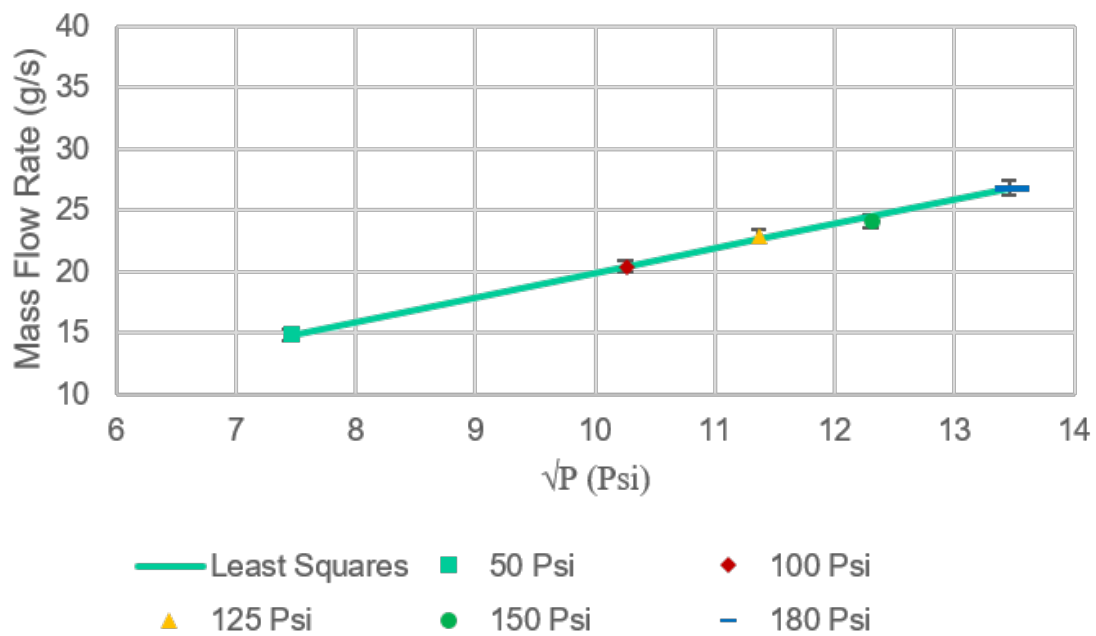
Figure 53. Mass flow rate as a function of the square root of pressure
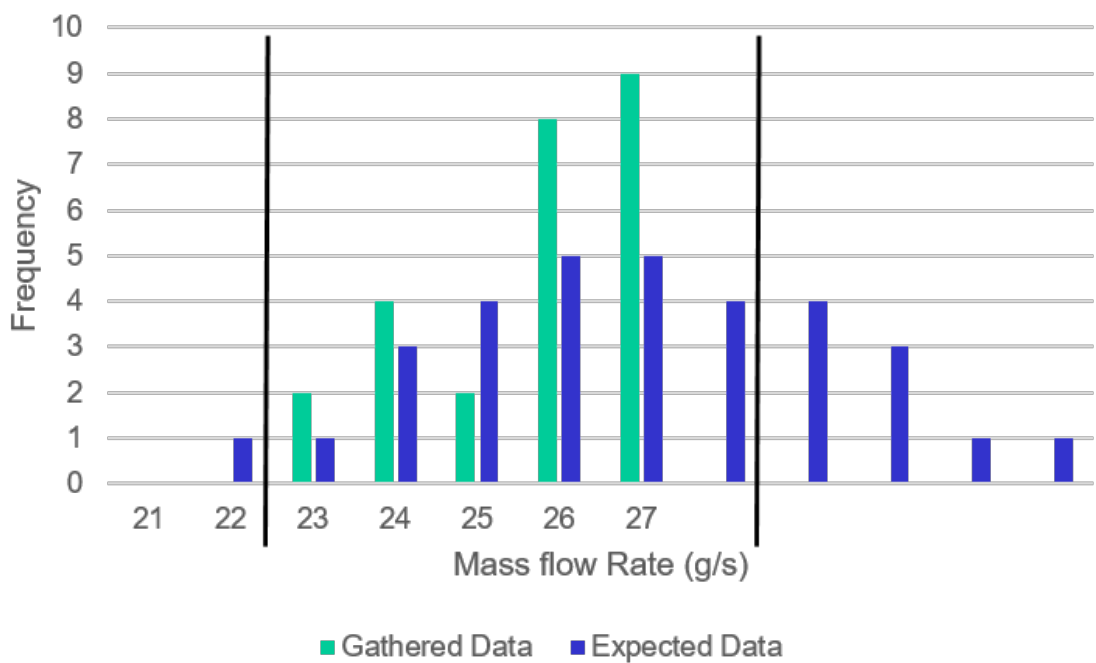
Figure 54. Mass flow rate data compared with expected mass flow values for constant Cd

Figure (54) shows a histogram of the data for Design 3 falls within normal distribution; however, not to the extent as the first two designs. The standard deviation, from Table (18) is slightly above 10 % of the average mass flow rate. While all of the data falls within 2 sigma only 60 % falls within 1 sigma, unlike the desired 68 % of a normal distribution.

Table 18. Design 3 Statistical data for Mass Flow Rate at varying pressures

Mean	26.49
Standard Deviation	2.69
Count	35
% Within 1 Sigma	60%
% Within 2 Sigma	100%

Design 4.

As discussed previously, the geometry of Design 4 had the benefits as well as downsides as Design 3. The geometry allowed the area of each element to be precise and accurate to the design with the largest difference being element 17 at 10 % larger than design. Figure (55) shows the original image taken at 5x magnification, the binary image converted using the histogram (also shown), and the perimeter of the opening. Table (19) shows the differences of each of the elements from the design parameters.
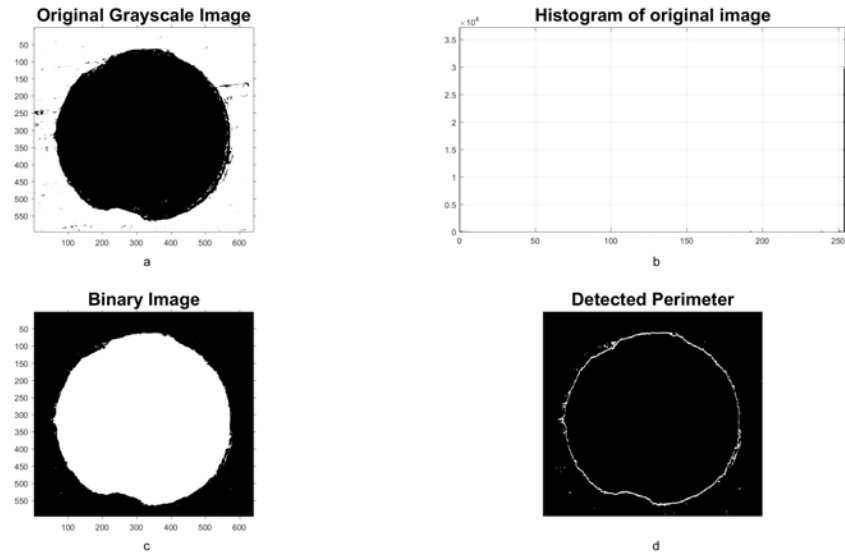
Figure 55. Original image in upper left shows the image captured by the microscope. Binary image in lower left shows the image after converting to pure black and white using threshold obtained from the histogram in upper right. Lower Right shows the detected surface of the opening

Figure (56) shows the variation in Cd for Design 4 was the lowest of all the designs with approximately 0.05 between the minimum and maximum values. The historical Cd is higher than the experimental values, but is consistently higher than the experimental values, this could potentially be accounted for an injector manifold

Table 19. Data from fourth design using microscope imagery

Number	Area (mm^2)	Change from Design (%)	Hydraulic Diameter (mm)
Design	0.785	-	1
16	0.837	7	0.810
17	0.862	10	0.896
18	0.731	7	0.686
19	0.825	5	0.769
20	0.729	7	0.599
Average	0.800	7	0.752

design.
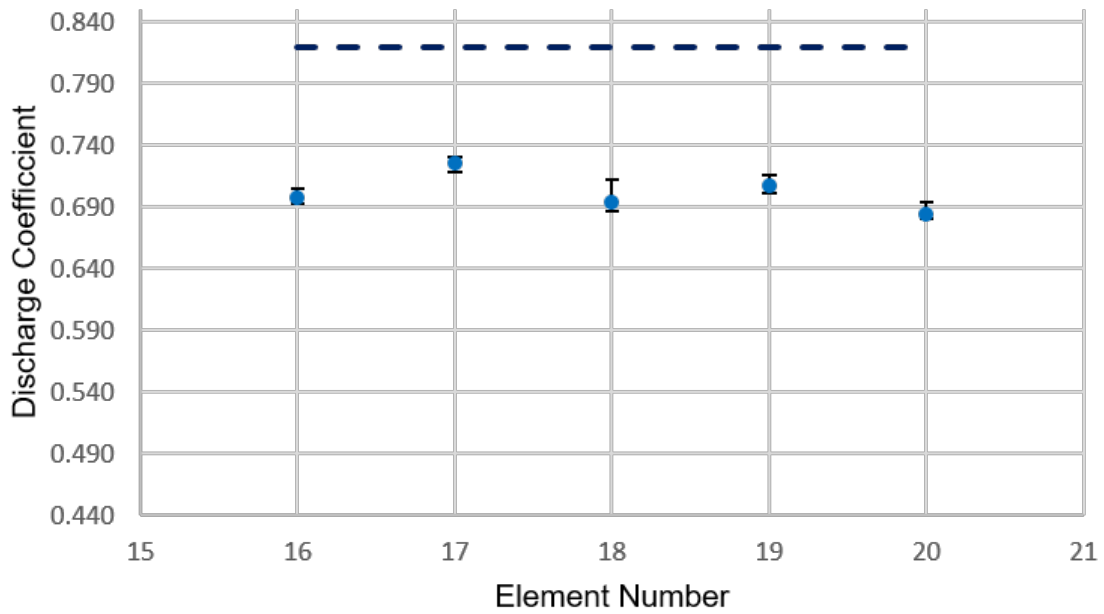
Figure 56. Comparison of Discharge Coefficient for each run of Design 4 testing

The Reynolds number, Figure (57), for each of the elements was between 40 and 60 thousand. With the elements split into two groups one at a higher mass flow while the other had a lower mass flow rate. The mass flow rates correspond to the differences in the area of the openings. The elements with a larger mass flow rate are also the elements with larger than design areas. The elements with lower than design areas correspond to the elements with lower mass flow rates.
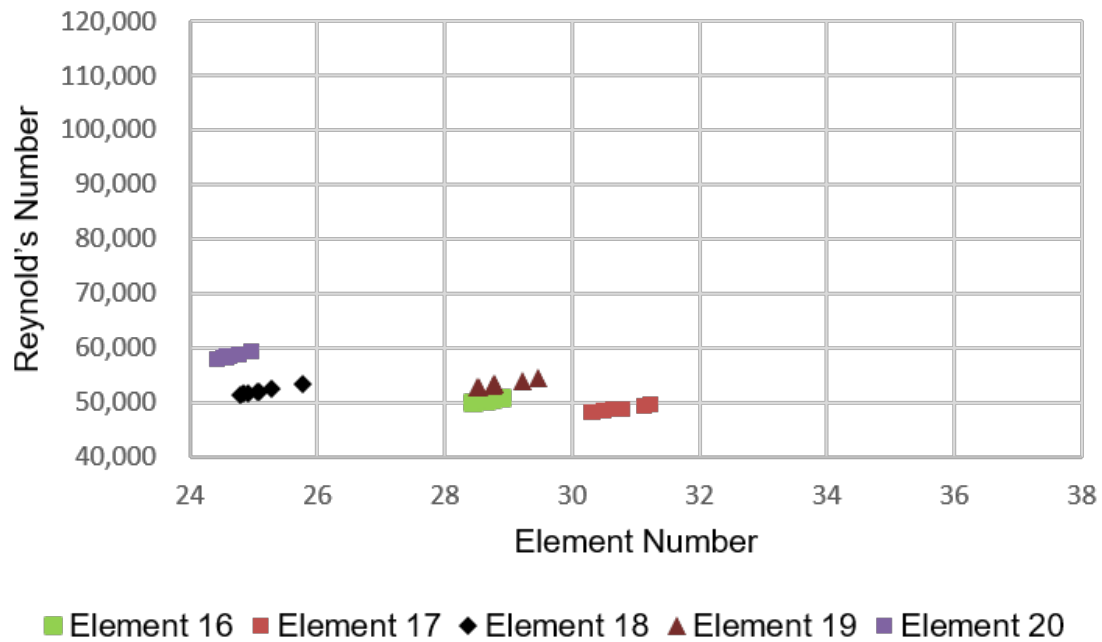
Figure 57. Comparison of Reynolds Number and Mass Flow Rate for Design 4
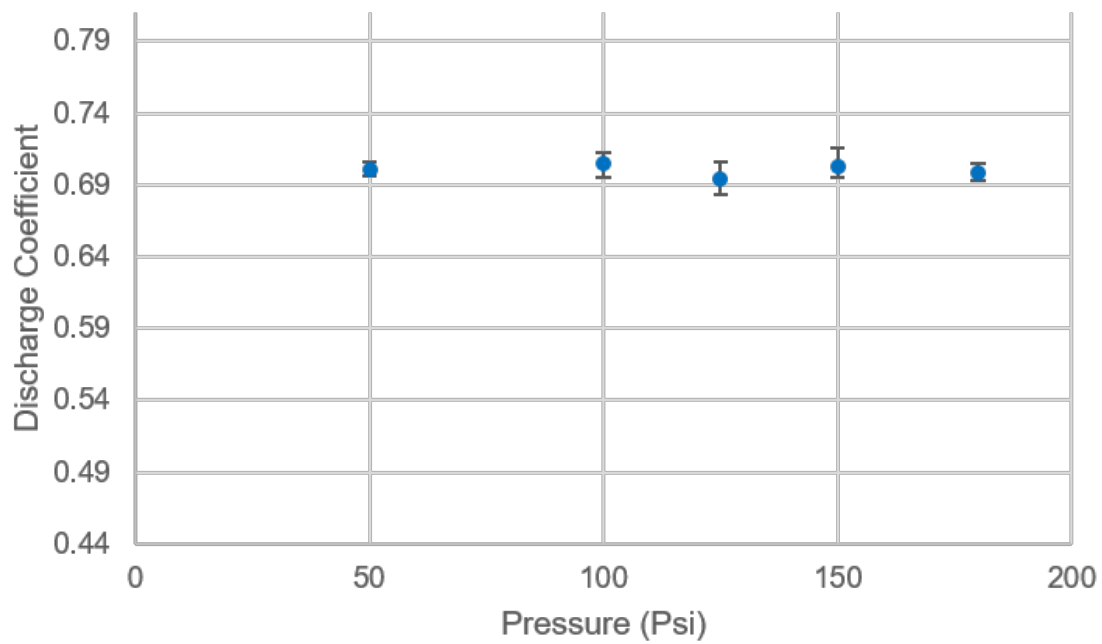
Figure 58. Discharge Coefficient calculated a additional pressure levels

Figures (58 and 59) show the results of testing element 16 at four additional

81

pressures. Figure (58) shows minimal variation of discharge coefficient with pressure. This was expected to be the case but is confirmed here. Figure (59) shows the least squares fit to the mass flow data gathered, as with previous plots the error bars here, represent the spread of data for each pressure. The largest variation in data points is shown to be with the 150 PSI tests followed by the 100 PSI tests.
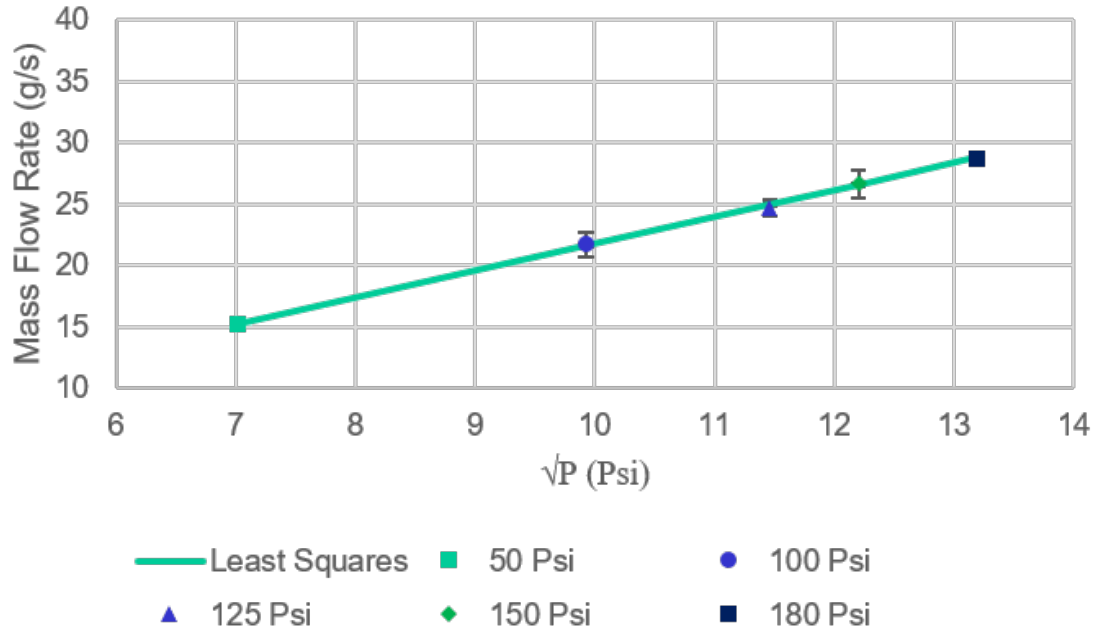

Figure 59. Mass flow rate as a function of the square root of pressure
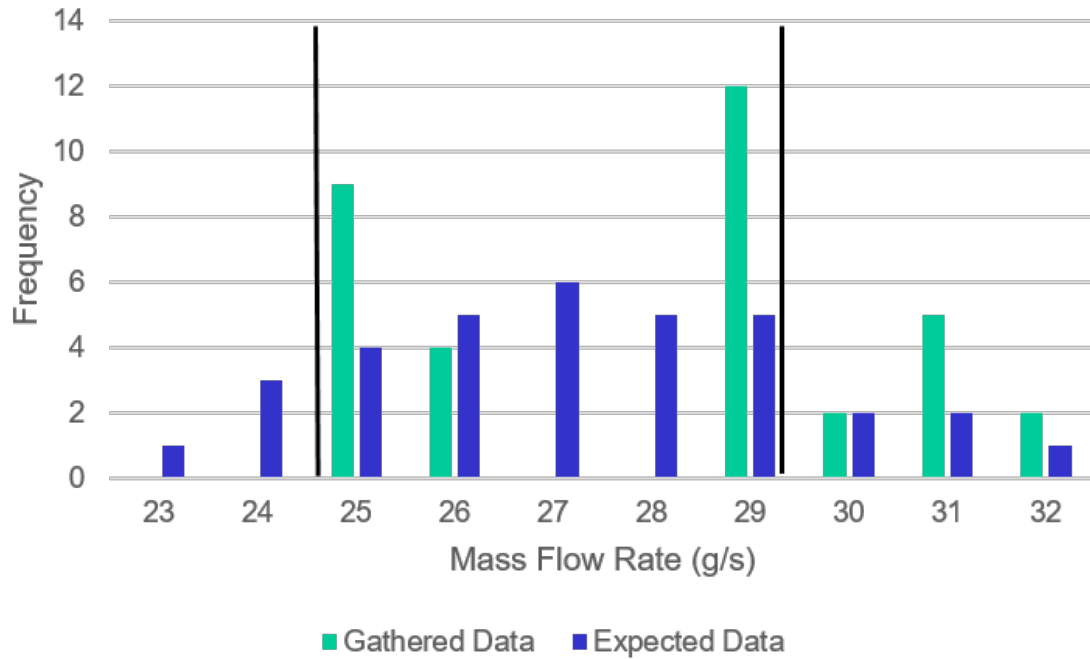
**Figure 60. Mass flow rate data compared with expected mass flow values for constant Cd**

The histogram of data shown in Figure (60) suggests a large amount of variation.The spread of sigma values shown in Table (20) shows only 46 % of the data were below 1 sigma with all of the data below 2 sigma. While the histogram shows no values on the mean for the gathered data. The table shows the standard deviation just under 10 % of the mean of the 35 samples.

Table 20. Design 4 Statistical data for Mass Flow Rate at varying pressures

Mean	27.59
Standard Deviation	2.35
Count	35
% Within 1 Sigma	46%
% Within 2 Sigma	100%

4.3 High Speed Imagery

These frames were captured well after the flow was started to ensure steady-state flow. Using a post processing software known as ImageJ, the images were analyzed. This software was used to find the maximum of each pixel in every frame and compiled into a single image. These maximum images are shown below in Figure (61). The figure shows the differences in each of the element designs while matching pressure for each design. These differences are due to both design as well as the imperfections of additively manufacturing.

Design 1 is shown in the upper left of Figure (61). It shows the design having a strong core flow as expected and shown previously in Figure (20). Interestingly, Design 1 is shown to not have a symmetric spray area, this is due to the build capabilities of the additive manufacturing process and the anomalies created at the orifice.

Design 2 is shown in the upper right image of Figure (61). The flow shown was very expected from the CFD results. The center core flow is shown as well as a close to symmetric spread in the spray area.

Design 3 shown in the lower left of Figure (61). The image shows little spread in the spray area with a very strong center core jet. This behavior was hinted at in the CFD results shown in Figure (25); however, the CFD results showed more spreading of the spray area than is shown here. This difference in the spreading rate is most likely due to the imperfections of the manufacturing process and the fact that the CFD modeled a perfectly manufactured design.

Design 4 is shown in the lower left image of Figure (61). The image shows a similar spreading rate to that shown for Design 1. The image also shows increased symmetry when compared to Design 1. The spray patterns of the designs can be used to estimate the type of injector system they would be best suited for. For instance,

Designs 2 and 3 appear to be better for an impinging setup where the interaction of multiple streams would cause mixing and atomization. This is due to the a low spreading angle and strong core flow.
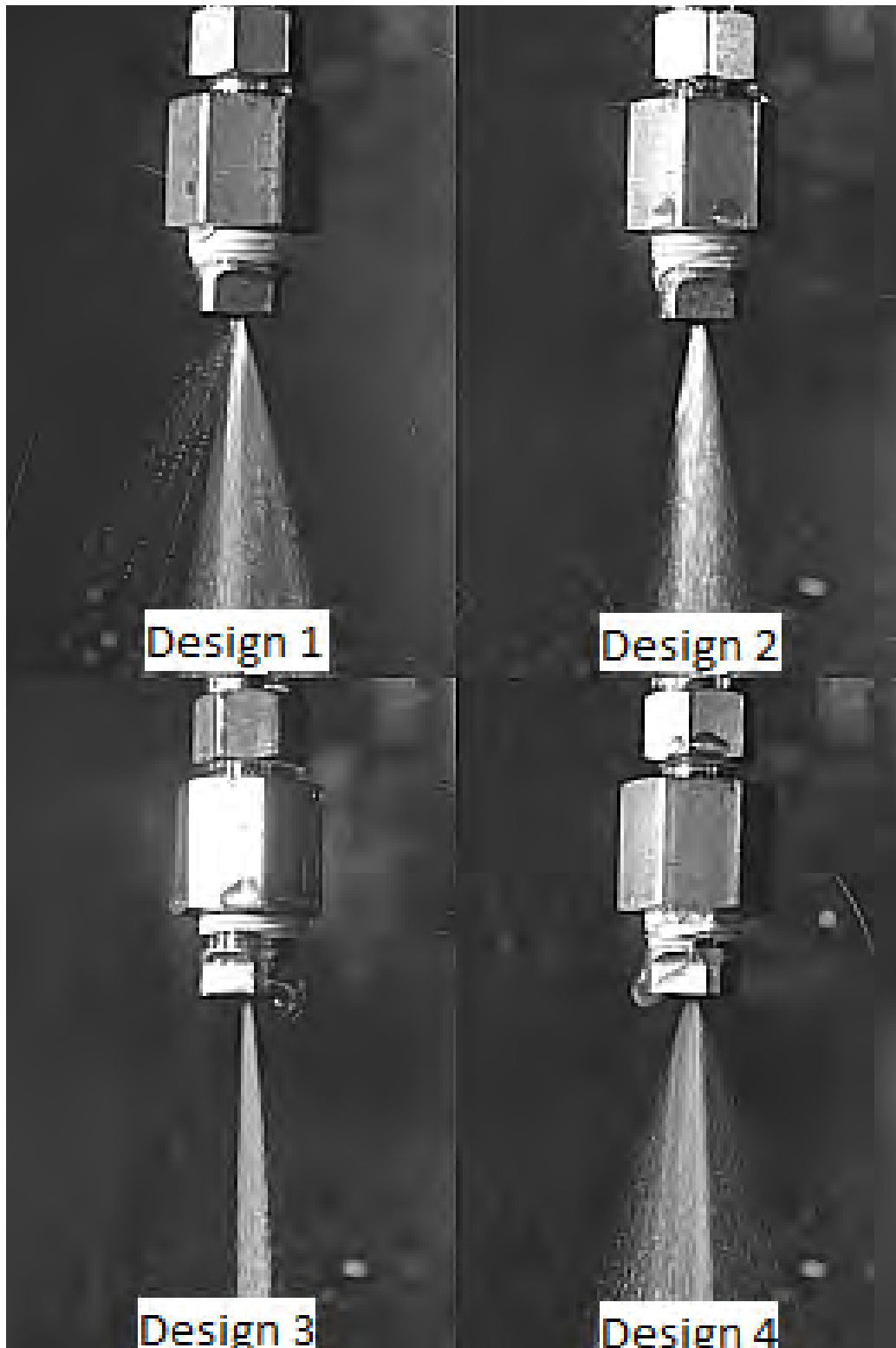
Figure 61. Comparison of spray for each design

4.4 Surface Roughness Measurements

Designs 2 and 4 were chosen to be sliced in half and examined due to their respective geometries. The build direction was instrumental in the decision to chose these designs as well. As was previously discussed, each element was built from the opening section first then to the start or threaded area of the element. Meaning for Design 2 the diverging section after the throat was built as an overhanging section while the converging section of Design 4 was built with each layer being the base for the next. Figure (62) shows an image of the converging ramp of Design 4 (a) compared to the diverging section of Design 2 (b). The difference in surface roughness is shown in the quality of the respective surfaces. In Image (a) it can be seen the surface is not smooth and is interrupted by the presence of what appear to be extra pieces of metallic powder. These extra grains of powder were erroneously sintered into their places during the manufacturing process. Image (b) shows the diverging section of Design 2. This image reveals the surface is not as uniform and scattered with relatively deep valleys and high protrusions. The combination of these valleys and protrusions lead to an average roughness similar to Design 4. This variation in uniformity shows the physical relationship of the roughness constant in the CFD simulations previously discussed.
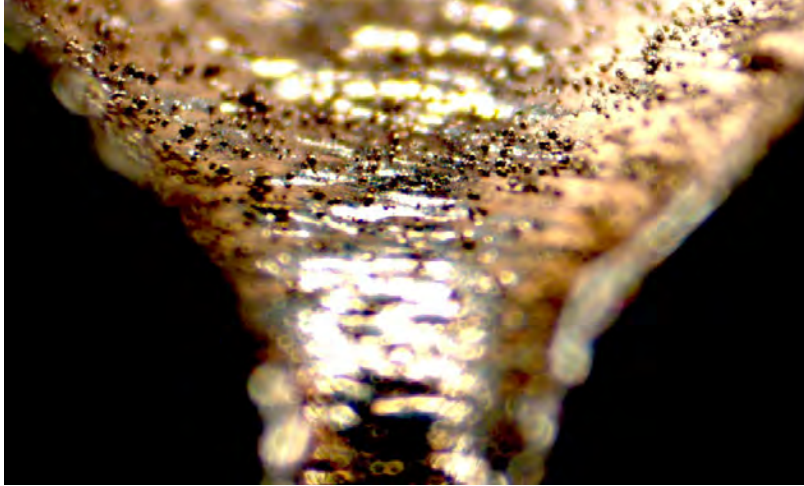
(a)
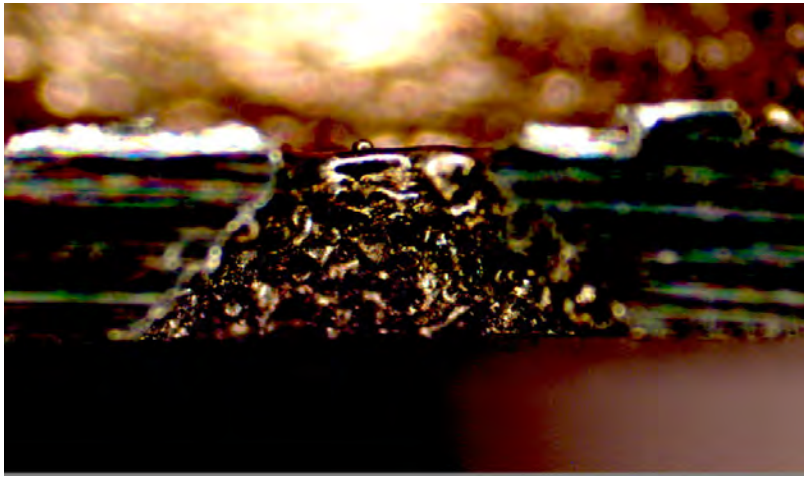
(b)

Figure 62. Converging section of Design 4 (a) Diverging section of Design 2 (b)

Figure (63) shows multiple images of the diverging section in Design 2. Image (a) shows a 12x magnification optical image, it shows the level of change in the surface roughness from looking from the diverging conical section to the interior walls of the element. Image (b) shows a 26x magnification optical image of the same section and focuses on showing the variation of printed area on the diverging section. It is important to note this was the section build as an overhang due to orientation

during manufacture. Image (a) of Figure (64) is an optical image of the element before being sliced in half. This image shows the build levels of the section and highlights the mountain and valley nature of this area. The final image ,(b), shows the topographical map of the surface gained through the use of a Laser Scanning Microscope (LSM). The surface roughness of this area was found to be 71.75 μm. The image shows the existence of anomalies, in particular, that are on the order of half the overall sample height shown.

(a)
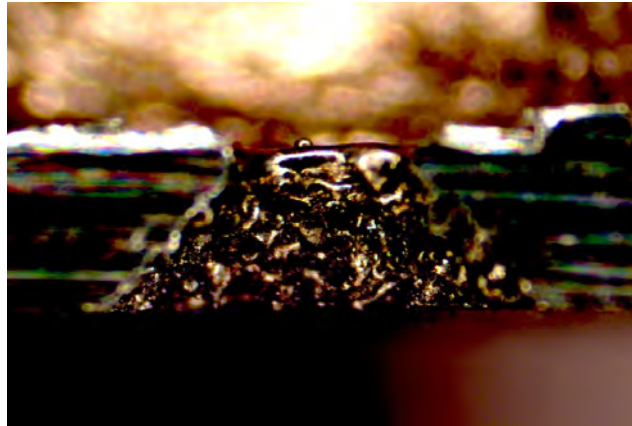
(b)

Figure 63. Optical image of Design 2 (a) Optical image of Design 2 magnified (b)
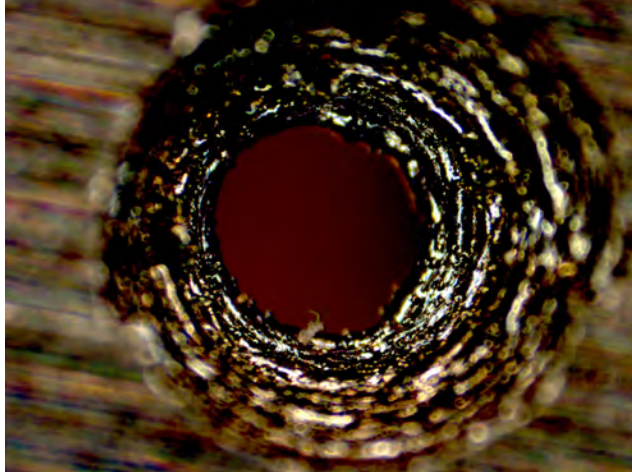
(a)
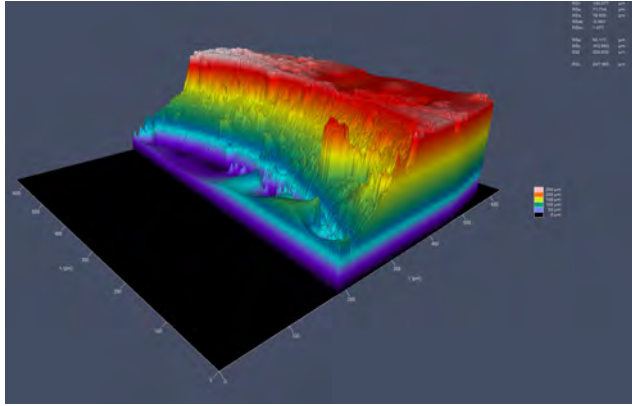
(b)

Figure 64. 45x optical image of non cut Design 2 element (a) LSM topographical image of Design 2 diverging section(d)

Below, Figure (65) shows the same optical image of the converging section of Design 4 as presented in Figure (62 (a)) now compared to a LSM image of the section boxed off. The LSM was used to image a 600 μm x 600 μm section of the converging ramp. This LSM image shows a topographical map of the surface. The average surface roughness found with the LSM was 50.994 μm. This is much lower than the upper limit simulated with the CFD and is on the order of the size of the particles in the powder used.
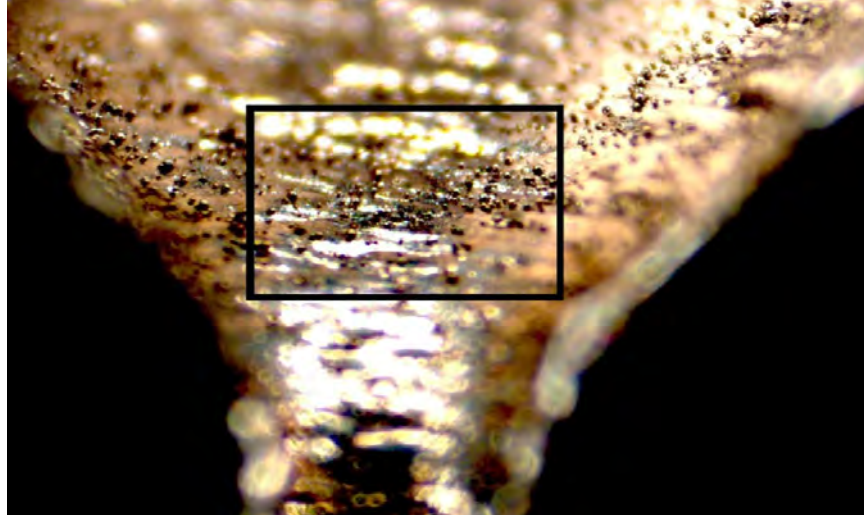
(a)
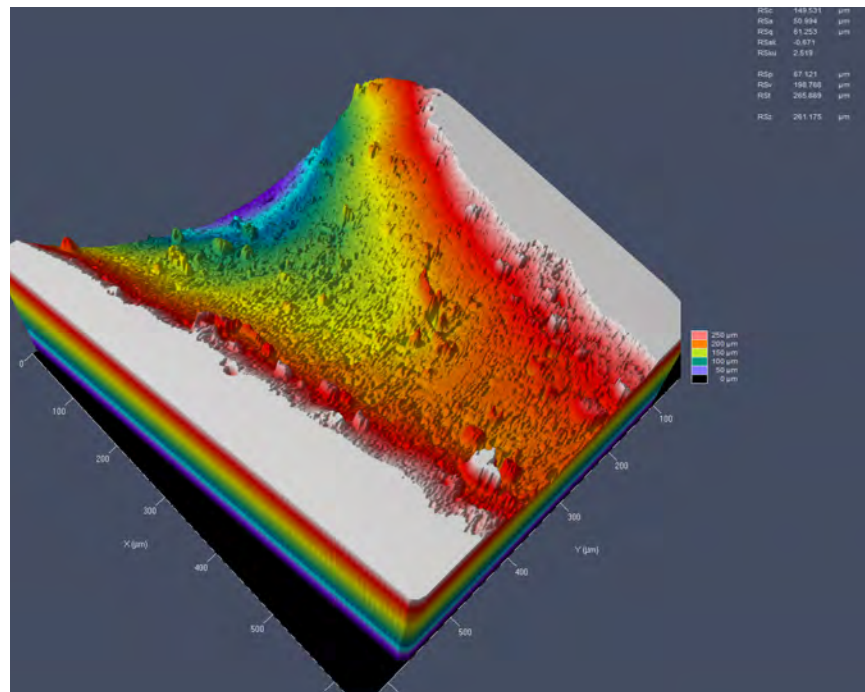
(b)

Figure 65. (a) Optical image of the converging section on Design 4 at 38x magnification (b) LSM image of boxed section on image (a)

V Conclusion

This chapter concludes this work and evaluates the accomplishment of the research objectives outlined in Chapter 1. An analytic model was used to predict the effects of surface roughness on the discharge coefficient of injector elements. This was done by incorporating turbulent viscous flow into a computational model of flow through four different geometries of an injector element.

5.1 Summary of Research Objectives

It is necessary to re-state the research objectives laid out in Chapter I. The objectives are listed below.

1. Measure mass flow rate of additively manufactured injector elements with a controlled pressure drop.

2. Calculate discharge coefficient of injector designs using computational and experimental techniques

3. Compare discharge coefficient of both techniques to each other as well as historical data.

4. Visualize flow of AM injector elements.

The first objective was met in that the mass flow rate was calculated for each of the additively manufactured elements. The second objective was met through the implementation of the Fluent 17.2 CFD package and a developed experimental method. The third objective was met through the data analysis and comparisons of discharge coefficients of respective designs with historical data available. The final research objective was met through the use of high speed imagery.

5.2 Summary of Results

The compilation of computational and experimental results leads to the following conclusions. First, the computational model provided great insight to the dependence of the flow characteristics on surface roughness and geometry of the design. Second, the imagery indicated the designs where the geometry allowed for over sanding to not be an issue, the printing process allowed for a very precise and accurate to design area value.

Experimental results showed the discharge coefficient for each design was lower than the textbook value as well as the CFD value. This is most likely due to the lack of exact modeling of turbulence in CFD and unknown exact roughness uniformity at the time of the CFD simulations. Each design, while being lower than the text and CFD, was consistently less than the CFD and text values for each of the elements for their respective designs. This consistent loss of performance, if acceptable, could be designed around for implementation in an engine. The experimental results also showed large amounts of variation in the measured areas as well as the perimeters of each orifice. This variation is due to the methods used to obtain the measurements and the use of detailed microscope imagery. Future work would be needed to resolve some of the variation issues seen in this research pertaining to these measurments.

5.3 Future Work

The results of this research indicate many avenues for future research interests. First would be to design build and test full arrays of injector elements. This research was only able to test single elements and not explore the flow stream interactions of having multiple elements in a manifold. Doing this would give a more realistic perspective of the affect the increased roughness would have on performance outside of simply mass flow rate comparisons.

Second, would be to explore novel designs that cannot be traditionally manufactured due to complexity of design or shape. Testing of new designs would allow for experimentation and possible discovery of more efficient mixing capabilities. New designs could potentially be placed differently and arranged within the manifold to allow better use of space or thermal control. Given the nearly limitless designs available with additive manufacturing, this area of future research could be endless. With new designs, a different approach for measuring the true area of the orifice opening would need to be used to avoid potential issues shown when measuring the area of Design 2.

Finally, an improved method for calculating the effective area and hydraulic diameter of each orifice would need to be explored. The methods used in this research, while highly detailed in their calculation of the area and perimeter, may have been over accurate and not truly representative of what the flow particles would interact with. By computing the effective diameter and area of each orifice a more accurate representation of the flow area could be calculated. Therefore, a more accurate calculation of the discharge coefficient could potentially be calculated.

5.4   Final Conclusions

The implementation of additive manufacturing has the potential to drastically reduce the amount of waste, time, and cost of making parts. Programs could move to a more flexible process and somewhat optimize designs before final components were built. The rocketry industry is already adopting additive manufacturing. The advantages of additively manufacturing components, along predictable losses shown in this research present DLS as a viable method of manufacturing for rocket engine components as small aa injector elements.

VI Appendix 1

The following images are CAD drawings of the injector element designs as well as stress simulations for 200 PSI. This pressure was chosen to guarantee there would not be a component failure with any of the elements as well as identify any weak spots in the designs.
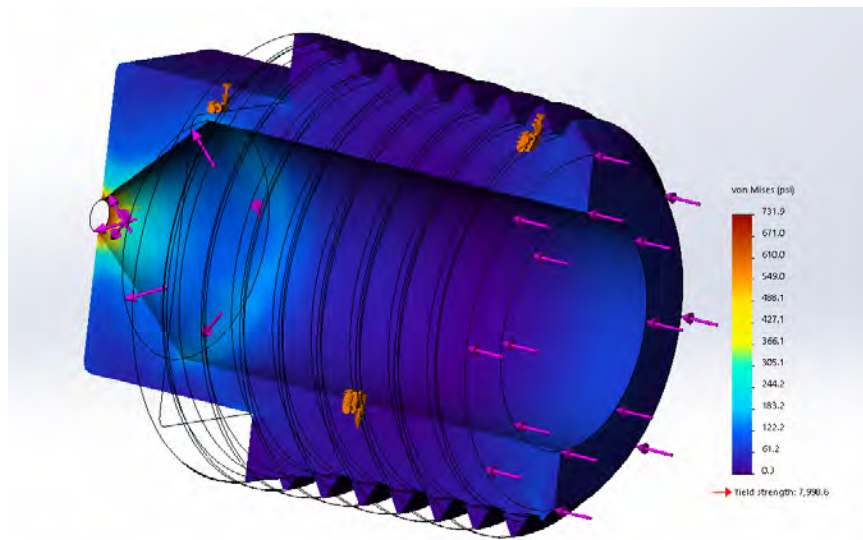
Figure 66. CAD of Sharp-edged Cone element stress analysis [23]
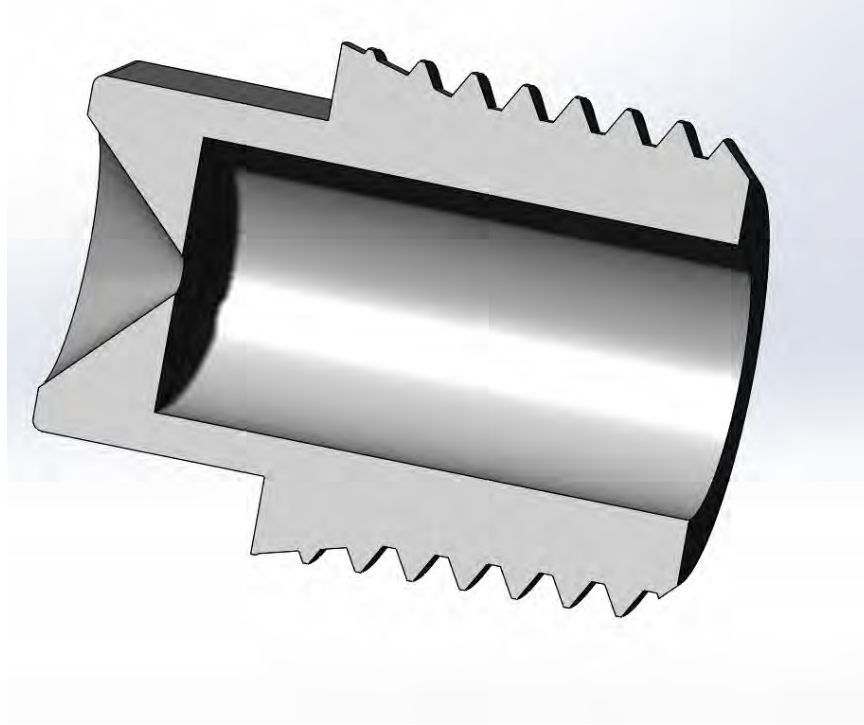
Figure 67. CAD of Sharp-edged orifice element [23]
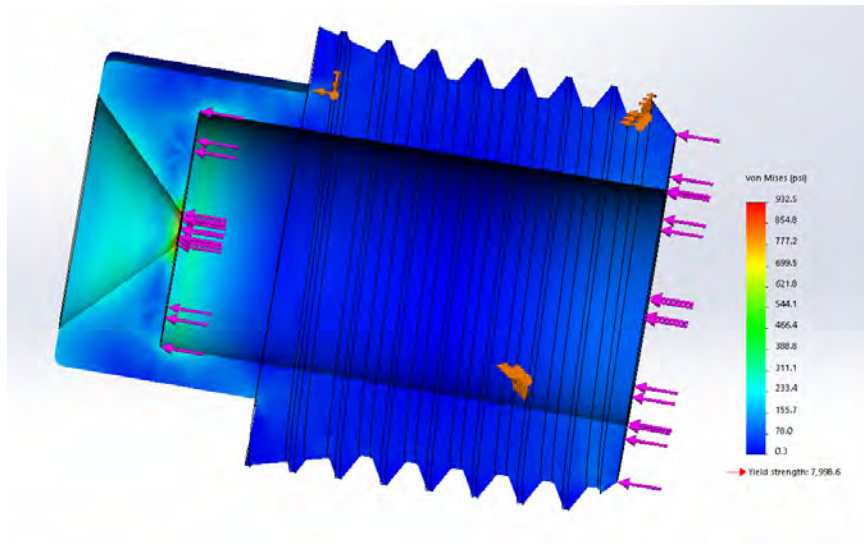
Figure 68. CAD of Sharp-edged orifice element stress analysis[23]
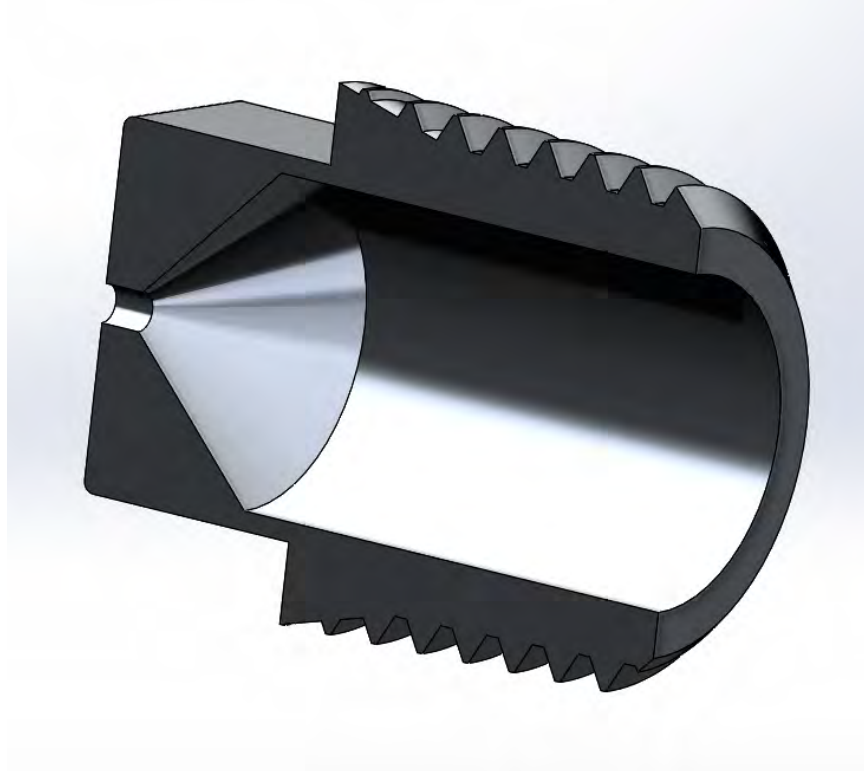
Figure 69. CAD of Short-tube with conical entrance element [23]
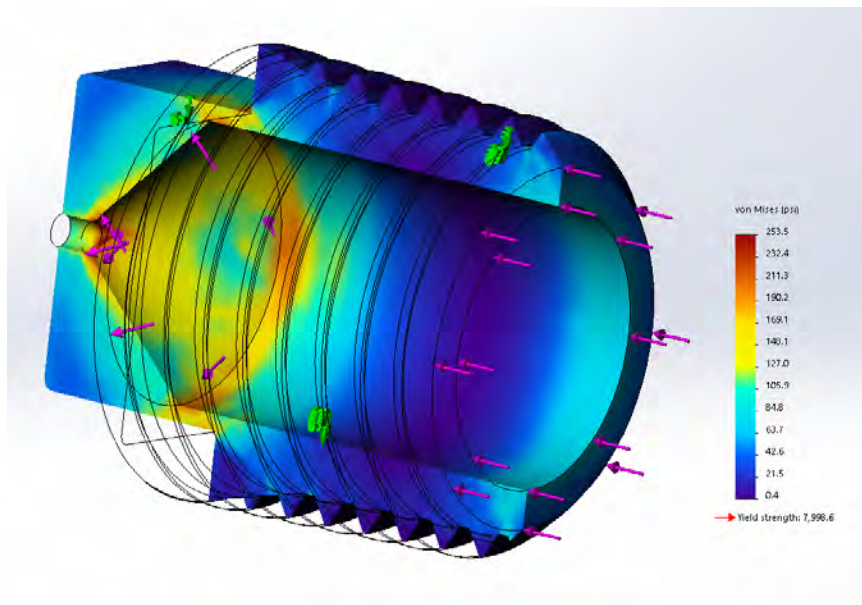
Figure 70. CAD of Short-tube with conical entrance element stress analysis [23]
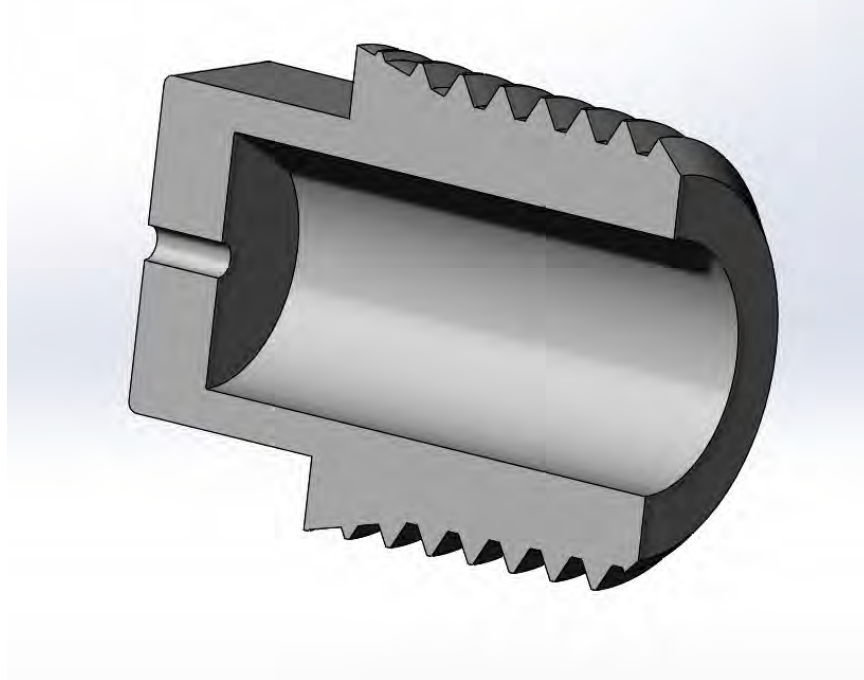
Figure 71. CAD of Short-tube with rounded entrance element [23]
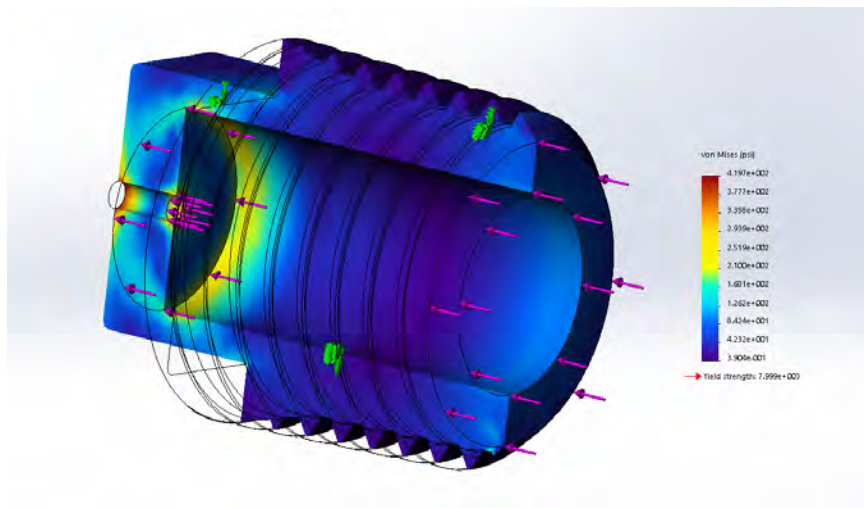
Figure 72. CAD of Short-tube with rounded entrance element stress analysis [23]
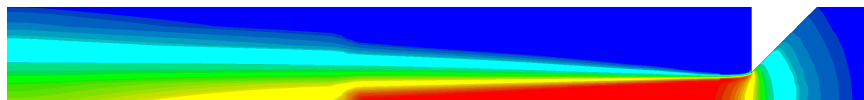
Figure 73. Velocity Contour of Design 1
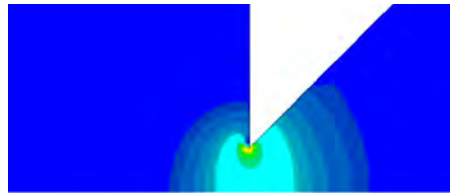
(a)
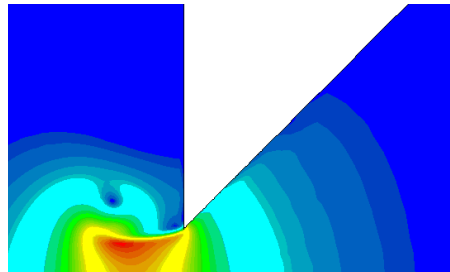
(b)
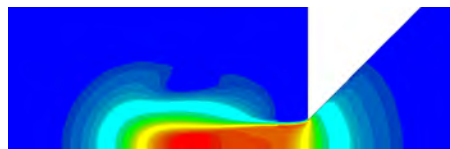
(c)
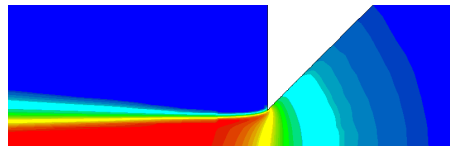
(d)

Figure 74. Design 1 flow progression in time: (a) Time 9.6E-6 sec (b) Time 6.6E-5 sec (c) Time 1.8E-4 sec (d) Time 2.4E-3 sec all flow is from right to left

VII Appendix 2

Design 1.
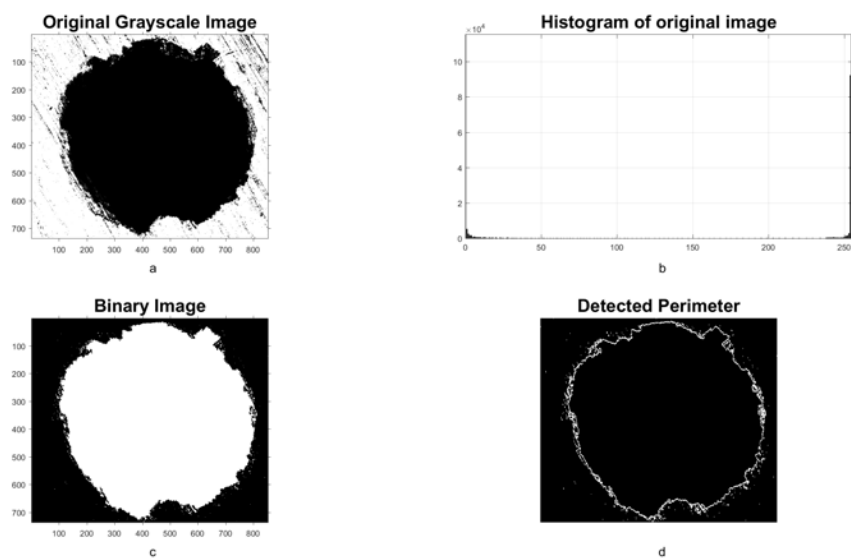
Figure 75. Original, Histogram, Binary, and Perimeter images for Element 2
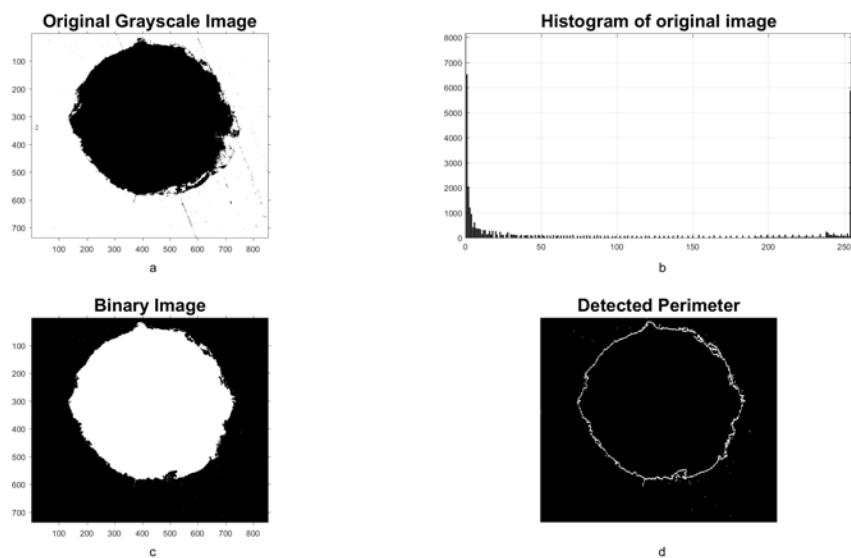
Figure 76. Original, Histogram, Binary, and Perimeter images for Element 3
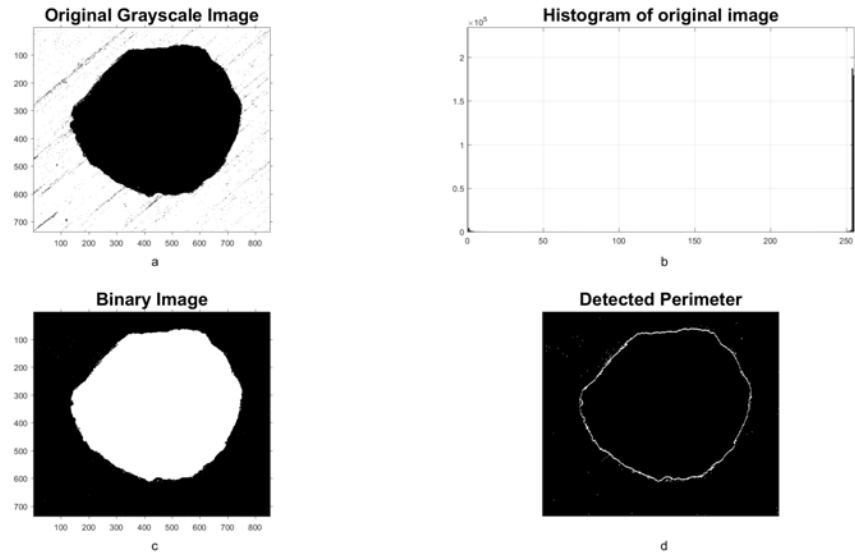
Figure 77. Original, Histogram, Binary, and Perimeter images for Element 4
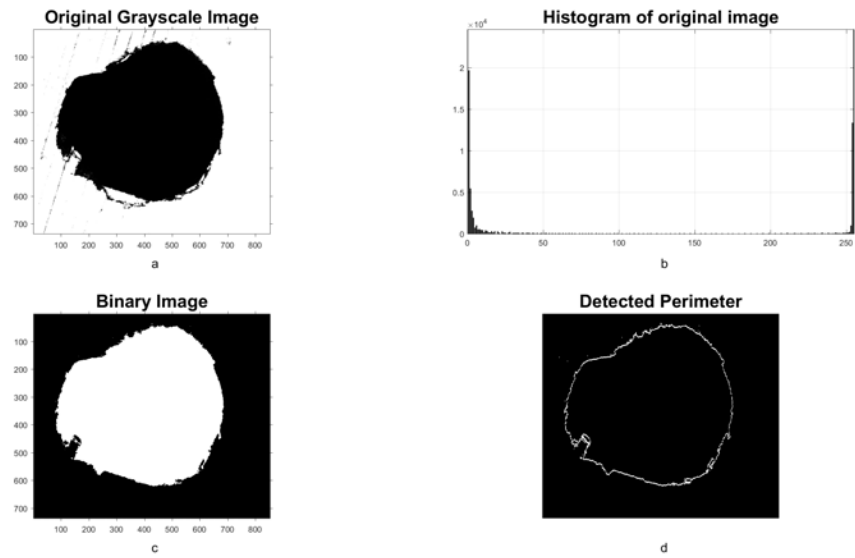
Figure 78. Original, Histogram, Binary, and Perimeter images for Element 5

Design 2.
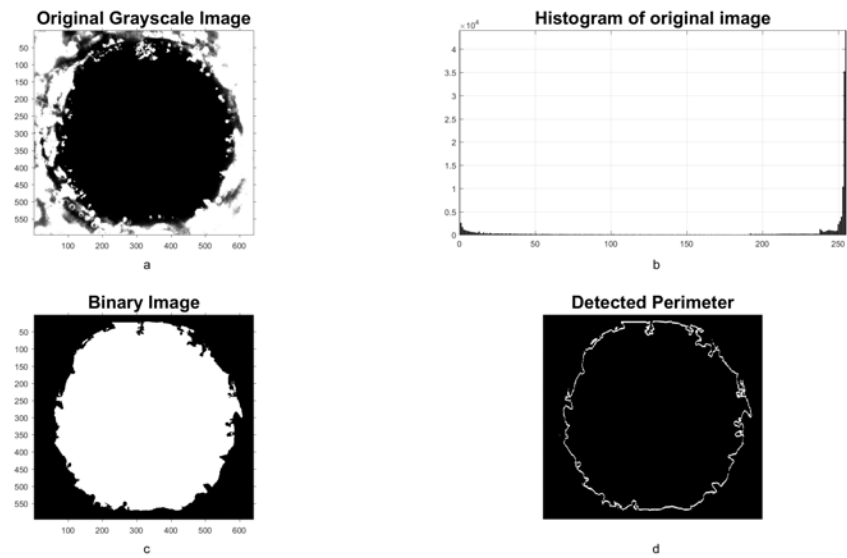
Figure 79. Original, Histogram, Binary, and Perimeter images for Element 7
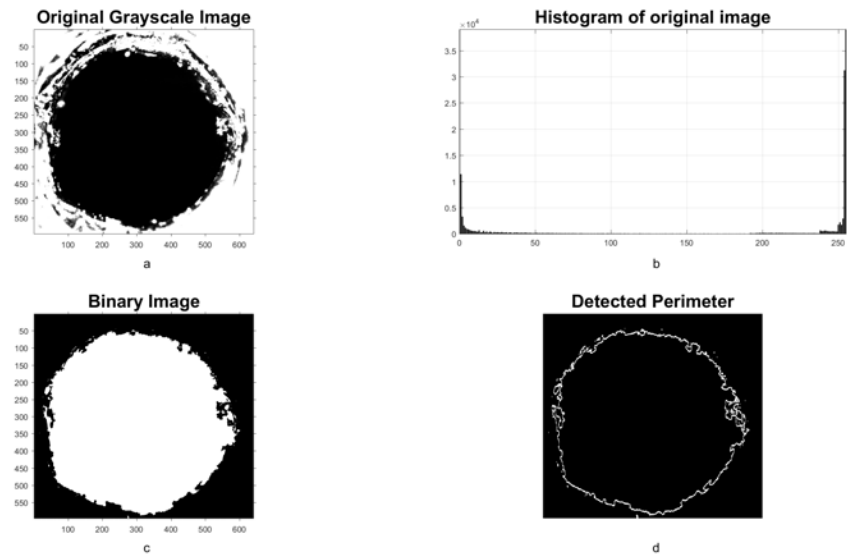
Figure 80. Original, Histogram, Binary, and Perimeter images for Element 8
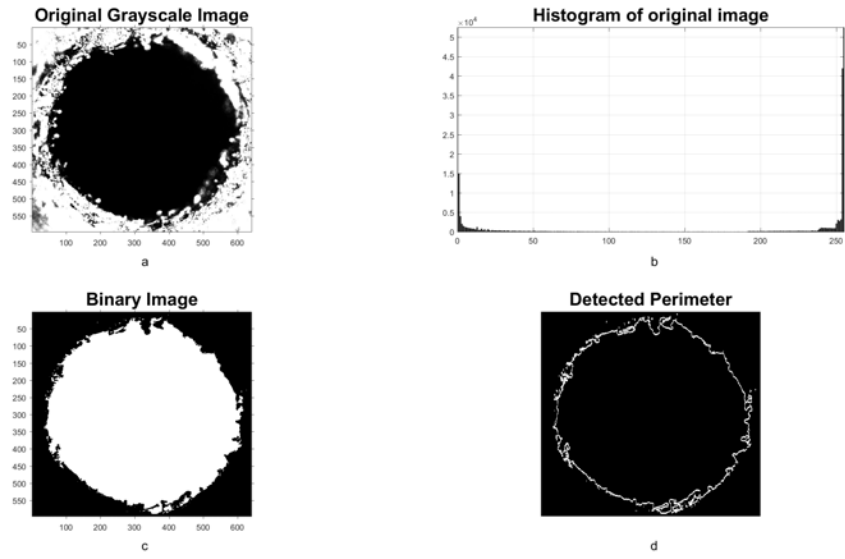
Figure 81. Original, Histogram, Binary, and Perimeter images for Element 9
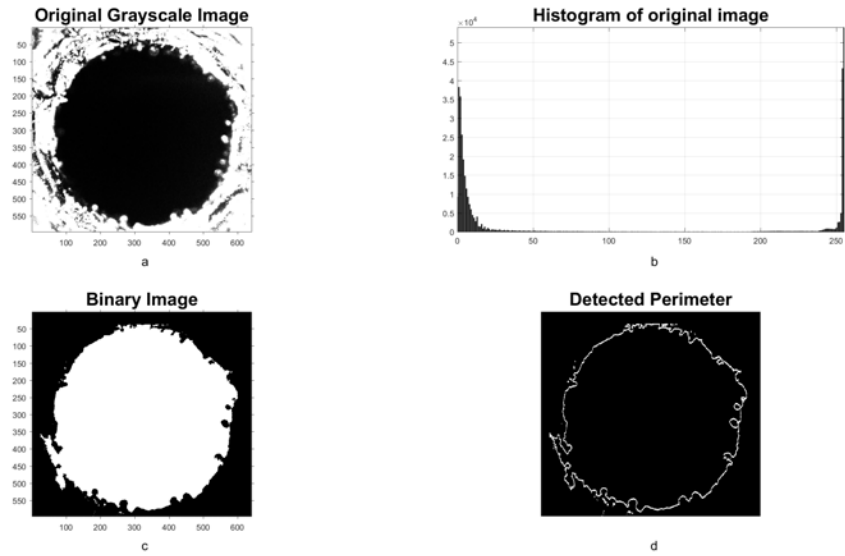
Figure 82. Original, Histogram, Binary, and Perimeter images for Element 10

Design 3.
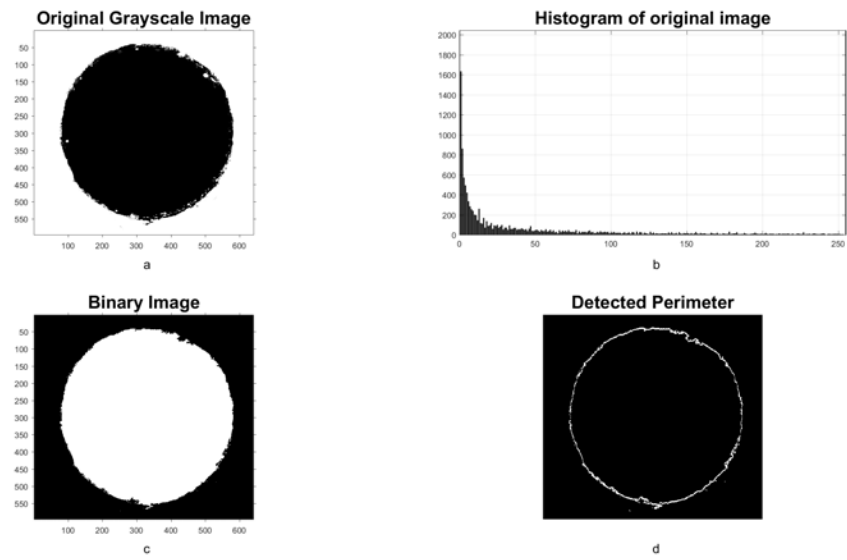
Figure 83. Original, Histogram, Binary, and Perimeter images for Element 12
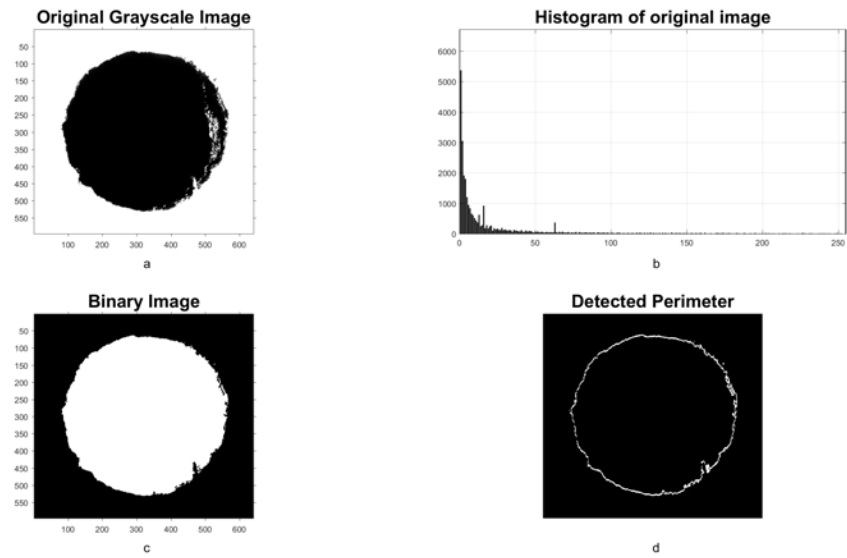
Figure 84. Original, Histogram, Binary, and Perimeter images for Element 13
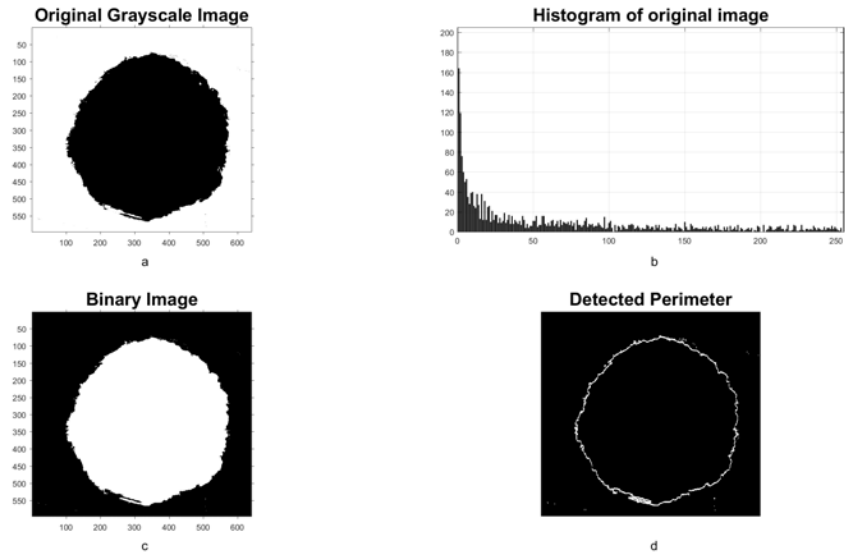
Figure 85. Original, Histogram, Binary, and Perimeter images for Element 14
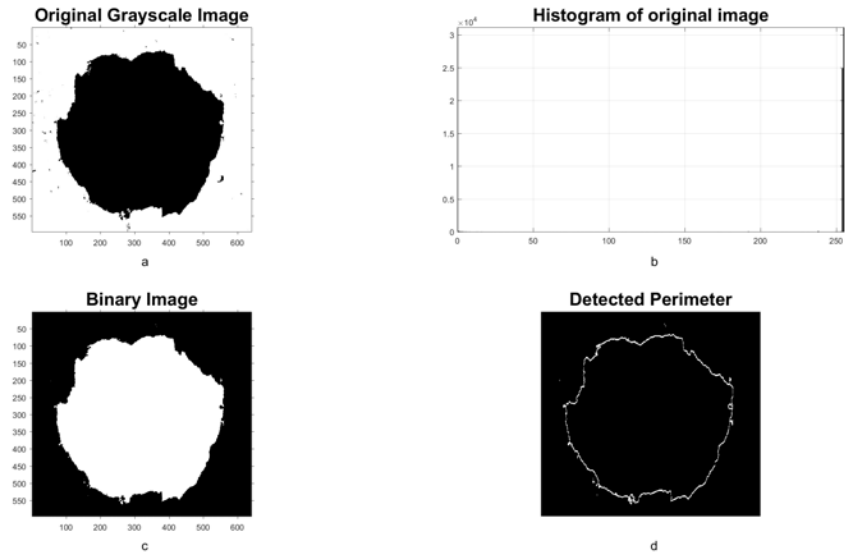
Figure 86. Original, Histogram, Binary, and Perimeter images for Element 15

Design 4.
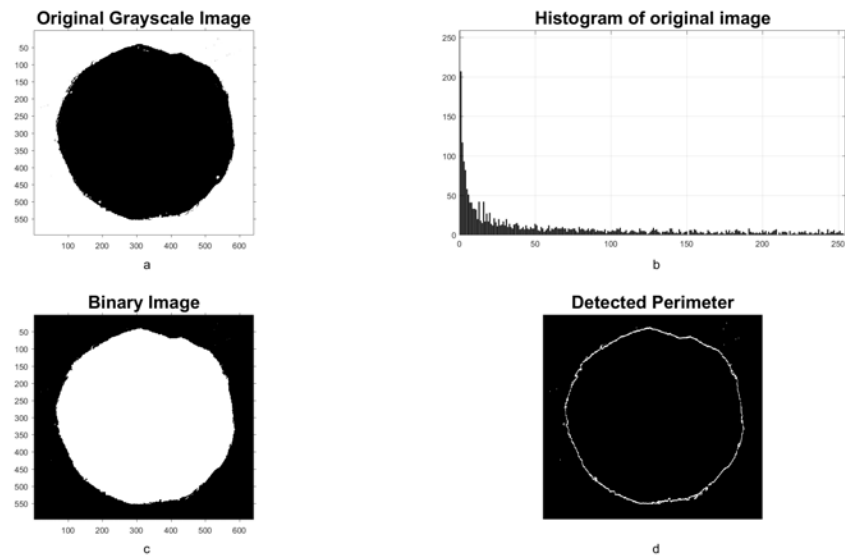
Figure 87. Original, Histogram, Binary, and Perimeter images for Element 17
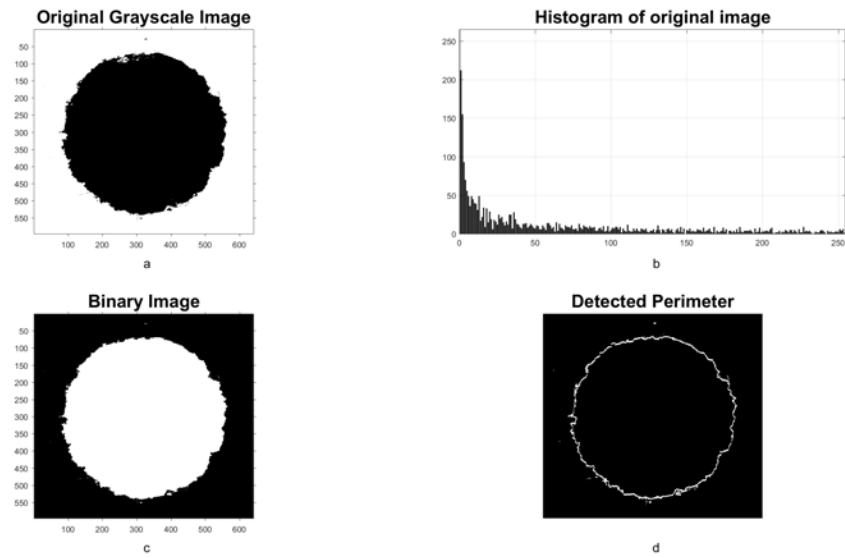
Figure 88. Original, Histogram, Binary, and Perimeter images for Element 18
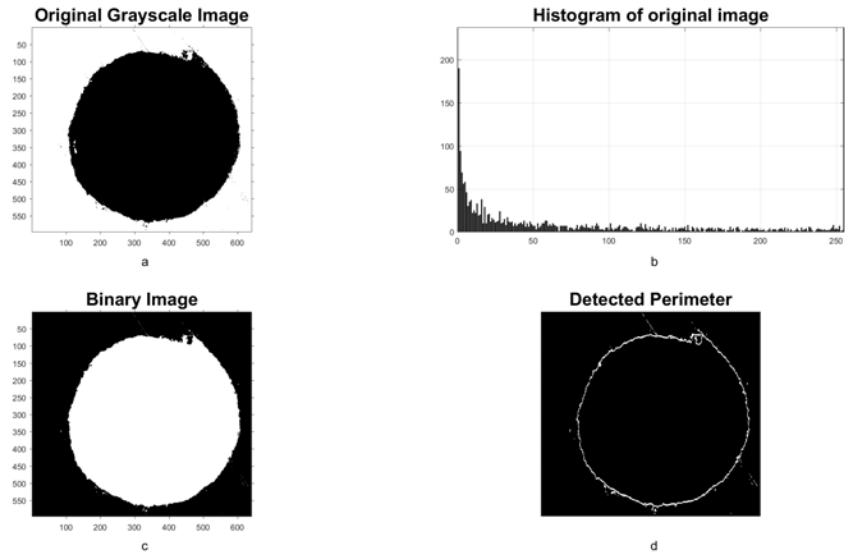
Figure 89. Original, Histogram, Binary, and Perimeter images for Element 19
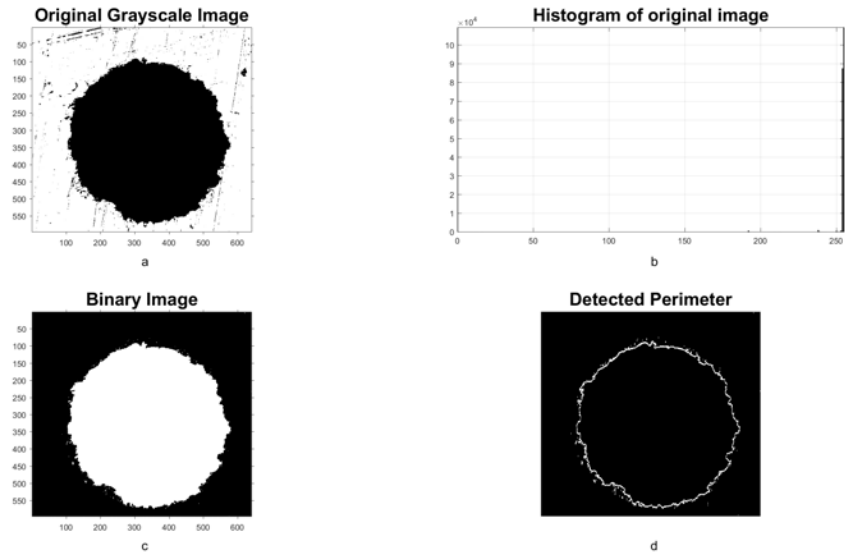
Figure 90. Original, Histogram, Binary, and Perimeter images for Element 20

VIII Appendix 3

Discharge Coefficient Calculator.

```matlab
1  % C D c l a c u l a t o r
2    clear  all ; close all ; clc ;
3    rho = 1000; % approx water density
4    f = 0.10 ; % rough
5    % f = 0.015 ; % smooth
6    % fully developed flow
7    l = 5*10; % mm
8    d = 1 ; % mm
9
10   %%%%%%
11   % Calculate the Area Ratio of the Port to the tank (1/2") to
          the orifice
12   % opening (1mm)
13   Dh1 = (1/2)*0.0254 ; % . 5 inch in meters
14
15
16   A1 = (0.5*Dh1)^2*pi ; % area of Tank port
17   D_h2 = (1/1000) ; % diameter of the injector orifice (1mm)
18   A2 = (0.5*D_h2)^2*pi ; % area of injector orifice
19   % Area Ratio
20   Arearatio = A1/A2
21
22   %%%%%%
```

```matlab
23  v_1 = 0.5 ; % initial velocity (m/s)

24  dp = (1:6000000) ; % dp in Pa from 1 : 6MPa

25  % Fend = 0.25;

26  % step = Fend/ length (dp) ;

27  % F = (step:step:Fend ) ;

28  cd = zeros(size(dp)); % just pre-allocate cd

29  j = 1 ;

30   for i = 1 : length (dp)

31   cd(i) = (sqrt(2*rho*dp(i)+((rho*f*(l/d))^2)-((rho*v_1)^2))-
          rho*f*(l/d))/(sqrt(2*rho*dp(i)));

32   % cd2(i)=(sqrt(2*rho*dp(i)+((rho*F(i)*(l/d))^2)-((rho*v_1)
          ^2))-rho*F(i)*(l/d))/(sqrt(2*rho*dp(1500000)));

33    if cd (i) >=0

34   CD(j) = cd (i) ;

35   DP(j) = dp(i) ;

36    j = j +1;

37   end

38   end

39

40    f = 0.015;

41   cd = zeros(size(dp)); % just pre-allocate cd

42  j = 1 ;

43   for i = 1 : length (dp)

44   cd2(i) = (sqrt(2*rho*dp(i)+((rho*f*(l/d))^2)-((rho*v_1)^2))-
          rho*f*(l/d))/(sqrt(2*rho*dp(i)));
```

```matlab
45  % cd2(i)=(sqrt(2*rho*dp(i)+((rho*F(i)*(l/d))^2)-((rho*v_1)
        ^2))-rho*F(i)*(l/d))/(sqrt(2*rho*dp(1500000)));
46  if cd2 (i) >=0
47  CD2(j) = cd2 (i) ;
48  DP2(j) = dp(i) ;
49  j = j +1;
50  end
51  end
52
53  %figure (1)
54  %semilogy(cd,dp)
55  %ylabel('\Delta P(Pa)')
56  %xlabel('CD')
57  %title('log(\Delta P)')
58
59  figure(2)
60  CD_DP = plot(DP,CD)
61  xlabel('\Delta P (Pa)')
62  ylabel('C_D')
63
64  hold on
65  CD_DP2 = plot(DP2,CD2)
66  xlabel('\Delta P (Pa)')
67  ylabel('C_D')
68  title( 'C_D Vs. \Delta P')
```

```
69   legend('Rough Surface (100 Micron)','Smooth Surface (15
         Micron)')
70   saveas (CD_DP2, 'c_D_Vs_dP25_2.png')
```

Area, Hydraulic perimeter, and Image Calculator.

```
1    clc;      % Clear the command window.
2    close all;  % Close all figures (except those of imtool.)
3    imtool close all;  % Close all imtool figures if you have the
         Image Processing Toolbox.
4    clear;  % Erase all existing variables. Or clearvars if you
         want.
5    workspace;  % Make sure the workspace panel is showing.
6    format long g;
7    format compact;
8    fontSize = 22;
9
10   % Check that user has the Image Processing Toolbox installed.
11   hasIPT = license('test', 'image_toolbox');
12   if ~hasIPT
13       % User does not have the toolbox installed.
14       message = sprintf('Sorry, but you do not seem to have the
             Image Processing Toolbox.\nDo you want to try to
             continue anyway?');
15       reply = questdlg(message, 'Toolbox missing', 'Yes', 'No',
             'Yes');
16       if strcmpi(reply, 'No')
```

```matlab
17            % User said No, so exit.
18              return;
19       end
20  end
21
22
23  for ii = 1:20
24  %
```

==

```matlab
25  % Read in a standard MATLAB gray scale demo image.
26  folder = 'E:\AFIT\RESEARCH\Experimentation\Microscope\Waters'
          ;
27  id = num2str(ii);
28  image_id = strcat(id,'_5X');
29  ScalingFactor = 2.05*2.05; % Micron/ Pixel
30  baseFileName = strcat(image_id,'.bmp');
31  % Get the full filename, with path prepended.
32  fullFileName = fullfile(folder, baseFileName);
33  % Check if file exists.
34  if ~exist(fullFileName, 'file')
35      % File doesn't exist — didn't find it there.  Check the
           search path for it.
36      fullFileNameOnSearchPath = baseFileName; % No path this
           time.
37      if ~exist(fullFileNameOnSearchPath, 'file')
```

```matlab
38          % Still didn't find it.  Alert user.
39          errorMessage = sprintf('Error: %s does not exist in
                the search path folders.', fullFileName);
40          uiwait(warndlg(errorMessage));
41          return;
42      end
43  end
44  grayImage = imread(fullFileName);
45  original = imread(strcat(image_id,'_original.bmp'));
46  % Get the dimensions of the image.
47  % numberOfColorBands should be = 1.
48  input_im = grayImage;
49  [rows, columns, numberOfColorBands] = size(grayImage);
50  if numberOfColorBands > 1
51      % It's not really gray scale like we expected − it's
            color.
52      % Convert it to gray scale by taking only the green
            channel.
53      grayImage = grayImage(:, :, 2); % Take green channel.
54  end
55
56  % Display the original gray scale image.
57
58  % Let's compute and display the histogram.
59  [pixelCount, grayLevels] = imhist(grayImage);
60
```

113

```matlab
61  binaryImage = grayImage < 100 ;
62  % Display the binary image.
63
64  % Fill the binary image.
65  binaryImage = imfill(binaryImage,'holes');
66
67  input_im = rgb2gray(input_im);
68
69  sum_of_x_axis=sum(input_im,1);
70  sum_of_y_axis=sum(input_im,2);
71
72  location_of_object_on_x=find(sum_of_x_axis>0);
73
74  location_of_object_on_y=find(sum_of_y_axis>0);
75
76  seperated_object=input_im(location_of_object_on_y(1):...
77      location_of_object_on_y(end),location_of_object_on_x(1)
            :...
78      location_of_object_on_x(end));
79
80  detected_outer_surface=im2bw(seperated_object);
81  [n, m] = size(detected_outer_surface);
82  counter = 0;
83  for i = 1:n
84      for j = 1:m
85          if detected_outer_surface(i,j) < 1
```

```matlab
86                    detected_outer_surface(i,j) = 1;
87                    counter = counter+1;
88                else
89                    detected_outer_surface(i,j) = 0;
90                end
91        end
92  end
93
94  sum_of_outer_space=0;
95  for  i=1:size(seperated_object,1)
96        if  seperated_object(i,1)>0
97            break
98        end
99        for  j=1:size(seperated_object,2)
100            if  seperated_object(i,j)>0
101                break
102            end
103            detected_outer_surface(i,j)=1;
104            sum_of_outer_space=sum_of_outer_space+1;
105        end
106  end
107
108  for  i=1:size(seperated_object,1)
109        if  seperated_object(i,size(seperated_object,2))>0
110            break
111        end
```

```matlab
112        for j=size(seperated_object,2):-1:1
113            if seperated_object(i,j)>0
114                break
115            end
116            detected_outer_surface(i,j)=1;
117            sum_of_outer_space=sum_of_outer_space+1;
118        end
119    end
120
121    Perimeter = bwperim(binaryImage);
122    perimeter2(ii) = sum(sum(Perimeter==1))*sqrt(ScalingFactor)
           /1000; % mm
123    name = strcat('Perimeter ',id) ;
124
125    sprintf('Perimeter %.0f = %0.3f',ii,perimeter2(ii))
126
127    Area_of_object=size(seperated_object,1)*size(seperated_object
           ,2);
128
129    Area_of_object=Area_of_object-sum_of_outer_space*
           ScalingFactor;
130
131    Height_of_the_line=max(sum_of_x_axis);
132
133    Area1 = pi*.5^2;
134    Area2 = bwarea(detected_outer_surface)*ScalingFactor/1e6;
```

```matlab
135  Area_calc = Area_of_object * ScalingFactor /1e6;

136

137  % Calculate the area using bwarea().
138  area3 = bwarea(binaryImage) * ScalingFactor /1e6;
139  % Calculate the area in pixels using sum()
140  area4 = sum(detected_outer_surface(:) * ScalingFactor )/1e6;

141

142  figure(1)
143  subplot(2, 2, 1);
144  imshow(original, []);
145  axis on;
146  title('Original Grayscale Image', 'FontSize', fontSize);
147  % Enlarge figure to full screen.
148  set(gcf, 'Units', 'Normalized', 'OuterPosition', [0 0 1 1]);
149  % Give a name to the title bar.
150  set(gcf, 'Name', 'Demo by ImageAnalyst', 'NumberTitle', 'Off'
        )

151

152  subplot(2, 2, 2);
153  bar(grayLevels, pixelCount);
154  grid on;
155  title('Histogram of original image', 'FontSize', fontSize);
156  xlim([0 grayLevels(end)]); % Scale x axis manually.
157  ylim([0 max(pixelCount(2:end-1))*1.25]);

158

159  subplot(2, 2, 3);
```

```matlab
160  imshow(binaryImage, []);

161  axis on;

162  title('Binary Image', 'FontSize', fontSize);

163

164  subplot(2,2,4)

165  imshow(Perimeter.*5)

166  title('Detected Perimeter','FontSize', fontSize);

167

168  print(figure(1),strcat(image_id,'comparison'),'-dpng')

169  close all

170  end
```

IX Appendix 4

Table 21. Design 1 experimental results

Element	Run	Run Time	Pressure (Pa)	Mass Flow (g/s)	Change From CFD (%)	Cd (Exp.)	Change From CFD (%)	Change From Text (%)	Re
1	1	4.369	1,236,363	29.301	4.32%	0.547	27.28%	21.26%	65,811
1	2	5.045	1,189,966	32.904	7.45%	0.626	16.76%	9.86%	73,905
1	3	5.744	1,258,528	33.773	10.29%	0.625	16.92%	10.04%	75,855
1	4	10.015	1,255,301	33.947	10.86%	0.629	16.38%	9.46%	76,248
1	5	9.879	1,222,936	31.987	4.46%	0.601	20.18%	13.57%	71,844
1	6	9.716	1,194,940	32.112	4.87%	0.610	18.93%	12.22%	72,125
1	7	11.857	1,240,960	32.555	6.31%	0.607	19.35%	12.67%	73,121
1	Avg	8.089	1,228,428	32.368	6.94%	0.607	19.40%	12.72%	72,701
2	1	9.138	1,167,794	34.799	13.64%	0.461	38.75%	33.68%	96,257
2	2	9.605	1,167,779	34.773	13.56%	0.461	38.80%	33.73%	96,186
2	3	9.776	1,215,047	36.008	17.59%	0.468	37.87%	32.72%	99,602
2	4	10.908	1,173,701	34.836	13.76%	0.460	38.84%	33.78%	96,359
2	5	9.459	1,205,245	35.943	17.38%	0.469	37.73%	32.57%	99,422
2	6	8.861	1,169,575	35.886	17.19%	0.475	36.89%	31.66%	99,263
2	7	10.492	1,210,126	35.836	17.03%	0.466	38.04%	32.91%	99,125
2	Avg	9.749	1,187,038	35.440	15.74%	0.466	38.13%	33.01%	98,031
3	1	10.233	1,173,575	29.512	3.62%	0.597	20.69%	14.13%	66,855
3	2	12.249	1,167,946	29.553	3.49%	0.599	20.39%	13.80%	66,947
3	3	15.092	1,162,144	30.347	0.90%	0.617	18.05%	11.27%	68,746
3	4	13.807	1,239,707	30.420	0.66%	0.599	20.47%	13.88%	68,911
3	5	12.229	1,245,111	30.583	0.13%	0.600	20.21%	13.61%	69,282
3	6	10.366	1,243,544	30.678	0.18%	0.603	19.91%	13.28%	69,496
3	7	10.530	1,239,743	30.389	0.76%	0.598	20.55%	13.97%	68,842
3	Avg	12.072	1,210,253	30.212	1.39%	0.602	20.04%	13.42%	68,440

Table 21. Design 1 experimental results

Element	Run	Run Time	Pressure (Pa)	Mass Flow (g/s)	Change From CFD (%)	Cd (Exp.)	Change From CFD (%)	Change From Text (%)	Re
4	1	11.411	1,226,037	30.672	0.16%	0.578	23.24%	16.89%	50,650
4	2	11.5425	1,219,743	30.669	0.15%	0.579	23.05%	16.68%	50,646
4	3	12.510	1,207,589	30.695	0.24%	0.582	22.60%	16.20%	50,688
4	4	10.781	1,229,588	30.793	0.56%	0.579	23.05%	16.68%	50,850
4	5	10.580	1,209,716	30.812	0.62%	0.584	22.38%	15.95%	50,882
4	6	9.808	1,212,328	30.792	0.56%	0.583	22.51%	16.09%	50,848
4	7	9.862	1,205,322	30.623	0.01%	0.582	22.71%	16.31%	50,570
4	Avg	10.928	1,215,761	30.722	0.33%	0.581	22.79%	16.40%	50,733
5	1	9.046	1,225,707	31.394	2.52%	0.577	23.36%	17.01%	59,057
5	2	12.359	1,228,319	31.394	2.52%	0.576	23.44%	17.10%	59,057
5	3	14.180	1,219,392	31.594	3.17%	0.582	22.67%	16.27%	59,433
5	4	9.469	1,228,566	31.681	3.46%	0.581	22.75%	16.35%	59,597
5	5	11.634	1,218,348	31.287	2.17%	0.577	23.39%	17.04%	58,856
5	6	12.355	1,231,689	31.242	2.02%	0.573	23.91%	17.61%	58,771
5	7	11.195	1,244,966	31.801	3.85%	0.580	22.97%	16.59%	59,822
5	Avg	11.463	1,228,141	31.484	2.82%	0.578	23.21%	16.85%	59,228

Table 22. Statistical data for design 1

Variable	Standard Deviation	Average All
RE	16,102	69,827
Mass Flow Rate (g/s)	1.961	32
Difference From CFD (%)	6%	5%
Cd (Experimental)	0.053	0.567
Difference From CFD (%)	7%	25%
Difference From Text (%)	8%	18%

Table 23. Design 1 additional pressures data

Pressure	Run	Mass Flow (g/s)	Change from CFD (%)	Cd (Exp)	Change from CFD (%)	Change from Text (%)	Re
50	1	16.910	45%	0.579	23%	17%	37,981
50	2	17.045	44%	0.595	21%	14%	38,283
50	3	16.251	47%	0.568	25%	18%	36,500
50	4	16.740	45%	0.575	24%	17%	37,600
50	5	17.270	44%	0.602	20%	13%	38,789
	Avg	16.843	45%	0.584	22%	16%	37,831
100	1	23.283	24%	0.577	23%	17%	52,296
100	2	23.419	24%	0.580	23%	17%	52,600
100	3	23.007	25%	0.571	24%	18%	51,675
100	4	23.626	23%	0.586	22%	16%	53,067
100	5	22.973	25%	0.573	24%	17%	51,598
	Avg	23.262	24%	0.578	23%	17%	52,247
125	1	26.213	14%	0.584	22%	16%	58,877
125	2	25.685	16%	0.572	24%	18%	57,690
125	3	26.057	15%	0.576	23%	17%	58,525

Table 23. Design 1 additional pressures data

Pressure	Run	Mass Flow (g/s)	Change from CFD (%)	Cd (Exp)	Change from CFD (%)	Change from Text (%)	Re
125	4	26.217	14%	0.582	23%	16%	58,884
125	5	26.175	15%	0.582	23%	16%	58,791
	Avg	26.069	15%	0.579	23%	17%	58,553
150	1	28.014	9%	0.571	24%	18%	62,921
150	2	28.490	7%	0.581	23%	16%	63,990
150	3	28.780	6%	0.583	22%	16%	64,641
150	4	28.533	7%	0.585	22%	16%	64,086
150	5	25.846	16%	0.527	30%	24%	58,053
	Avg	27.933	9%	0.570	24%	18%	62,738
180	1	29.301	4%	0.547	27%	21%	65,811
180	2	32.904	7%	0.626	17%	10%	73,905
180	3	33.773	10%	0.625	17%	10%	75,855
180	4	33.947	11%	0.629	16%	9%	76,248
180	5	31.987	4%	0.601	20%	14%	71,844
180	6	32.112	5%	0.610	19%	12%	72,125
180	7	32.555	6%	0.607	19%	13%	73,121
	Avg	32.368	7%	0.607	19%	13%	72,701

Table 24. Design 2 experimental results

Element	Run	Run Time	Pressure (Pa)	Mass Flow (g/s)	Change From CFD (%)	Cd (Exp.)	Change From CFD (%)	Change From Text (%)	Re
6	1	10.590	1,249,062.78	29.839	10.98%	0.524	19.59%	19.31%	93,994
6	2	11.396	1,246,168.53	30.185	12.27%	0.531	18.57%	18.28%	95,086
6	3	11.483	1,229,663.61	29.957	11.42%	0.531	18.64%	18.36%	94,367
6	4	13.465	1,242,651.48	30.152	12.15%	0.531	18.54%	18.26%	94,980
6	5	11.398	1,241,693.57	30.356	12.91%	0.535	17.96%	17.67%	95,623

Table 24. Design 2 experimental results

Element	Run	Run Time	Pressure (Pa)	Mass Flow (g/s)	Change From CFD (%)	Cd (Exp.)	Change From CFD (%)	Change From Text (%)	Re
6	6	16.447	1,240,328.65	30.035	11.71%	0.530	18.78%	18.50%	94,613
6	7	12.717	1,238,199.92	30.196	12.31%	0.533	18.27%	17.99%	95,120
6	Avg	12.500	1,241,109.79	30.103	11.97%	0.531	18.62%	18.34%	94,826
7	1	11.616	1,245,371.42	28.410	5.67%	0.596	8.68%	8.36%	66,935
7	2	12.290	1,237,742.89	27.991	4.11%	0.589	9.75%	9.44%	65,948
7	3	13.412	1,236,812.41	29.376	9.26%	0.618	5.25%	4.92%	69,210
7	4	12.675	1,239,859.54	29.192	8.58%	0.613	5.96%	5.63%	68,778
7	5	16.247	1,240,435.01	29.051	8.05%	0.610	6.43%	6.11%	68,446
7	6	11.848	1,232,789.67	29.204	8.62%	0.615	5.65%	5.32%	68,807
7	7	13.576	1,235,077.32	28.876	7.40%	0.608	6.80%	6.48%	68,032
7	Avg	13.095	1,238,298.32	28.871	7.39%	0.607	6.93%	6.61%	68,022
8	1	12.469	1,247,800.54	29.514	9.77%	0.638	2.19%	1.85%	78,047
8	2	13.978	1,237,998.82	29.332	9.10%	0.637	2.41%	2.07%	77,567
8	3	18.322	1,232,428.99	29.363	9.21%	0.639	2.08%	1.74%	77,649
8	4	16.315	1,231,058.12	29.420	9.43%	0.640	1.84%	1.50%	77,800
8	5	14.342	1,233,022.73	29.703	10.48%	0.646	0.97%	0.63%	78,549
8	6	13.901	1,232,808.22	29.782	10.77%	0.648	0.70%	0.36%	78,757
8	7	16.272	1,228,585.66	29.990	11.55%	0.653	0.16%	0.51%	79,308
8	Avg	15.086	1,234,814.72	29.586	10.04%	0.643	1.48%	1.24%	78,239
9	1	13.92	1,244,839	30.306	12.72%	0.626	3.97%	3.64%	87,960
9	2	17.36	1,231,002	29.960	11.44%	0.623	4.54%	4.20%	86,956
9	3	12.40	1,226,633	29.689	10.43%	0.618	5.23%	4.90%	86,169
9	4	18.03	1,225,331	29.833	10.96%	0.621	4.72%	4.39%	86,585
9	5	10.16	1,231,007	30.131	12.07%	0.626	3.99%	3.66%	87,452
9	6	17.27	1,231,079	30.102	11.96%	0.626	4.09%	3.75%	87,368

Table 24. Design 2 experimental results

Element	Run	Run Time	Pressure (Pa)	Mass Flow (g/s)	Change From CFD (%)	Cd (Exp.)	Change From CFD (%)	Change From Text (%)	Re
9	7	16.06	1,233,436	29.890	11.18%	0.621	4.85%	4.52%	86,753
9	Avg	15.03	1,231,904	29.987	11.54%	0.623	4.48%	4.15%	87,035
10	1	14.203	1,242,639	29.008	7.89%	0.622	4.59%	4.26%	70,175
10	2	14.933	1,224,463	28.930	7.60%	0.625	4.15%	3.81%	69,985
10	3	18.859	1,220,515	28.846	7.29%	0.624	4.27%	3.94%	69,783
10	4	16.739	1,222,133	29.154	8.44%	0.631	3.31%	2.98%	70,527
10	5	17.238	1,222,348	28.890	7.45%	0.625	4.20%	3.86%	69,889
10	6	16.587	1,221,889	28.817	7.18%	0.623	4.42%	4.09%	69,712
10	7	13.016	1,223,620	28.888	7.45%	0.625	4.25%	3.92%	69,885
10	Avg	15.939	1,225,372	28.933	7.62%	0.625	4.17%	3.84%	69,994

Table 25. Statistical data for design 2

Variable	Standard Deviation	Average All
RE	10,173	79,623
Mass Flow Rate (g/s)	0.577	29.496
Difference From CFD (%)	2%	10%
Cd (Experimental)	0.040	0.606
Difference From CFD (%)	6%	7%
Difference From Text (%)	6%	7%

Table 26. Design 2 additional pressures data

Pressure	Run	Mass Flow (g/s)	Change from CFD (%)	Cd (Exp)	Change from CFD (%)	Change from Text (%)	Re
50	1	15.389	43%	0.511	22%	21%	48,475
50	2	15.580	42%	0.523	20%	20%	49,077

Table 26. Design 2 additional pressures data

Pressure	Run	Mass Flow (g/s)	Change from CFD (%)	Cd (Exp)	Change from CFD (%)	Change from Text (%)	Re
50	3	15.956	41%	0.539	17%	17%	50,262
50	4	15.877	41%	0.523	20%	20%	50,014
50	5	15.438	43%	0.523	20%	20%	48,631
	Avg	15.648	42%	0.524	20%	19%	49,292
100	1	22.578	16%	0.538	17%	17%	71,122
100	2	22.699	16%	0.543	17%	16%	71,503
100	3	22.555	16%	0.546	16%	16%	71,050
100	4	21.980	18%	0.530	19%	18%	69,240
100	5	21.766	19%	0.526	19%	19%	68,564
	Avg	22.316	17%	0.537	18%	17%	70,296
125	1	26.088	3%	0.535	18%	18%	82,178
125	2	26.455	2%	0.548	16%	16%	83,334
125	3	25.964	3%	0.536	18%	17%	81,789
125	4	26.023	3%	0.535	18%	18%	81,975
125	5	26.654	1%	0.552	15%	15%	83,961
	Avg	26.237	2%	0.541	17%	17%	82,647
150	1	28.319	5%	0.542	17%	17%	89,206
150	2	27.933	4%	0.542	17%	17%	87,989
150	3	27.672	3%	0.537	18%	17%	87,167
150	4	27.449	2%	0.532	18%	18%	86,465
150	5	27.785	3%	0.540	17%	17%	87,525
	Avg	27.831	4%	0.539	17%	17%	87,671
180	1	29.839	11%	0.524	20%	19%	93,994
180	2	30.185	12%	0.531	19%	18%	95,086

Table 26. Design 2 additional pressures data

Pressure	Run	Mass Flow (g/s)	Change from CFD (%)	Cd (Exp)	Change from CFD (%)	Change from Text (%)	Re
180	3	29.957	11%	0.531	19%	18%	94,367
180	4	30.152	12%	0.531	19%	18%	94,980
180	5	30.356	13%	0.535	18%	18%	95,623
180	6	30.035	12%	0.530	19%	18%	94,613
180	7	30.196	12%	0.533	18%	18%	95,120
	Avg	30.103	12%	0.531	19%	18%	94,826

Table 27. Design 3 experimental results

Element	Run	Run Time	Pressure (Pa)	Mass Flow (g/s)	Change From CFD (%)	Cd (Exp.)	Change From CFD (%)	Change From Text (%)	Re
11	1	12.633	1,239,360	27.073	1.30%	0.736	13.57%	6.79%	41,994
11	2	13.637	1,245,135	26.839	0.42%	0.728	12.33%	7.81%	41,631
11	3	14.116	1,257,805	26.921	0.73%	0.727	12.10%	7.99%	41,758
11	4	13.993	1,250,011	26.585	0.53%	0.720	11.05%	8.86%	41,237
11	5	16.047	1,254,264	26.672	0.20%	0.721	11.23%	8.72%	41,372
11	6	15.114	1,243,638	26.863	0.51%	0.729	12.50%	7.67%	41,668
11	7	17.281	1,245,161	26.504	0.83%	0.719	10.93%	8.96%	41,111
11	Avg	14.688	1,247,911	26.779	0.65%	0.726	11.96%	8.11%	41,539
12	1	12.556	1,262,411	30.902	15.63%	0.728	12.29%	7.84%	58,244
12	2	11.369	1,242,369	31.137	16.51%	0.739	14.05%	6.40%	58,686
12	3	14.936	1,243,057	31.065	16.24%	0.738	13.75%	6.64%	58,550
12	4	15.478	1,247,182	31.140	16.52%	0.738	13.84%	6.57%	58,692
12	5	13.660	1,242,675	31.479	17.79%	0.747	15.29%	5.38%	59,330
12	6	10.981	1,241,856	31.327	17.22%	0.744	14.77%	5.81%	59,044
12	7	11.164	1,235,472	31.172	16.64%	0.742	14.50%	6.03%	58,752
12	Avg	12.878	1,245,003	31.175	16.65%	0.740	14.07%	6.38%	58,757

Table 27. Design 3 experimental results

Element	Run	Run Time	Pressure (Pa)	Mass Flow (g/s)	Change From CFD (%)	Cd (Exp.)	Change From CFD (%)	Change From Text (%)	Re
13	1	12.850	1,259,046.73	25.992	2.74%	0.713	10.02%	9.70%	55,603
13	2	13.656	1,250,638.21	25.777	3.55%	0.710	9.48%	10.15%	55,144
13	3	11.578	1,237,047.95	25.739	3.69%	0.713	9.91%	9.79%	55,062
13	4	14.443	1,226,784.33	25.757	3.63%	0.716	10.45%	9.35%	55,100
13	5	14.916	1,245,631.18	26.012	2.67%	0.718	10.70%	9.15%	55,647
13	6	15.290	1,235,232.88	26.161	2.11%	0.725	11.80%	8.24%	55,965
13	7	14.250	1,233,863.54	26.526	0.75%	0.735	13.42%	6.91%	56,746
13	Avg	13.855	1,241,177.83	25.995	2.73%	0.719	10.83%	9.04%	55,610
14	1	15.46	1,258,537	25.477	4.67%	0.702	8.26%	11.15%	54,039
14	2	16.15	1,248,197	25.508	4.55%	0.706	8.84%	10.67%	54,104
14	3	14.92	1,232,771	25.060	6.23%	0.698	7.60%	11.69%	53,154
14	4	19.16	1,229,984	24.945	6.66%	0.695	7.22%	12.00%	52,909
14	5	16.46	1,235,998	24.783	7.27%	0.689	6.27%	12.78%	52,566
14	6	15.03	1,237,065	25.012	6.41%	0.695	7.20%	12.01%	53,053
14	Avg	16.20	1,240,425	25.131	5.97%	0.697	7.57%	11.72%	53,304
15	1	19.599	1,222,413	22.756	14.85%	0.619	4.48%	21.60%	43,928
15	2	13.404	1,201,271	23.127	13.46%	0.635	2.07%	19.63%	44,643
15	3	13.405	1,209,210	22.976	14.03%	0.629	3.03%	20.41%	44,352
15	4	18.339	1,211,175	22.793	14.71%	0.623	3.88%	21.11%	43,998
15	5	10.368	1,236,622	23.535	11.94%	0.637	1.78%	19.39%	45,430
15	6	12.481	1,233,946	23.555	11.86%	0.638	1.59%	19.23%	45,470
15	7	13.737	1,229,181	23.585	11.75%	0.640	1.27%	18.97%	45,528
	Avg	14.476	1,220,545.40	23.190	0.132	0.632	0.026	0.2018	44,764

Table 28. Statistical data for design 3

Variable	Standard Deviation	Average All
RE	6,694	50,878
Mass Flow Rate (g/s)	2.678	27
Difference From CFD (%)	6%	8%
Cd (Experimental)	0.038	0.705
Difference From CFD (%)	4%	10%
Difference From Text (%)	5%	11%

Table 29. Design 3 additional pressures data

Pressure	Run	Mass Flow (g/s)	Change from CFD (%)	Cd (Exp)	Change from CFD (%)	Change from Text (%)	Re
50	1	15.137	43%	0.729	13%	8%	23,480
50	2	14.870	44%	0.731	13%	7%	23,066
50	3	14.636	45%	0.720	11%	9%	22,703
50	4	14.798	45%	0.729	12%	8%	22,954
50	5	14.807	45%	0.726	12%	8%	22,967
	Avg	14.850	44%	0.727	12%	8%	23,034
100	1	20.300	24%	0.726	12%	8%	31,488
100	2	20.515	23%	0.729	12%	8%	31,822
100	3	20.152	25%	0.713	10%	10%	31,258
100	4	20.609	23%	0.730	13%	8%	31,967
100	5	20.478	23%	0.734	13%	7%	31,764
	Avg	20.411	24%	0.726	12%	8%	31,660
125	1	22.577	16%	0.723	12%	8%	35,020
125	2	23.106	14%	0.743	15%	6%	35,840
125	3	22.925	14%	0.738	14%	7%	35,560
125	4	22.741	15%	0.730	13%	8%	35,275
125	5	22.790	15%	0.730	13%	8%	35,350

Table 29. Design 3 additional pressures data

Pressure	Run	Mass Flow (g/s)	Change from CFD (%)	Cd (Exp)	Change from CFD (%)	Change from Text (%)	Re
	Avg	22.828	15%	0.733	13%	7%	35,409
150	1	23.781	11%	0.705	9%	11%	36,887
150	2	24.320	9%	0.720	11%	9%	37,723
150	3	24.080	10%	0.715	10%	9%	37,351
150	4	24.308	9%	0.724	12%	8%	37,705
150	5	24.117	10%	0.712	10%	10%	37,409
	Avg	24.121	10%	0.715	10%	9%	37,415
180	1	27.073	1%	0.736	14%	7%	41,994
180	2	26.839	0%	0.728	12%	8%	41,631
180	3	26.921	1%	0.727	12%	8%	41,758
180	4	26.585	1%	0.720	11%	9%	41,237
175	5	26.672	0%	0.721	11%	9%	41,372
180	6	26.863	1%	0.729	12%	8%	41,668
180	7	26.504	1%	0.719	11%	9%	41,111
	Avg	26.779	1%	0.726	12%	8%	41,539

Table 30. Design 4 experimental results

Element	Run	Run Time	Pressure (Pa)	Mass Flow (g/s)	Change From CFD (%)	Cd (Exp.)	Change From CFD (%)	Change From Text (%)	Re
16	1	14.566	1,210,976	28.696	17.70%	0.697	17.62%	15.02%	50,452
16	2	18.443	1,206,046	28.629	17.90%	0.697	17.65%	15.04%	50,335
16	3	16.795	1,203,263	28.462	18.38%	0.693	18.04%	15.44%	50,039
16	4	15.426	1,202,464	28.913	17.08%	0.705	16.71%	14.07%	50,833
16	5	17.795	1,198,703	28.435	18.45%	0.694	17.96%	15.36%	49,992
16	6	19.049	1,199,507	28.663	17.80%	0.699	17.33%	14.71%	50,394
16	7	15.724	1,200,778	28.745	17.56%	0.701	17.13%	14.51%	50,538
16	Avg	16.828	1,203,105	28.649	17.84%	0.698	17.49%	14.88%	50,369

Table 30. Design 4 experimental results

Element	Run	Run Time	Pressure (Pa)	Mass Flow (g/s)	Change From CFD (%)	Cd (Exp.)	Change From CFD (%)	Change From Text (%)	Re
17	1	10.037	1,195,087	30.289	13.14%	0.719	15.05%	12.36%	48,149
17	2	11.682	1,207,443	30.645	12.11%	0.723	14.49%	11.78%	48,715
17	3	15.477	1,182,139	30.497	12.54%	0.728	14.00%	11.28%	48,479
17	4	11.478	1,169,358	30.319	13.05%	0.727	14.03%	11.31%	48,196
17	5	11.913	1,235,895	31.227	10.45%	0.729	13.87%	11.15%	49,640
17	6	14.557	1,221,930	30.776	11.74%	0.722	14.63%	11.93%	48,922
17	7	10.410	1,221,272	31.125	10.74%	0.731	13.64%	10.91%	49,477
17	Avg	12.222	1,204,732	30.697	11.97%	0.725	14.24%	11.53%	48,797
18	1	12.027	1,245,301	25.276	27.51%	0.693	18.07%	15.48%	52,495
18	2	12.592	1,231,376	25.095	28.03%	0.692	18.20%	15.61%	52,119
18	3	14.047	1,233,328	25.058	28.14%	0.690	18.39%	15.80%	52,043
18	4	12.478	1,218,820	24.843	28.75%	0.689	18.60%	16.03%	51,597
18	5	13.556	1,220,642	24.787	28.92%	0.686	18.85%	16.28%	51,479
18	6	14.928	1,217,633	24.919	28.54%	0.691	18.32%	15.73%	51,754
18	7	13.820	1,222,675	25.760	26.12%	0.713	15.73%	13.07%	53,501
18	Avg	13.350	1,227,111	25.105	28.00%	0.693	18.02%	15.43%	52,141
19	1	13.50	1,254,962	29.471	15.48%	0.713	15.69%	13.02%	54,552
19	2	17.33	1,215,495	28.513	18.23%	0.701	17.11%	14.49%	52,779
19	3	17.74	1,214,718	28.525	18.19%	0.702	17.05%	14.43%	52,801
19	4	12.65	1,208,466	28.776	17.47%	0.710	16.10%	13.45%	53,266
19	5	14.75	1,219,172	28.746	17.56%	0.706	16.56%	13.92%	53,210
19	6	15.75	1,224,054	29.211	16.23%	0.716	15.38%	12.70%	54,071
19	7	20.29	1,215,604	28.785	17.45%	0.708	16.33%	13.68%	53,282
19	Avg	16.001	1221782	28.861	0.172	0.708	0.163	0.137	53,423
20	1	14.696	1,238,280	24.768	28.97%	0.683	19.31%	16.76%	58,897

Table 30. Design 4 experimental results

Element	Run	Run Time	Pressure (Pa)	Mass Flow (g/s)	Change From CFD (%)	Cd (Exp.)	Change From CFD (%)	Change From Text (%)	Re
20	2	11.908	1,206,312	24.522	29.68%	0.685	19.06%	16.50%	58,312
20	3	18.234	1,217,744	24.570	29.54%	0.683	19.28%	16.73%	58,427
20	4	14.735	1,217,676	24.975	28.38%	0.694	17.95%	15.35%	59,389
20	5	11.210	1,219,261	24.620	29.39%	0.684	19.17%	16.61%	58,546
20	6	14.820	1,225,983	24.562	29.56%	0.680	19.58%	17.04%	58,407
20	7	12.940	1,206,165	24.420	29.97%	0.682	19.39%	16.84%	58,071
20	Avg	14.078	1,218,774	24.634	29.35%	0.684	19.10%	16.55%	58,578

Table 31. Statistical data for design 4

Variable	Standard Deviation	Average All
RE	3,387	52,662
Mass Flow Rate (g/s)	2.353	28
Difference From CFD (%)	7%	21%
Cd (Experimental)	0.015	0.7018
Difference From CFD (%)	2%	17%
Difference From Text (%)	2%	14%

Table 32. Design 4 additional pressures data

Pressure	Run	Mass Flow (g/s)	Change from CFD (%)	Cd (Exp)	Change from CFD (%)	Change from Text (%)	Re
50	1	15.319	56%	0.696	18%	15%	26,933
50	2	15.324	56%	0.706	16%	14%	26,942
50	3	15.225	56%	0.697	18%	15%	26,767
50	4	15.206	56%	0.700	17%	15%	26,734
50	5	15.198	56%	0.701	17%	15%	26,720
	Avg	15.254	56%	0.700	17%	15%	26,819

Table 32. Design 4 additional pressures data

Pressure	Run	Mass Flow (g/s)	Change from CFD (%)	Cd (Exp)	Change from CFD (%)	Change from Text (%)	Re
100	1	22.306	36%	0.713	16%	13%	39,218
100	2	21.678	38%	0.709	16%	14%	38,113
100	3	22.052	37%	0.709	16%	14%	38,771
100	4	21.322	39%	0.695	18%	15%	37,486
100	5	21.445	38%	0.701	17%	14%	37,703
	Avg	21.761	38%	0.705	17%	14%	38,258
125	1	24.665	29%	0.683	19%	17%	43,364
125	2	24.710	29%	0.696	18%	15%	43,444
125	3	24.305	30%	0.685	19%	17%	42,732
125	4	24.990	28%	0.707	16%	14%	43,936
125	5	24.919	29%	0.702	17%	14%	43,812
	Avg	24.718	29%	0.694	18%	15%	43,458
150	1	27.362	22%	0.715	15%	13%	48,106
150	2	26.662	24%	0.703	17%	14%	46,875
150	3	26.280	25%	0.695	18%	15%	46,204
150	4	26.562	24%	0.703	17%	14%	46,699
150	5	26.416	24%	0.699	17%	15%	46,443
	Avg	26.656	24%	0.703	17%	14%	46,865
180	1	28.696	18%	0.697	18%	15%	50,452
180	2	28.629	18%	0.697	18%	15%	50,335
180	3	28.462	18%	0.693	18%	15%	50,039
180	4	28.913	17%	0.705	17%	14%	50,833
180	5	28.435	18%	0.694	18%	15%	49,992
180	6	28.663	18%	0.699	17%	15%	50,394
180	7	28.745	18%	0.701	17%	15%	50,538
	Avg	28.649	18%	0.698	17%	15%	50,369

Bibliography

1. Measurment of fluid flow by means of pressure differential devices inserted in circular cross-section conduits running full–Part 2: Orifice plates.

2. Fluent 6.3 User's Guide. Technical report, 2006.

3. Khaled Alhussan, Mohamad Assad, and Oleq Penazkov. Analysis of the actual thermodynamic cycle of the detonation engine. *Applied Thermal Engineering*, 107:339–344, 2016.

4. Vijay Anand, Andrew St. George, Robert Driscoll, and Ephraim Gutmark. Characterization of instabilities in a Rotating Detonation Combustor. *International Journal of Hydrogen Energy*, 40(46):16649–16659, 2015.

5. John D. Anderson. *Introduction to Flight*. McGraw-Hill Education, seventh edition, 2011.

6. Ionio Q. Andrus, Paul I. King, Marc D. Polanka, Air Force, Wright Patterson, Air Force, U S Air Force, Wright Patterson, and Air Force. Design of a Premixed Fuel Oxidizer System to Arrest Flashback in a Rotating Detonation Engine. *Journal of Propulsion and Power*, pages 1–11, 2017.

7. Theodore Bergman, Adrienne Lavine, Frank Incropera, and David DeWitt. *Fundamentals of Heat and Mass Transfer*. Wiley, seventh edition, 2011.

8. Xiaodong Chen, Dongjun Ma, Vigor Yang, and Stephane Popinet. High-Fidelity Simulations of Impinging Jet Atomization. *Atomization and Sprays*, 23(12):1079–1101, 2013.

9. Paul W. Cooper. *Explosives Engineering*. Wiley-VCH, New York, first edition, 1996.

10. Natalia Gimelshein, J Duncan, Taylor Lilly, Sergey Gimelshein, Aandrew Ketsdever, and Ingrid Wysong. Surface Roughness Effects in Low Reynolds Number Channel Flows (Preprint). Technical Report 0704, 2006.

11. Sanford Gordon and Bonnie McBride. CEARUN, 2012.

12. M. F. Heidmann. Propellant Vaporization as a Criterion for Rocket-Engine Design; Experiments Effect of Fuel Temperature on Liquid-Oxygen-Heptane Performance. Technical Report JULY, Langley Aeronautical Laboratory Library, Langley Field, 1957.

13. Dieter K Huzel and David H. Huang. *Modern Engineering for Design of Liquid-Propellant Rocket Engines.* American Institute of Aeronautics and Astronautics, Inc., Washington DC, 1992.

14. Carl P. Jones, Elizabeth H. Robertson, Mary B. Koelbl, and Chris Singer. Additive Manufacturing a Liquid Hydrogen Rocket Engine. Technical report, NASA Marshall Space Flight Center, Huntsvill, Al, 2012.

15. David M. Lane, David Scott, Mikki Hebl, Rudy Guerra, Dan Osherson, and Heidi Zimmer. *Introduction To Statistics.* Online edition, 2009.

16. Craig Nordeen, Douglas Schwer, Fredrick Schauer, John Hoke, Thomas Barber, and Baki Cetegen. Divergence and Mixing in a Rotating Detonation Engine. *51st AIAA Aerospace Sciences Meeting*, (January):1–14, 2013.

17. Kozo Osakada and Masanori Shiomi. Flexible Manufacturing of Metallic Products by Selective Laser Melting of Powder. *International Journal of Machine Tools and Manufacture*, 46(11 SPEC. ISS.):1188–1193, 2006.

18. Evan L. Pettus. Building a competitive edge with Additive Manufacturing. Technical report, Air War College, 2013.

19. Richard J. Priem and Marcus F. Heidman. Propellant Vaporization as a Design Criterion for Rocket-Engine Combustion Chambers. *NASA-TR R-67*, 1960.

20. Juan Rodriguez, Ivett Leyva, Jeffrey Graham, and Talley Douglas. Mixing Enhancement of Liquid Rocket Engine Injector Flow. Technical Report 0704, Air Force Research Laboratory, Edwards AFB, 2009.

21. Jason Shank. Development and Testing of a Rotating Detonation Engine Run on Hydrogen and Air. Master's thesis, 2012.

22. James A. Suchocki, Sheng-Tao John Yu, John L. Hoke, Andrew G. Naples, Frederick R. Schauer, and Rachel Russo. Rotating Detonation Engine Operation, 2012.

23. George P. Sutton and Oscar Biblarz. *Rocket Propulsion Elements*. John Wiley & Sons, Inc., Hoboken, eighth edition, 2010.

24. Christopher D. Tommila. Performance Losses in Additively Manufactured Low Thrust Nozzles. Master's thesis, Air Force Institute of Technology, 2017.

25. Vigor Yang, Mohammaed Habiballah, James Hulka, and Michael Popp. *Liquid Rocket Thrust Chambers: Aspects of Modeling, Analysis, and Design*. American Institute of Aeronautics and Astronautics, Inc., Reston, 2004.

REPORT DOCUMENTATION PAGE

Form Approved
OMB No. 0704–0188

1. REPORT DATE *(DD–MM–YYYY)*	2. REPORT TYPE	3. DATES COVERED *(From — To)*
22-03-2018	Master's Thesis	March 2017 - March 2018

4. TITLE AND SUBTITLE

ANALYSIS OF INJECTORS IN ROTATING DETONATION ENGINES

5a. CONTRACT NUMBER

5b. GRANT NUMBER

5c. PROGRAM ELEMENT NUMBER

6. AUTHOR(S)

Michael C. Waters

5d. PROJECT NUMBER

5e. TASK NUMBER

5f. WORK UNIT NUMBER

7. PERFORMING ORGANIZATION NAME(S) AND ADDRESS(ES)

Air Force Institute of Technology
Graduate School of Engineering and Management (AFIT/EN)
2950 Hobson Way
WPAFB OH 45433-7765

8. PERFORMING ORGANIZATION REPORT NUMBER

AFIT-ENY-MS-18-301

9. SPONSORING / MONITORING AGENCY NAME(S) AND ADDRESS(ES)

Department of Aeronautical Engineering
2950 Hobson Way
WPAFB OH 45433-7765
DSN 271-0690, COMM 937-255-3636
Email: michael.waters@afit.edu

10. SPONSOR/MONITOR'S ACRONYM(S)

11. SPONSOR/MONITOR'S REPORT NUMBER(S)

12. DISTRIBUTION / AVAILABILITY STATEMENT

DISTRIBUTION STATEMENT A:
APPROVED FOR PUBLIC RELEASE; DISTRIBUTION UNLIMITED.

13. SUPPLEMENTARY NOTES

14. ABSTRACT

This research represents an experimental and computational analysis of additively manufactured injectors for Rotating Detonation Engines (RDEs) for use in rocket propulsion. This research was based on the manufacture and testing of existing injector element designs using additive techniques. The designs were modeled from geometries gathered from Sutton and Biblarz *Elements of Rocket Propulsion* [23]. The goal of this research was to characterize the viscous losses of each design based on the discharge coefficient. The designs were computationally simulated to gain insight to the flow characteristics using multiple sets of conditions for surface roughness and inlet pressure. The results were then compared to experimental results of similar conditions. Each design was then tested using pressurized water as a simulated propellant. The results show the viscous losses to be highly dependent on design and the relative roughness of the surface. For designs with areas of high relative roughness and L/D such that flow interaction is facilitated the surface roughness was shown to effect the discharge coefficient.

15. SUBJECT TERMS

16. SECURITY CLASSIFICATION OF:

a. REPORT	b. ABSTRACT	c. THIS PAGE	17. LIMITATION OF ABSTRACT	18. NUMBER OF PAGES	19a. NAME OF RESPONSIBLE PERSON
U	U	U	U	133	Dr. Carl Hartsfield, AFIT/ENY

19a. NAME OF RESPONSIBLE PERSON
Dr. Carl Hartsfield, AFIT/ENY

19b. TELEPHONE NUMBER *(include area code)*
(937) 785-3636, ext 4667(carl.hartsfield@afit.edu)

Standard Form 298 (Rev. 8–98)
Prescribed by ANSI Std. Z39.18